ABSTRACT

THE COOPERATIVE EFFECTS OF CHANNEL LENGTH-BIAS, WIDTH ASYMMETRY, GRADIENT STEEPNESS, AND CONTACT-GUIDANCE ON FIBROBLASTS' DIRECTIONAL DECISION MAKING

by
Quang Long Pham

Cell migration in complex micro-environments, that are similar to tissue pores, is important for predicting locations of tissue nucleation and optimizing scaffold architectures. Firstly, how fibroblast cells – relevant to tissue engineering, affect each other's directional decisions when encountered with a bifurcation of different channel lengths was investigated. It was found that cell sequence and cell mitosis influence the directional choices that the cells made while chemotaxing. Specifically, the fibroblasts chose to alternate between two possible paths – one longer and the other shorter – at a bifurcation. This finding was counter-intuitive given that the shorter path had a steeper chemoattractant gradient, and would thus be expected to be the preferred path, according to classical chemotaxis theory. Hence, a multiscale image-based modeling was performed in order to explain this behavior. It showed that consumption of the chemotactic signals by the neighboring cells led to the sequence-dependent directional decisions. Furthermore, it was also found that cellular division led to daughter cells making *opposite* directional choices from each other; even it meant that one of the daughter cells had to move *against* the chemotactic gradient, and overcome oncoming traffic of other cells.

Secondly, a comparison of the effects of the various directional cues on the migration of individual fibroblast cells: including the chemoattractant concentration gradient, the channel width, and the contact-guidance was provided. Simple bifurcated mazes with two branches of different widths were created and fibroblasts were allowed to

travel across these geometries by introducing a gradient of PDGF-BB at the ‘exit’ of the device. By incorporating image-based modeling methodology into the experimental approach, an insight into (i) how individual cells make directional decisions in the presence of complex migration cues and (ii) how the cell-cell interaction influences it was provided. It was found that a larger width ratio between the two bifurcated branches outdoes a gradient difference in attracting the cells. Also, when cells encounter a symmetric bifurcation (i.e., no difference between the branch widths), the gradient is predominant in deciding which path the cell will take. Then, in a *symmetrical* gradient field (i.e., inside a bifurcation of similar branch widths, and in the absence of any leading cells), the contact guidance is important for guiding the cells in making directional choices. Finally, these directional cues were ranked according to the order from the most importance to the least: vast gradient difference between the two branches, channel width bias, mild gradient difference, and contact-guidance.

THE COOPERATIVE EFFECTS OF CHANNEL LENGTH-BIAS, WIDTH ASYMMETRY, GRADIENT STEEPNESS, AND CONTACT-GUIDANCE ON FIBROBLASTS' DIRECTIONAL DECISION MAKING

by
Quang Long Pham

A Dissertation
Submitted to the Faculty of
New Jersey Institute of Technology
in Partial Fulfillment of the Requirements for the Degree of
Doctor of Philosophy in Chemical Engineering

Otto H. York Department of
Chemical and Materials Engineering

December 2018

.

APPROVAL PAGE

THE COOPERATIVE EFFECTS OF CHANNEL LENGTH-BIAS, WIDTH ASYMMETRY, GRADIENT STEEPNESS, AND CONTACT-GUIDANCE ON FIBROBLASTS' DIRECTIONAL DECISION MAKING

Quang Long Pham

Dr. Roman S. Voronov, Dissertation Advisor — Date
Assistant Professor of Chemical Engineering, NJIT

Dr. Edward L. Dreyzin, Committee Member — Date
Distinguished Professor of Chemical Engineering, NJIT

Dr. Treena L. Arinzeh, Committee Member — Date
Professor of Biomedical Engineering, NJIT

Dr. Sagnik Basuray, Committee Member — Date
Assistant Professor of Chemical Engineering, NJIT

Dr. Murat Guvendiren, Committee Member — Date
Assistant Professor of Chemical Engineering, NJIT

BIOGRAPHICAL SKETCH

Author: Quang Long Pham

Degree: Doctor of Philosophy

Date: December 2018

Undergraduate and Graduate Education:

- Doctor of Philosophy in Chemical Engineering,
  New Jersey Institute of Technology, Newark, NJ, 2018

- Master of Science in Chemical Engineering,
  Yeungnam University, Gyeongsansi, Gyeongsangbuk-do, South Korea, 2011

- Bachelor of Engineering in Materials Technology,
  Ho Chi Minh City University of Technology, Ho Chi Minh City, Vietnam, 2008

Major: Chemical Engineering

Presentations and Publications:

Q. L. Pham, L. N. Rodrigues, V. D. Chandran, C. Bi, E. Stein, N. A. N. Tong, D. Chege, T. Dijamco, S. Basuray, R. S. Voronov. Cell Sequence and Mitosis Affect Fibroblast Directional Decision-Making during Chemotaxis in Tissue-Mimicking Microfluidic Mazes, Cell. Mol. Bioeng., accepted (2018)

Q. L. Pham, N. A. N. Tong, A. Mathew, R. S. Voronov. A Compact Low-Cost Low-Maintenance Open Architecture Mask Aligner for Fabrication of Multilayer Microfluidics Devices, Adv. Eng. Mat., accepted (2018)

Q. L. Pham, A. Mathew, P. Abatemarco, S. Lyer, R. S. Voronov. A Review On Commercial Low-Cost 3D Bioprinters, the Future of Inexpensive Tissue Fabrication, manuscript in preparation (2018)

T. A. Alam, Q. L. Pham, V. I. Sikavitsas, D. V. Papavassiliou, R. L. Shambaugh, R. S. Voronov. Image-Based Modeling: A Novel Tool For Realistic Simulations Of Artificial Bone Cultures, Technology, 4 (4) (2016)

Q. L. Pham, R. Voronov. Interplay Of Physical Constraints And Chemotaxis In Fibroblasts' Directional Decision, MAS17 Meeting of The American Physical Society, Nov 4-5, 2017, Newark, NJ, USA

Q. L. Pham, R. Voronov. Fibroblasts Affect Each Other's Directional Decision Making Process during Chemotaxis in Microfluidic Tissue Mimicking Mazes. 2017 AIChE Annual Meeting, Oct 29-Nov 3, 2017, Minneapolis, MN, USA

Q. L. Pham, R. Voronov. An All-in-One High Throughput Microfluidic Platform for Cell Culture and Migration. 2017 AIChE Annual Meeting, Oct 29-Nov 3, 2017, Minneapolis, MN, USA.

Q. L. Pham, R. Voronov. Tissue Patterning By Spatially Defined Addressable Microfluidic Delivery of Differentiated Growth Factors. 2017 AIChE Annual Meeting, Oct 29-Nov 3, 2017, Minneapolis, MN, USA

Q. L. Pham, R. Voronov. Fibroblast Chemotaxis in Microfluidic Maze. 43rd Annual NEBEC, Mar 31st -April 2nd, 2017, NJIT, Newark, NJ, USA

Q. L. Pham, R. Voronov. Chemotaxis-Based Mesenchymal Stem Cell Migration in 2D Microfluidic Maze. 2016 AIChE Annual Meeting, November 13-18, 2016, San Francisco, USA

Dành tặng cho bố mẹ, ông nội, Mai, và toàn thể gia đình thân yêu

To my parents, grandfather, little sister Mai, and my beloved family

ACKNOWLEDGMENT

I would like to express my deep gratitude to my advisor, Prof. Roman S. Voronov, for his mentorship and instructions. His continuous guidance and motivation are the key factors that help me to move my research forward. He also supported me to pursue my future career and help me to make it happen.

I also want to thank Prof. Sagnik Basuray for his advice and suggestions regarding experiment, writing papers, and journal submission; and the encouragement of pursuing my future career.

I also want to thank Prof. Edward L. Dreizin for his comments on my manuscript, which greatly help me to improve my dissertation.

I also want to thank Prof. Treena L. Arinzeh and Prof. Murat Guvendiren for the suggestions to improve my dissertation.

I would like to acknowledge all committee members for their support on the completion of my dissertation.

I am also thankful for the financial support from the Department of Chemical Engineering, the Gustavus and Louise Pfeiffer Foundation, and the NSF-Icorps.

I am grateful for Prof. Robert Barat for his generous offer of his lab space and the permission to use his instruments, which are greatly helpful for many of my lab projects.

My thanks to Anh, Femi, Lydia, Akshay, David, Vishnu, Timothy, Migla, Vatsal, Austin, Paul, John and Brandon. You guys are great lab mates. Your helps with the experiment and the computation are highly appreciated.

Lastly, I want to sincerely thank my family for their unconditional love!

TABLE OF CONTENTS

TABLE OF CONTENTS
(Continued)

TABLE OF CONTENTS
(Continued)

TABLE OF CONTENTS
(Continued)

TABLE OF CONTENTS
(Continued)

Chapter **Page**

LIST OF TABLES

LIST OF FIGURES

Figure **Page**

(Continued)

Figure **Page**

LIST OF FIGURES
(Continued)

Figure **Page**

LIST OF FIGURES
(Continued)

Figure **Page**

LIST OF FIGURES
(Continued)

Figure **Page**

LIST OF FIGURES
(Continued)

Figure **Page**

LIST OF FIGURES
(Continued)

Figure **Page**

LIST OF FIGURES
(Continued)

Figure **Page**

CHAPTER 1

INTRODUCTION

The shortage in transplantable organs is one of the major concerns of the healthcare industry. According to U.S. Department of Health & Human Services, nearly 114,926 people in the U.S need a lifesaving organ transplant, and only 11,491 transplants are performed so far in 2018. In early 1990s Langer and Vacanci introduced Tissue Engineering (TE) (1) to address this issue through the synthesis of viable tissues for artificial organ development. Tissue Engineering integrates principles and methods of bioengineering, material science, and life sciences to understand structural, functional, and mechanical properties of normal or degenerated tissues and develop biological substitutes to restore or reconstruct damaged tissues or even entire organs. With its limitless supplies, TE emerges to be prospective alternatives to classical reconstructive surgical therapies, which largely rely on organ donations. (1, 2) Thus, successful bio-manufacturing of tissues and organs is central to satisfying the ever-growing demand for transplants.

As TE relies extensively on three-dimensional (3D) scaffolds in order to generate appropriate microenvironment for the cellular ingrowth and extracellular matrix (ECM) production (3), the scaffolds are required to be meticulously designed to accurately deliver and monitor cellular activities. There is a plethora of scaffold fabrication techniques such as phase separation, particulate-leaching, textile, electrospinning, nano-fibrous, self-assembly, and supercritical fluid-assisted; however, these techniques fail to provide precise control of the 3D pore architecture of the scaffolds but instead, forming random and ill-controlled structures. (4) Computer-assisted design and manufacture

(CAD/CAM) manifests itself as an ideal technique to tackle this problem. This method can generate well-defined structures at high resolution while allowing rapid prototyping of desire scaffold with controlled architecture. As a result, the arena of 3D printing for TE has rapidly expanded over the last decade. (5) Even though scaffolds can be fabricated with high fidelity and physically similar to a decellularized tissue structure using 3D printing, the engineered tissue still fails due to the poor control of cell behavior inside the tissue pores. During *in vitro* culture, cells can either be seeded on top of the scaffold and passively infiltrate it or be stimulated with external force (i.e., centrifuge, shear stress, etc.) to accelerate the infiltration (6); or they can be positioned to a specific location inside the scaffold using bioprinting technology (7); however, as being said, subsequent monitoring and controlling of cellular behavior – such as migration inside the tissue pore – are missing in all of previous studies, especially at single cell level, which poses an immense challenge in current TE technologies.

1.1 Chemotaxis of Fibroblast Cells is Important to Tissue Engineering

Chemotaxis – the directional migration of cells in response to a gradient of chemotactic cue – is crucial for tissue formation since tissue growth only nucleate at the locations where the cells are. Even though there has been a significant number of studies covering a wide range of cells and chemo-attractants, most of the *in vitro* methods fails to provide an indispensable dynamic feature of cell chemotaxis (i.e., molecule transport, cell speed and directionality, etc.) within a complex tissue-like structure. This gap in the knowledge apparently restricts the design and optimization of engineered tissues. Therefore, it is imperative to have a comprehensive model that can help fill in the missing piece.

Fibroblast is an important cell type for wound healing *in vivo*. The cell contributes to the tissue formation by secreting different growth factors and cytokines, synthesizing,

depositing, and remodeling of extracellular matrix materials such as collagen I-VI and XVIII, glycoproteins, and proteoglycans, glycosaminoglycans (GAGs), and hyaluronic acid (HA).(8-10) Therefore, fibroblasts are important for tissue engineering. For example, they act as a key player in tissue vascularization by providing 3D support the organization and migration of endothelial cells, the blood vessel builder, as well as secreting angiogenesis factors.(11) Moreover, fibroblasts have been found to influence and modulate neighboring cells.(12) Thus, the successful engineered tissue growth is directly related to the fibroblast activity.

The directed movement of fibroblasts in the tissue is guided by a number of growth factors such as platelet-derived growth factors (PDGFs), transforming growth factors, epidermal growth factors, and fibroblast growth factors.(9, 13) PDGFs are those being released at the wound site by platelets and inflammatory cells and have been found to have both chemotactic and mitogenic effects on fibroblasts.(14) *In vitro* studies highlight the use of PDGF, especially the –BB isomer, as the chemoattractant for fibroblast.(15-21) The cells sense PDGF-BB gradient *via* the receptor-mediated mechanism. When being exposed to an asymmetric concentration field of chemoattractant, fibroblasts tend to polarize themselves along the field, as evidenced by the elongated morphology, the formation of actin protrusion, and the asymmetric distribution of the PDGF receptors (PDGF-R) on the cell membrane. The mechanism of the gradient sensing has been well studied. (19)When PDGF-Rs, receptor tyrosine kinases, are bound by PDGF ligands, both receptors and ligands are internalized to the endosome. This in turn activates the phosphoinositide-3 kinase (PI-3K) signaling pathway that induces the cell motility. PI-3Ks are accumulated internally and the distribution of accumulation inside the cell is fundamental receptor-mediated signal

transduction and spatial gradient sensing in fibroblast. Haugh et al. demonstrated that fibroblasts only exhibited significant response to a range of chemoattractant concentration (~ 0.1 – 2 nM PDGF-BB or 2.5-50 ng/ml) and steep gradient (>10% difference between front and back of the moving cells).(21). Even though it is useful to understand single/isolated cell biology, how the chemotaxis of single fibroblasts in concert with others in tissue-like environment (i.e. scaffold pores) still remains understudied. In essence, the presence of neighboring cells, which can consume chemoattractant molecules *via* endocytosis, can change the gradient sensed by the migrating cells, thereby creating a much more complicated scenario. This posed a challenge to current single/isolated cell models, which need to be improved to account for the presence of the cell-cell interaction.

Directional decision is one of the important properties of cell migration because understanding the directional decision of the moving cells – i.e., what decisions they make and what cause that decision makings – can help to control the cell migration, especially in confined environments. There have been a number of studies investigating the directional decision of cells in different confined microchannels of various styles (i.e., mazes, bifurcation, straight channels, etc.) using microfluidic devices (**Table 1.1**). The directional decision of cells has been found to be dependent on the channel width, which are directly related to gradient steepness; contact-guidance; and cell division. Yet, the cooperated effects contributed by these factors have not been elucidated and comparison between them has been largely ignored. In addition, these migration models treat the migrating cells as individual with little attention to the cell-cell interaction, which has been known to be critical, especially when cells usually migrate in groups. Moreover,

these studies mostly focus on cancer and immune cells while fibroblasts, which have more implications to the tissue engineering, has not been widely studied.

Table 1.1 Summary of Previous Findings on Directional Decision Making of Various Types of Single Cells

Cell Type	Migration Platform	Directional Cue	Decision Influence	References
Epithelial cancer cells	Complex maze	Epidermal growth factor (EGF)	Self-generated gradient	Scherber et al.(22)
Neutrophil	Simple maze	formyl-methionyl-leucyl-phenylalaine (fMLP)	Steeper chemoattractant gradient	Ambravaneswaran et al.(23)
Neutrophil	Biased bifurcation	Hydraulic resistance + fMLP	Lower hydraulic resistance	Prentice-Mott et al.(24)
Breast cancer cells	Biased bifurcation	Directional and dimensional constraints	Path size constraint and path orientation; Cytoskeletal drugs	Mak et al.(25)
Breast cancer cells	Biased bifurcation	Physical cues + contact guidance	Amount of wall contact and path size constraint;	Paul et al.(26)
Human prostate cancer	Tapered straight channels	EGF + mechanical constraint	Path size constraint	Rao et al.(27)

Furthermore, the division of the mother cells leads to two daughter cells moving in distintive direction on planar surface. (28-30) However, there have not been any studies demonstrating the directional decision of daughters in a confined environment. Whether or not these characteristics can be changed under the influence of gradient, physical confinement, and the surface where the cells contact has not been elucidated as well.

1.2 Microfluidic-Assisted Technology: Useful Tool for Study Single Cell Migration

One difficulty with controlling cells is the understanding of cell behavior, i.e. cell migration, in tissue pores at single cell level. This, in essence, is directly related to the successful vascularization, extracellular matrix production, and tissue ingrowth inside the scaffold. There are a number of cell migration assays available (**Figure 1.1**). For example, the trans-well membrane assay (or Boyden chamber) is a chamber consisting of two compartments (one on top of the other) separated by a microporous membrane.(31)

Cells are placed on the top compartment while chemoattractant-rich media is added into the bottom compartment. The cells move towards the chemoattractant following a concentration gradient established inside the membrane. Migration index is quantitatively determined by the number of cells successfully migrating to the bottom chamber. Even though the Boyden chamber assay is simple and popularly used,(32, 33) it lacks a capacity to observe the cell migration process, and thus many important migratory parameters (i.e., cell speed, directionality) are neglected using this method. The scratch assay (also known as wound-healing assay) allows the observation of the cell dynamic during the migration (34); however, the assay is invasive as it causes damage to the cells during scratching. It also falls short of describing the chemotaxis phenomenon, which is critical to guiding cell migration directionally. The gel-based chemotaxis assay,(18) on the other hand, can enable both visualization of the cell movement and the introduction of chemoattractant gradient; however, the established gradient is not well-described by this method, especially near the single cell locality. Thus, the method is only suitable for a population-average analysis, while lacks the capability of studying individual cells. Phagokinetic assay has been developed to provide the tracking of individual cells by using coverslip coated with gold particles.(28) When cells move, they uptake the particles and leave behind particle-free tracks that can be visualized using microscope. The strength of this method is its simplicity and ability to visualize individual cells' moving path. However, there comes the downsides for this method. For example, it is only available to very low cell density due to the fact that collision of two cells may lead to the mistaken reading of the result. It is also limited to cell migration on a flat substrate without confinements, which is closer to the tissue pore structure.

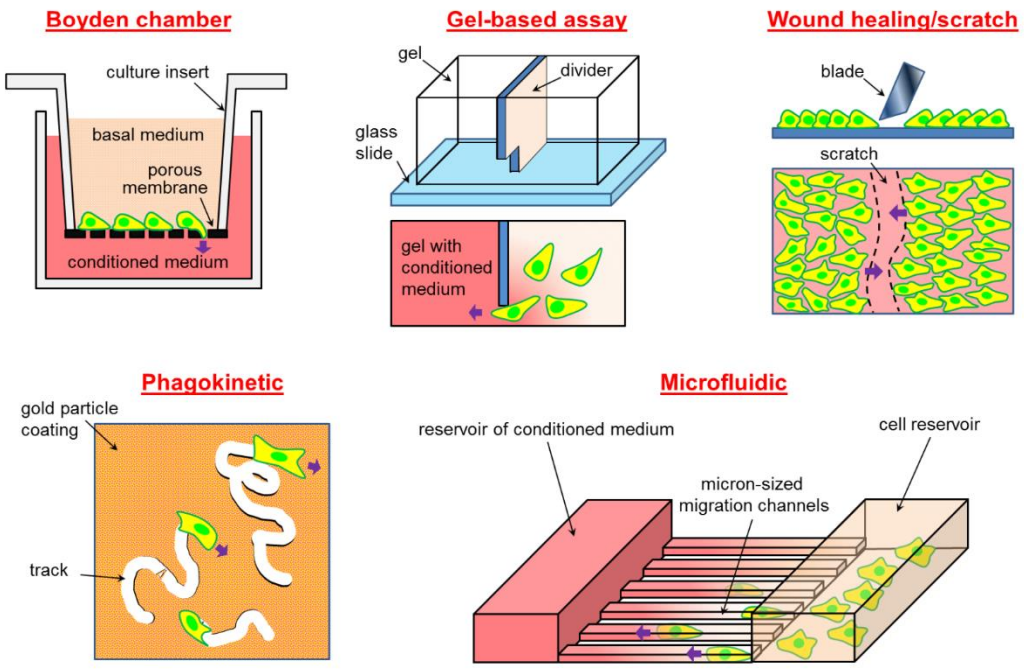

Figure 1.1 Assays commonly used in cell migration studied. Purple arrows indicate the direction of migration.

Microfluidic technologies, which involve the use of miniaturized device, can overcome the drawbacks encountered with classical assays by providing specified structure, which can be more representative to the tissue scaffold architecture; can establish well-defined gradient; and can facilitate the study of individual cell chemotaxis.(35) Furthermore, the technology allows the controlling and maneuvering of fluidic substances at high resolution, thus allow one to control the cell behavior at high fidelity. Microfluidic-assisted chemotaxis assays that have been developed include a flow-based and a flow-free system. In the former type, the flow is driven by programmable pumping (i.e., pneumatic, peristatic, syringe-based, etc.) to carry the cells, chemoattractant to a microchip platform. The flow-free system creating gradient using two reservoirs of different chemoattractant concentrations, namely, source and sink. In theory, the flow-based system allows a better dynamic control of gradient compared to the flow-free. However, the flow-based requires complicated setup and expose cells to

shear stress, while the gradient can be easily disturbed by convection of the flow. The flow-free, even though lack the capability of creating a dynamic gradient, can still be used in chemotaxis study owing to its simplicity and the minimization of the flow effects on the cells.

1.3 Image-Based Modeling: Realistic Simulations for Tissue Engineering

Successful production of artificial tissues depends on the ability to control the tissue growth in a spatiotemporal manner, which is in turn subject to the understanding of the interplay between the scaffold architecture, culture conditions, and cell biology within the construct. Recent developments in computer modeling and biomedical imaging have significantly contributed to the advancement of scaffold design and optimization, which is otherwise too complicated to do in a rational manner.(36) Traditional computer-assisted tissue engineering was done using virtual scaffold drawings, with little-to-no cross validation with experiment.(37-42) Thus, such studies were unable to provide a precise "picture" of the tissue growth inside the scaffold. On the other hand, image-based modeling, which combines images collected experimentally with computation, can simulate the exact microenvironment within the scaffold, accounting for both transport phenomena physics and cell biology.(43) However, one challenge with image-based simulation is the lack of real-time experimental data of cell migration within scaffolds. For example, images acquired from μCT scanning provide only a single time point snapshot, because the sample is sacrificed during the imaging process. This leads to a lack in experimental data for development and cross validation of the models. Therefore, in order to provide experimental data for the image-based simulations, automatic image acquisition systems based on a fully automated microscope coupled to microfluidic platforms were developed.

1.4 Objectives

1.4.1 Investigate the Influence of Cell-Cell Interaction and Cell Division on the Directional Decision of Fibroblast

As reviewed earlier, current models have understudied on how individual fibroblasts affect each other's decision making and whether or not this is influenced by the cell division. Therefore, my aim is to elucidate this unknown picture.

1.4.2 Investigate the Cooperated Effects of Various Directional Cues on the Decision Making of Fibroblasts

The directional decision of cells has been found to be dependent on the channel width, gradient steepness, contact-guidance, and cell division. However, the relative importance of the different directional cues on the cell migration is understudied. Therefore, I aim to investigate the cooperated effects of the above-mentioned directional cues on the cell chemotaxis as well as unravelling the relative importance between them.

1.5 Dissertation Outline

In Chapter 2, I aim to explore the mechanisms by which single fibroblasts affect each other's directional decisions, while chemotaxing in microscopic tissue pores (representative of scaffold microporous structure). Two types of social interactions on fibroblast platelet-derived growth factor-BB (PDGF-BB)-induced migration in microfluidic mazes was evaluated: cell sequence and mitosis.

From the experimental results, I found that cells tend to alternate at the bifurcation of long and short paths instead of following each other in the short path to ascend a steeper gradient. This is likely due to the consumption of PDGF-BB by the *leading* cells, which modifies the gradient experienced by the *following* cells. To validate that hypothesis, I have used image-based simulation of the dynamics of the PDGF-BB

gradient in the maze in the presence of the moving cells that consume the chemical. By segmenting the cells from the phase-contrast images and applying transport parameters into the model, the gradient with respect to each moving cell could be generated. The simulation results suggested that the cell consumption of the chemoattractant contributed to the alternating feature of the cell sequence.

In Chapter 3, the cooperated effects of the channel size, the gradient steepness, and the contact-guidance on the decision making of fibroblasts were evaluated and compared. We use a migration model which consists of bifurcated maze channels of varying widths. By inducing the migration with PDGF-BB, migrating fibroblasts are exposed to various external cues including chemoattractant gradient, channel width bias, and the contact surface. The gradient dynamic inside the mazes induced by the cell-cell interaction is calculated using the image-based simulation method mentinoed earlier. We found that larger channel size bias between the two bifurcated channels outdoes a gradient difference in attracting the cells. When cells encounter a bifurcation of no difference in the branch size, the gradient is predominant in deciding which path the cell will take. The cells were found to be guided by the way they contact the wall of the feeder channels. Finally, these directional cues were compared and ranked according to their strength in attracting the cell migration.

CHAPTER 2

CELL SEQUENCE AND MITOSIS AFFECT FIBROBLAST DIRECTIONAL DECISION-MAKING DURING CHEMOTAXIS IN MICROFLUIDIC MAZES

2.1 Abstract

Directed fibroblast migration is central to highly proliferative processes in regenerative medicine and developmental biology, such as wound healing and embryogenesis. However, the mechanisms by which single fibroblasts affect each other's directional decisions, while chemotaxing in microscopic tissue pores, are not well understood. Therefore, we explored the effects of two types of relevant social interactions on fibroblast platelet-derived growth factor-BB (PDGF-BB)-induced migration in microfluidic mazes: cell sequence and mitosis. Surprisingly, it was found that in both cases, the cells display behavior that is contradictory to the global chemoattractant gradient pre-established in the maze. In case of the sequence, the cells do not like to take the same path through the maze as their predecessor, when faced with a bifurcation. To the contrary, they tend to alternate - if a leading cell takes the shorter (steeper gradient) path, the cell following it chooses the longer (weaker gradient) path, and *vice versa*. Additionally, we found that when a mother cell divides, its two daughters go in opposite directions (even if it means migrating against the chemoattractant gradient and overcoming on-going cell traffic). Thus, it is apparent that fibroblasts modify each other's directional decisions in a manner that is counter-intuitive to what is expected from classical chemotaxis theory. Consequently, accounting for these effects could lead to a better understanding of tissue generation *in vivo*, and result in more advanced engineered tissue products *in vitro*.

2.2 Introduction

Directional decision-making during cell migration is important for regenerative medicine (e.g., tissue engineering, wound healing)(8) and developmental biology(13, 44) since tissue development depends on how the cells distribute themselves within the complex pores of the extra-cellular matrix (ECM).(44-46) However, current single cell studies are not representative of the scenarios in which multiple cells enter the pores simultaneously and influence each other's decisions. At the same time, "collective" migration investigations mainly focus on cells that form stable adhesions between each other during movement (e.g., epithelial cells).(47-49) Yet, fibroblasts, which are more relevant to synthesizing collagen and ECM, tend to migrate as individual cells when squeezing through the microscopic tissue pores.(50) Previous studies on how social interactions influence fibroblasts' migration behaviors mainly focused on random migration, while we could not find published examples of such influences on chemotaxis.(28, 30, 51-55) As a result, the processes by which single fibroblasts affect each other's directional decision-making while chemotaxing in tissues are not well understood. Given the lack of knowledge, this manuscript set out to investigate two unexplored aspects of fibroblast migration that are particularly relevant to proliferative environments commonly encountered in regenerative medicine: effects of cell sequence and mitosis on chemotaxis in tissue-sized pores.

In case of the former, we hypothesized that the order in which the cells enter the pores will affect their directional choices at bifurcations. Fibroblast migration in tissue is primarily regulated *via* attraction to chemical substances originating from the hematopoietic and blood system, or from products of the ECM. However, other cell types have been known to self-generate/modify existing chemical gradients when

confined in microscopic spaces.(22, 56) Moreover, fibroblasts are known to deposit integrin-containing “migration tracks” that affect the motility of their neighbors.(28, 57) Therefore, it is logical to conclude that the localized fibroblast sequence effects will compete with the global chemotactic gradient in the microscopic pores.

Secondly, since tissue generation is a highly proliferative process, we aimed to explore the effects that cell division has on the fibroblast decision-making during chemotactic migration. Mitosis has been found to affect migration in both fibroblasts(28, 52) and other cell types.(25, 58, 59) However, these experiments were conducted in the absence of a chemotactic gradient and/or micro-confinement, which is more representative of geometric features of tissue microenvironments.(60) Therefore, we wanted to see whether the cell division effects on fibroblast hold true under chemotaxis and in the spatial confinement.

To that end, we chose the most appropriate migration platform from currently available sources(22-27) – a microfluidic maze, which contains confinement features that offer multiple directional choices.(22, 23) Specifically, the maze consists of a long path, a short path, and dead ends. In order to emulate chemotaxis in tissue and induce the fibroblast migration across the maze, we selected platelet derived growth factor – BB (PDGF-BB), a fibroblasts “mitoattractant” (i.e., a chemoattractant(18, 61, 62) and a mitogen(14, 15, 63) at the same time).

To our surprise, we found that in both, the cell sequence and the mitosis cases, the cell-cell interactions cause the fibroblasts to display behavior that is contradictory to what would be classically expected from the chemoattractant gradient established in the maze. Namely, we found that the fibroblasts path choices alternate depending on each predecessor’s decision, and that cell division occurring during the chemotaxis yields

daughter cells with directional bias distinctive from that of their siblings. Therefore, the presented results carry practical implications for both engineered tissue design, and for understanding the fibroblast biology in their native micro-constricted environments.

2.3. Materials and Methods

2.3.1 Materials

Polydimethylsiloxane (PDMS) Sylgard 184 was purchased from Dow Corning (Midland, MI). Negative photoresist SU-8 was purchased from Microchem (Newton, MA). Bovine collagen Type I 3mg ml^{-1} solution (PureCol) was purchased from Advanced Biomatrix (San Diego, CA). Recombinant rat platelet-derived growth factor-BB (PDGF-BB) was purchased from R&D Systems (Minneapolis, MN). Culture media was prepared from Minimum Essential Medium (MEM) (Sigma, MO) supplemented with 10% (v/v) fetal bovine serum (FBS) (VWR, Radnor, PA), and 1% (v/v) penicillin-streptomycin (10,000 U mL^{-1}) (Thermofisher, Waltham, MA). Basal media was composed of MEM supplemented with 1% (v/v) penicillin-streptomycin. For incubation in 5% CO2 atmosphere, media was buffered by 26 mM sodium bicarbonate (Sigma, MO). CO2-independent media buffered by 20 mM HEPES (Sigma, MO) was used for the microscope stage-top experiment.

2.3.2 Device Description

The microfluidic platform used in this work consists of micron-sized mazes (adapted from a cancer migration study by Scherber et al.).(22) The maze is a network of bifurcations consisting of two through paths, one short (1,300 µm) and one long (1,700 µm), and several dead ends. Its channels were chosen to have a rectangular profile 24 µm wide by 17 µm high (see **Figure 2.1**A & D), in order to limit the number of cells entering the maze to 1-3 at a time. Each maze had a single entrance and exit, shown at

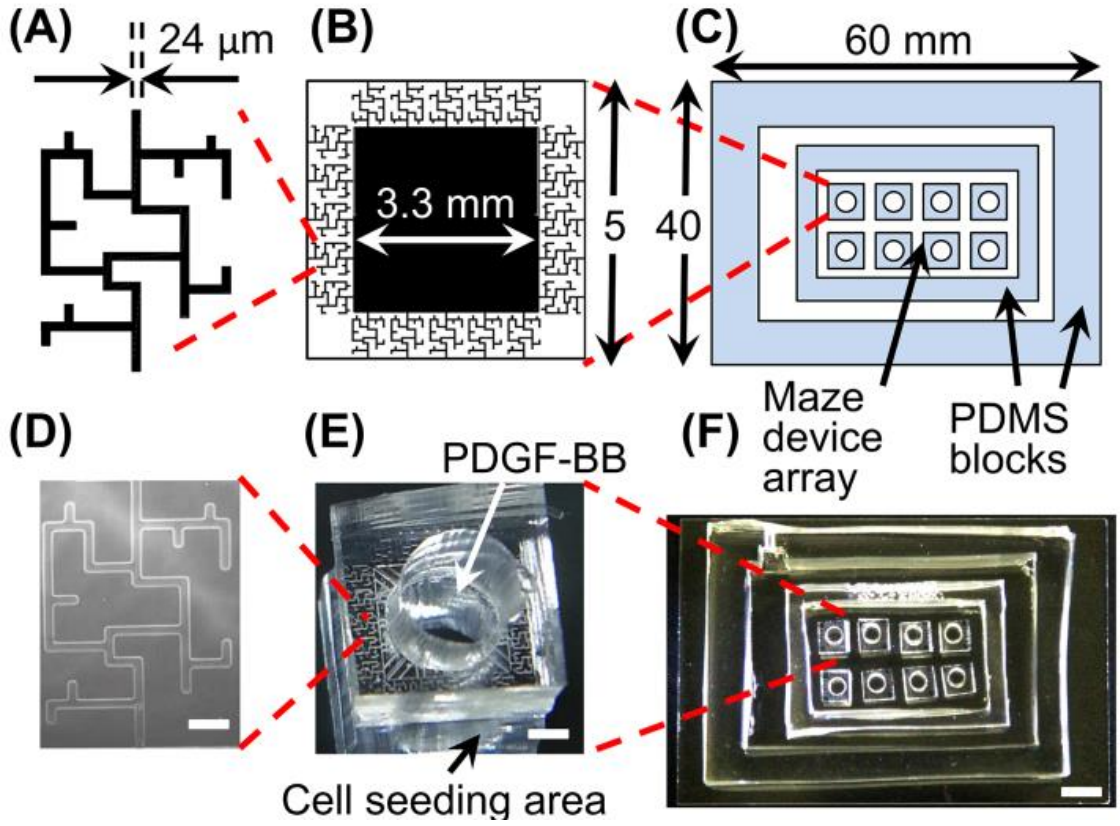

Figure 2.1 (A, B, C) Schematics showing dimensions of a single maze, a single microfluidic device, and an array of the devices inside of a stage-top custom incubation chamber, respectively. (D) Phase contrast microscopy image of a single maze network. Scale bar is 100 µm. (E) Photograph of a single microfluidic device, consisting of 20 maze networks that share a central chemoattractant reservoir. A circular 3 mm diameter hole was punched in the center of each device in order to deposit the PDGF-BB into the reservoir. Cells were seeded outside of the devices. Scale bar is 1 mm. (F) An array of microfluidic devices placed inside a stage-top custom incubation chamber, consisting of two PDMS blocks bonded to the top of a glass slide. Scale bar is 5 mm.

the bottom and top of those figures, respectively. Twenty mazes of identical design were replicated per a single microfluidics device (see **Figure 2.1**B & E). The device connected a large cell seeding area, with zero initial concentration of the chemoattractant, to a central reservoir of chemoattractant-rich media, *via* the mazes. In this manner, a stable chemoattractant gradient was established between the cell compartment and the central reservoir, in order to prescribe direction to the cell migration. Finally, multiple identical devices were placed inside of a PDMS enclosure for high-throughput experimentation (see **Figure 2.1**C & F). The enclosure also isolated the whole setup from the external environment, in order to prevent contamination.

2.3.3 Custom Incubation Chamber for Culturing on the Microscope Stage

PDMS with a base-to-crosslinking agent ratio of 10:1 was poured into two 100 mm petri dishes to different thicknesses: 8 mm and 10 mm. After heating at 65 °C overnight, the resulting solid PDMS blocks were removed from the petri dishes and cut in rectangular shapes: one smaller and one larger. A 2-mm hole was punched on one side of the larger block for mounting a temperature sensor. The two blocks were then treated with air plasma using a plasma cleaner (PDC-001, Harrick Plasma, Ithaca, NY), and bonded on to a pre-cleaned 50x75x1 mm glass slide (Ted Pella, Redding, CA), one inside the other (see **Figure 2.1**C & F). The larger and thicker block served as the periphery of the incubation chamber, while the smaller block formed an enclosure for the microfluidic devices array, in order to prevent contamination from the temperature sensor opening. Phosphate buffer saline (PBS) was added to the space between the two PDMS blocks in order to humidify the incubation chamber.

2.3.4 Device Fabrication

The mold for the device was fabricated using SU-8. First, the microscale pattern was sketched using AutoCAD (Autodesk, Mill Valey, CA) and printed at 16,525 dpi on a transparency (Fineline Imaging, Colorado Springs, CO) to generate a high-resolution photomask. SU-8 was spin coated, exposed to UV light, and developed on a 4-in silicon wafer (University Wafer, Boston, MA) following the manufacturer‘s protocol to generate 17-μm high microfluidic channels. Microfluidic devices were fabricated using a single-layer soft lithography method. Typically, PDMS with a base-to-agent ratio of 10:1 was poured over the photo-patterned mold, degassed, and cured at 65 °C overnight. The cast PDMS was carefully peeled off from the master, and a 3-mm biopsy punch was used to create a central hole in each device for PDGF-BB delivery to the chemoattractant reservoir. Individual devices were cut using a thin razor blade, rinsed with 70% isopropyl alcohol and left dried in an oven. Then 6 to 8 devices were treated with air plasma for 30 s at medium radio-frequency power, before they were bonded inside of the culture chamber. The assembly was then heated to 65 °C on a hot plate for 5 min to improve the bonding.

2.3.5 Surface Treatment

Right after bonding, the device was placed under a 200-mTorr vacuum for 2 min to remove air inside the micro channels. Immediately after being released from vacuum, about 150 μg ml^{-1} collagen type I solution was added to completely coat the micro channels and the cell seeding area. The coated device was then sterilized by UV light inside a biohood for 1 hour, and washed several times with PBS before use.

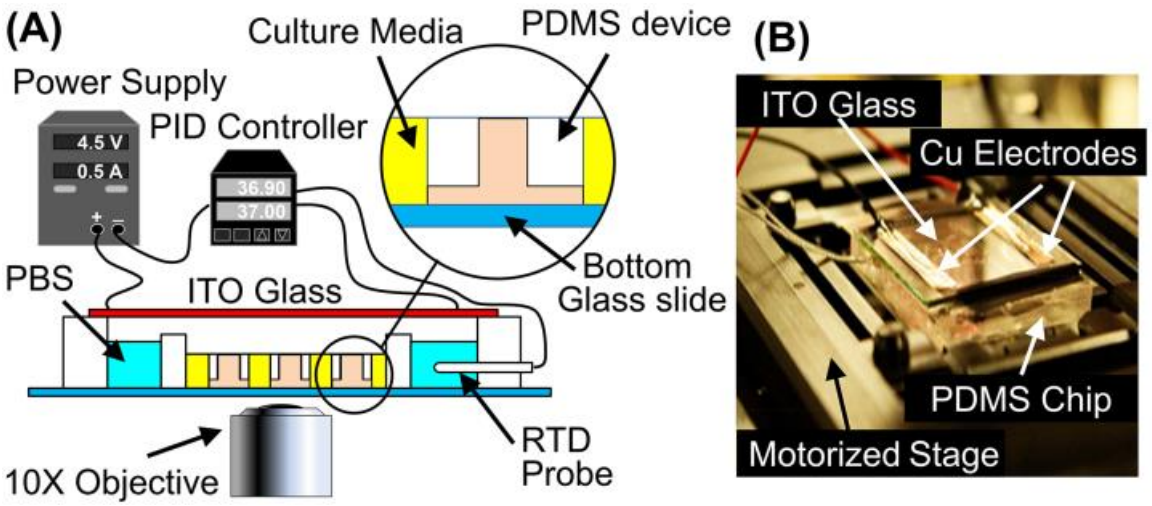

Figure 2.2 (A) Experiment setup schematic, showing the custom incubation chamber used for culturing on the automated microscope's stage. The setup consisted of a benchtop variable power supply, which provided a current of 0.5 A to an ITO glass that was placed on top of the PDMS chamber. Heat generated by the glass warmed up the media inside of the chamber. Temperature was measured using an RTD sensor coupled to a PID controller, which modulated the power supply in order to maintain a constant temperature of 37 °C. (B) Photograph of the incubation chamber in operation. Electric current was fed to the resistive layer of the ITO glass through a pair of copper electrodes. This led to heat generation underneath of the PDMS chamber. The incubation chamber was placed on top of a XY motorized stage, controlled by the computer, for imaging.

2.3.6 Cell Preparation

Mouse embryo NIH/3T3 (ATCC® CRL-1658TM) fibroblasts were purchased from ATCC (Manassas, VA). Prior to being transferred to the microfluidic device for the migration experiments, the cells were incubated in the culture media inside of T75 flasks. The flasks were kept at 37 °C and in a humidified atmosphere of 5% CO_2 in air. The culture media was changed every two days to ensure normal cell growth. Prior to the migration experiments, the cells were trypsinized from the T75 flasks and loaded into the chip, with a seeding density of about 50,000 cells cm^{-2}. The chip was incubated at 37 °C under 5% CO_2 for 6 h to allow cell attachment. Then the cells were cultured in serum-starved media (MEM supplemented with 1% penicillin-streptomycin) for 6 hours.

2.3.7. Cell Migration Experiments and Image Acquisition

At the start of the experiment, cell culture media in the chip was replaced with CO_2-independent basal media buffered by HEPES. 20 µL of basal media supplemented with 25-50 ng mL^{-1} PDGF-BB was then added into the central reservoir of each device. The concentration of PDGF-BB at the exit was chosen to be higher than that typically used to induce migration and mitosis,(14) keeping in mind that it would be lower at the maze's entrance. The experimental setup used a custom incubation system, which is illustrated in **Figure 2.2**. A resistance temperature detector (RTD) sensor (Auberin, Alpharetta, GA) was mounted to the mounting hole on the larger PDMS block. The chip was covered by a 15Ω cm^{-2} Indium Tin Oxide (ITO)-coated glass slide (Adafruit, NY) and mounted on a motorized microscope stage (Ludl Electronic, Hawthorne, NY). Electrodes on the ITO glass slide were connected to a bench top power supply (MPJA, FL) to supply a heating power of 1.5 W. The RTD sensor was connected to a PID controller (Auberin, Alpharetta, GA) which helped to maintain a constant temperature of 37 ± 0.2 °C. Time-lapse phase-contrast imaging of the fibroblast migration was performed using a fully automated Olympus IX83 microscope fitted with a 10X phase-contrast objective (Olympus, Japan), a CMOS camera (Orca Flash 4.0 V2, Hamamatsu, Japan), and an autofocus module (ZDC, Olympus, Japan). Time-lapse images were automatically captured at 5-15 min intervals for duration of 20 hours. For each device at each time step, 36 tile images were acquired at different locations, stitched, and stabilized using an in-house Matlab® 2016b code (The MathWorks, Inc., Natick, MA). The cells were labeled manually.

2.3.8 Data Analysis

Migratory cells were tracked using the Manual Tracking plug-in for ImageJ software (National Institutes of Health).(64) The directional decision chosen by each individual cell at the long-short bifurcation was determined *via* manual observation. Quantitative data of cell sequence was generated using an in-house Matlab® 2016b code (The MathWorks, Inc., Natick, MA). Cells that underwent division were not included in the sequential cell migration statistics. Instead, the directional decisions of the mitotic cells were counted separately. Significance level was determined by the nonparametric binomial test. Statistical significance was set as $p < 0.05$.

2.3.9 Global PDGF-BB Gradient Simulation within a Maze without Cells

The PDGF-BB concentration gradient formed between the two ends of the maze was simulated numerically using COMSOL 5.3a Multiphysics (COMSOL, Burlington, MA). Specifically, steady state two dimensional transport of diluted species was modelled inside of 24-μm wide by 17-μm high channels, resembling the real maze geometry (see **Figure 2.3**). The chemoattractant reservoir and the cell seeding area were treated as infinite sources and sinks, respectively. Constant concentration boundary conditions, corresponding to the experiment, were set to $C_{P,exit}$ = 50 ng mL^{-1} PDGF-BB at the source (i.e., maze exit), and to zero at the sink (i.e., maze entrance). A diffusion coefficient of $D_{P,maze}$ = 1 x 10^{-10} m^2/s was used to represent the PDGF-BB (MW = 25 kDa) in an aqueous solution.(65) Chemoattractant gradient values at every point in the maze were calculated from the vector magnitude of two components, x-axis (horizontal) and y-axis (vertical), both of which increased towards the higher concentration of PDGF-BB (see **Figure 2.3**C). The presence of the cells in the maze was not taken into account by the calculation.

2.4 Results

To better understand how single fibroblasts affect each other's directional decision-making under chemotaxis in microscopic tissue pores, we studied their motility in spatially confined maze channels. The mazes contained two possible through paths and multiple dead-ends. The cells entered the mazes through a common path, and would eventually reach a bifurcation where they had a choice of either a shorter through path (see **Figure 2.3**A), or one that was approximately 1.3 times longer (see **Figure 2.3**B). Eventually, they exited the maze through another common path (assuming that they did not get stuck in a dead-end).

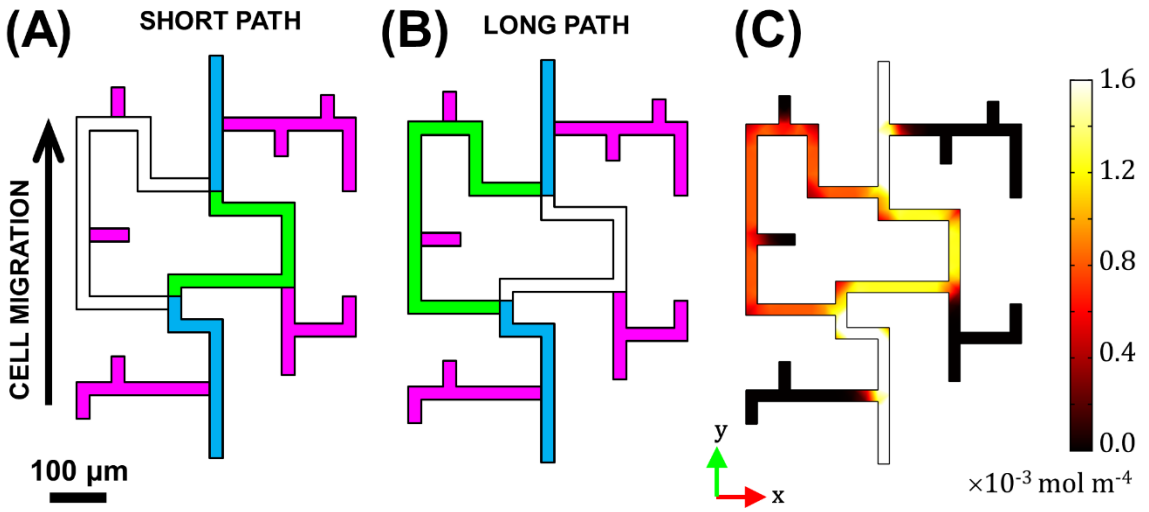

Figure 2.3 Illustration of possible path choices available to the cells in the microfluidic maze. Blue = common paths; Pink = dead ends. (A) Short path labelled in Green; (B) Long path labelled in Green; (C) PDGF-BB gradient magnitude calculated from COMSOL. The maze entrance is at the bottom, and its exit is at the top..

Since the fibroblasts migrated in response to a concentration gradient of PDGF-BB established inside of the maze, we characterized the relative difference in the chemotactic driving forces between the two paths *via* a COMSOL simulation (see **Figure 2.3**C). The chemoattractant concentration in the maze increased from the zero boundary condition at its entrance (where the cell seeding area was) to 50 ng mL^{-1} at its exit, in

order to match the experiment. The resulting *global* gradient, shown in **Figure 2.3**C, was about 1.5 times higher in the short path than the long path, mainly due to the length difference between them. Therefore, it would be logical to expect that the cells would be more likely to select the shorter path, in order to ascend the steepest gradient possible.

To test whether the above prediction is valid, the cells were allowed to migrate across the maze in response to two different PDGF-BB concentrations at the exit: 25 and 50 ng mL^{-1}. Manual tracking was used to collect statistics on their positions in the maze, throughout the duration of each experiment (see video: *https://vimeo.com/234413123*). Moreover, we also recorded the sequence in which the cells entered the maze and made their directional decisions once inside.

2.4.1 Experimentally-observed Effects of Cell Sequence on the Fibroblasts Directional Decision-Making

Overall, we found no statistically significant differences between the two PDGF-BB tested concentrations; and the shorter path was indeed preferred over the longer path for the leading cells that were the first to arrive at the bifurcation (see **Figure 2.4** A). The distribution between the short and the long paths was approximately 60-40%, when only these cells were considered. However, surprisingly, if all the cells entering the maze were taken into account (regardless of their order), the directional bias disappeared, and the prediction was no longer valid (see **Figure 2.4**B).

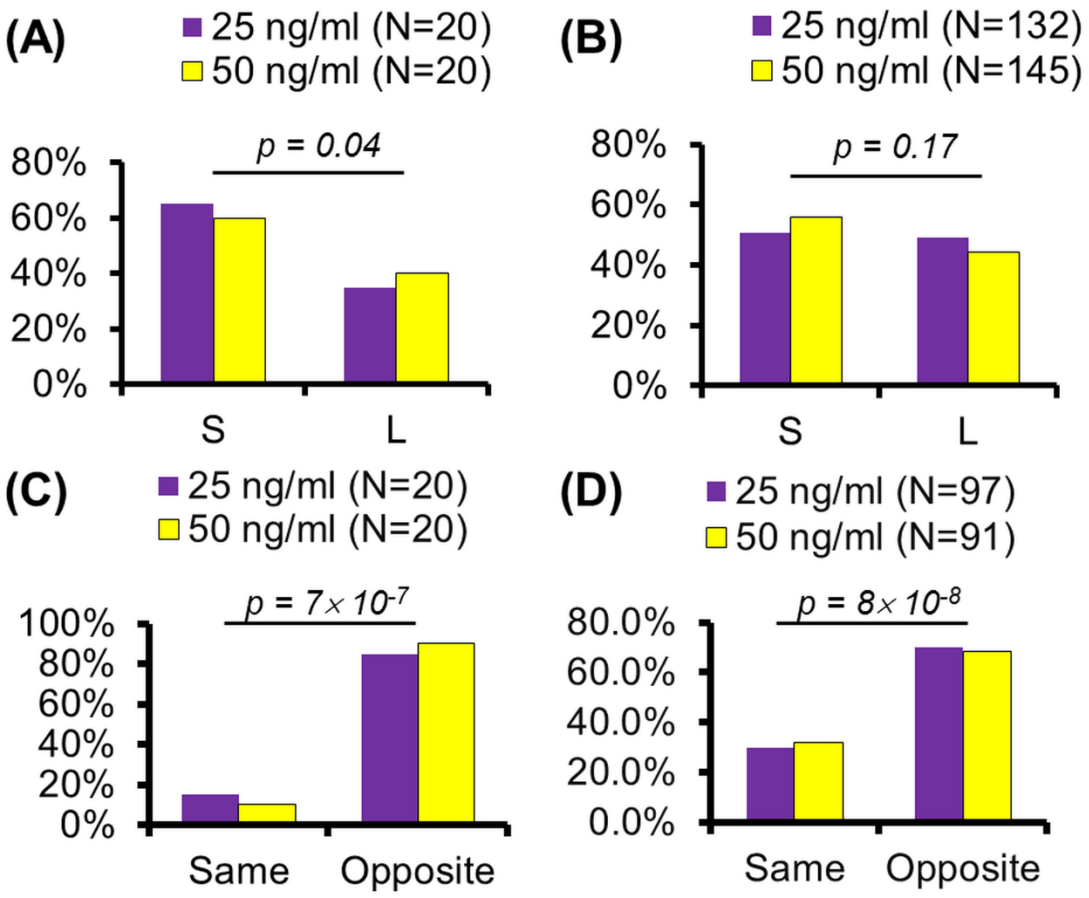

Figure 2.4 (A) Directional choices of the first cells to reach the maze bifurcation (S=short path, L=long path). (B) Directional choices of all cells reaching the maze bifurcation, regardless of order. (C) Directional choices of the first two cells reaching the maze bifurcation, when the cell sequence is taken into account. (D) Directional choices of any two consecutive cells to reach the maze bifurcation. N indicates the number of cells (A&B) and sequences (C&D) being counted. N is low in case of (A) & (C) since only first and second cells were considered. N is high in case of (B) & (D) since all cell orders were taken into account. P-values are calculated using the Binomial Test with the statistical level of 0.05.

In order to investigate this curious phenomenon further, we considered the sequence in which the cells arrived at the bifurcation. This type of analysis showed that the cells alternate their directional choices between the long and the short paths (see videos *https://vimeo.com/234413123* and *https://vimeo.com/234413129*). Hence, we defined a binary variable for either 'opposite' or 'same' choices made by the leading-following cell pairs, and used the binomial test to quantify their bias. **Figure 2.4**C shows

that most of the cell pairs chose an opposite path relative to each other, when only the *first* two cells that entered the maze were considered. Likewise, **Figure 2.4**D shows that the trend remained the same when the choices of *any* two consecutive cells were considered. In fact, the statistical analysis showed that in both cases the cells were biased towards the opposite choice with a >99% confidence.

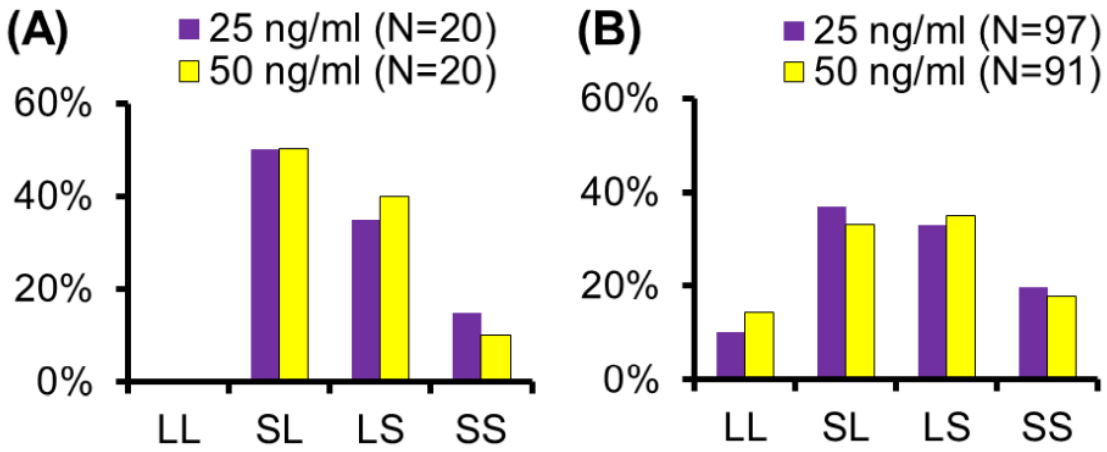

Figure 2.5 Detailed breakdown of the directional decision sequences displayed by the fibroblasts in the maze. (A) Directional choices of the first two cells reaching the maze bifurcation, when the cell sequence is taken into account. (B) Directional choices of any two consecutive cells to reach the maze bifurcation, when the cell sequence is taken into account. N indicates the number of sequences being counted.

Specially, **Figure 2.5**A shows that there was a slight bias (~ 50% of the occurrences) towards the short-long decision, because the leading cells were likelier to choose the short path (as was shown in **Figure 2.4A**). The second likeliest case was long-short; followed by short-short, accounting for less than 10% of the occurrences. Finally, the long-long case happened with a negligible probability.

Similarly, the alternation of the directional choice persisted even with the subsequent cells. **Figure 2.5**B shows the probabilities of fibroblast directional decisions when the choices of any two consecutive cells are considered. Here, 'same' choice decisions were slightly more frequent, but the overall trend remained the same, and the

cells were more likely to choose the paths opposite to that of their predecessors'. Hence, we hypothesized that the observed alternation of the directional decisions was caused by a localized consumption of the chemoattractant by the individual cells. So, we performed image-based simulations in order to test this hypothesis.

2.4.2 Image-based Simulation of Localized PDGF-BB Consumption by the Cells in the Maze

In order to visualize how the individual fibroblasts modify the PDGF-BB localized concentration gradient established in the maze, phase microscopy time-lapse images were used to incorporate the effects of the presence of the cells into the COMSOL diffusion simulations. While the maze geometry remains static, the cell shapes and locations are obtained *via* image processing and are passed into the diffusion solver. The boundary conditions remain the same as in the steady state "no cell" model described in the Methods section, while the cell migration is updated at intervals of Δt = 15 min (corresponding to the experimental image acquisition times). The main difference here is that the PDGF-BB is depleted over time *via* a natural decay and *via* endocytosis by the fibroblast cells. Following Menon et al. and Haugh, these effects are represented by adding the following consumption terms to the COMSOL model: $-k_{decay}\, C_P$ everywhere in the maze, and $-k_{endocytosis}\, C_f\, C_P$ to the cells domains.(66, 67) Here, 'k' represents reaction rate constants, C_P is the local concentration of PDGF-BB and C_f is the fibroblast "density" – an analogue of a chemical species concentration in a continuum representation of the cells. However, since our model has discrete cells, we assume that $C_f = C_{f,max}$ (corresponding to $\bar{f}$ in Menon et al.), which is derived based on the carrying capacity of the fibroblast cells. Moreover, the diffusivity of the PDGF inside of the cells $D_{P,cell}$ was arbitrarily set to two orders of magnitude slower than in the channels, in order to simulate the effect of the chemoattractant diffusion being slowed down within the

cells. The physical values of the relevant model inputs are summarized in **Table 2.1**, and the idea behind the approach is shown in **Figure 2.6**A.

Table 2.1 Simulation Parameters Used in The Image-Based Model of PDGF-BB Consumption by Individual Fibroblasts

Parameter	Description	Value
$C_{P,exit}$	PDGF-BB concentration at the maze exit	2×10^{-6} mol/m^3
$C_{P,entrance}$	PDGF-BB concentration at the maze entrance	0 mol/m^3
$D_{P,maze}$	Diffusivity of PDGF-BB in the channels	1×10^{-10} m^2/s
$D_{P,cell}$	Diffusivity of PDGF-BB in the cells	1×10^{-12} m^2/s
$C_{f,max}$	Maximum Fibroblast "density"	0.1 g/cm^3
k_{decay}	PDGF-BB decay constant	2.78×10^{-5} s^{-1}
$k_{endocytosis}$	PDGF-BB degradation constant	0.555 cm^3 g^{-1} s^{-1}

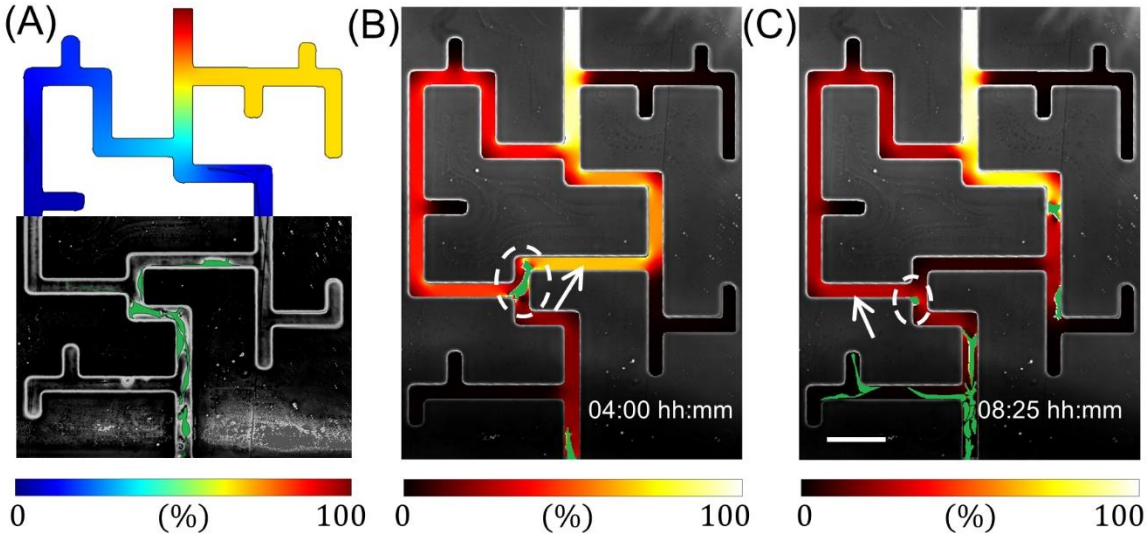

Figure 2.6 Image-based modeling of localized fibroblast effects on the PDGF-BB distribution within the maze. (A) Demonstration of the image-based concept. Upper half corresponds to the COMSOL simulation, with the PDGF-BB concentration scaled by the exit boundary condition concentration; while the lower half is the phase microscopy image of the fibroblasts (labeled in green) chemotaxing through the maze. (B) & (C) Simulation results of real-time modifications to the PDGF-BB gradient overlaid on the experimental microscopy images, showing the first and second cells' directional decisions at the maze bifurcation, respectively. Note that although the gradient is scaled between 0 and 100%, the actual value corresponding to the latter is chosen differently between the two timeframes in order to enhance visibility (for physical values see Video 6). Dashed white circle highlights the decision-making cell, while white arrow points to the higher chemoattractant gradient path chosen by the cell.

Additionally, we verified that the simulated PDGF diffusion kinetics matches those of experimental fluorescent dextran with a similar molecular weight (see video: *https://vimeo.com/285901346*); and that the presence of the individual cells in the maze's channels do not block the diffusion of the dextran (see *https://vimeo.com/285901737*).

The model showed that each fibroblast consumed the PDGF-BB in its locality (see *https://vimeo.com/277342732*), and thereby affected the distribution of the chemoattractant's concentration gradient significantly (see *https://vimeo.com/277342971*). This analysis also showed that the "leading" cell's choice is motivated by the steeper gradient in the shorter path, as is expected (see **Figure 2.6**B). Conversely, the "trailing" cell senses a steeper gradient in the longer path, because the

"leading" cell in front of it has consumed the chemoattractant in the short path (see **Figure 2.6**C). This finding supports the hypothesis that the presence of the individual cells can overcome the external chemotactic cues *via* self-generation of local gradients. However, given that tissue generation is a highly-proliferative process, we also wanted to explore the effects of cell mitosis on fibroblast migration.

2.4.3 Experimentally-observed Effects of Mitosis on the Fibroblasts Directional Decision-Making

For simplicity, we only examined non-dividing cells when collecting data for Figure 2.4

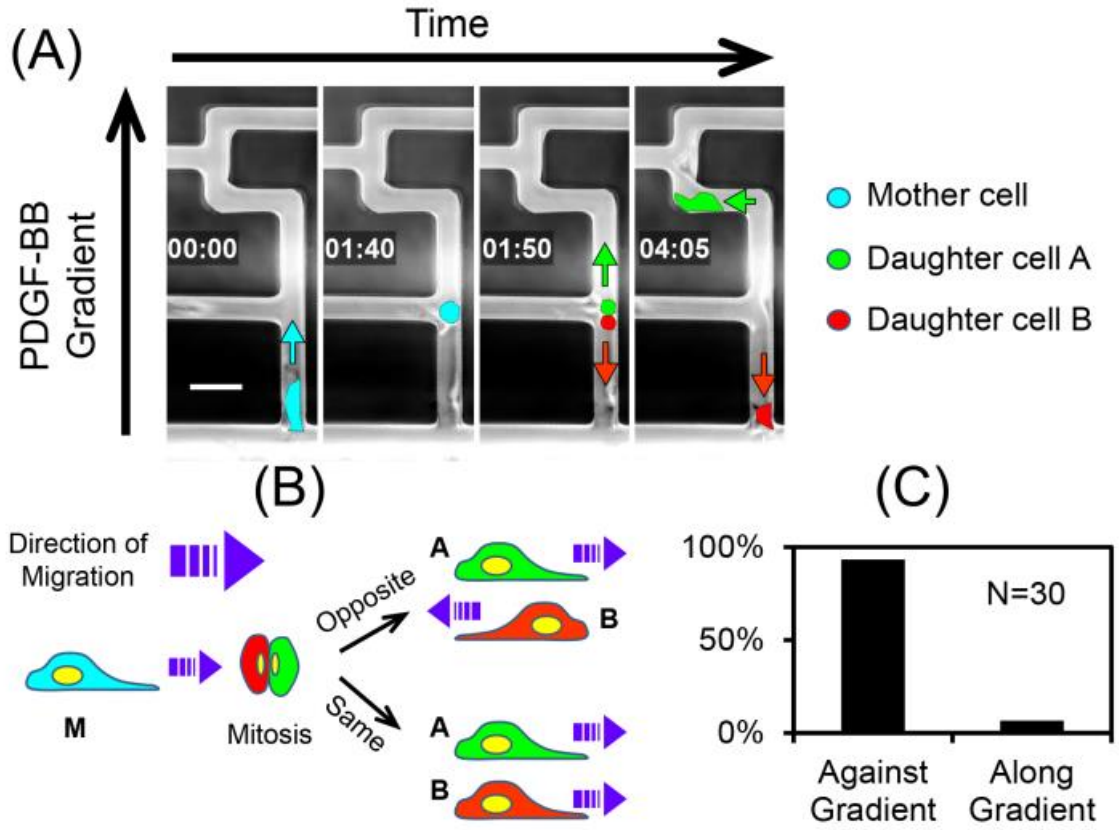

Figure 2.7 (A) Time-lapsed montage of cells undergoing mitosis when migrating in the maze. The cells were false-colored for visual recognition. Cyan, red, and green arrows show the direction of migration of the mother and the two daughter cells, respectively. The time is displayed as hh:mm. The scale bar is 50 μm. (B) Diagram showing two directional scenarios encountered by the two daughter cells. (C) Frequency of occurrence of the two directional scenarios shown in pane B.

and **Figure 2.5**. However, since tissue formation is a highly proliferative process, it is also interesting to examine how cell mitosis affects the fibroblast chemotaxis.

In the past, mitosis has been found to affect fibroblast migration under non-chemotactic conditions,(28, 52) while here we explored its effect on the cells' directional decision-making in the presence of PDGF-BB. To do that, the fibroblasts undergoing division were manually tracked and analyzed. **Figure 2.7**A shows a time montage of such an event occurring, while the mother cell was navigating the maze's common path from the entrance. This figure shows that after the division, one of the daughter cells continued along the positive PDGF-BB gradient path, while the second daughter went against it (in the opposite direction).

In overall, we observed two modes of the daughter cells' migration: either both went along the gradient (though often taking different paths through the maze, as in the cell sequence case), or one went along the gradient and the other against it (see **Figure 2.7**B). However, the probabilities of each mode differed significantly: only < 10% of occurrences for the former (**Figure 2.7**C, see video *https://vimeo.com/234413134*), versus >90% for the latter (see video *https://vimeo.com/234413136*). Furthermore, it was especially surprising to see that some of the daughter cells that went against the gradient did so despite the oncoming traffic of other migrating cells; and ultimately were able to exit the maze entirely, through the entrance (*https://vimeo.com/234413136*). Therefore, it is apparent that the mitosis-driven repulsion between the daughter fibroblasts is so great that it is able to overcome both the chemotactic forces and the "inertia" of the other cells migrating along the gradient. That is, in many instances the daughter cell has to squeeze past heavy oncoming traffic of densely-packed cells entering the maze.

Finally, we observed that the mitosis happened more frequently at regions in the maze that are closer to the entrance, and less frequently near its exit (**Figure 2.8**). This is likely because the threshold(14) at which fibroblast proliferation is induced corresponds to the lower PDGF-BB concentrations that are experienced by the cells near the maze entrance. Although cell mitosis has been found to be affected by micro-confinement,(68) we do not believe that this the case here; because, according to **Figure 2.8**B, the highest proportion of cell divisions per maze segment visits occurred in a dead-end (and not at the maze entrance, where the confinement was first encountered).

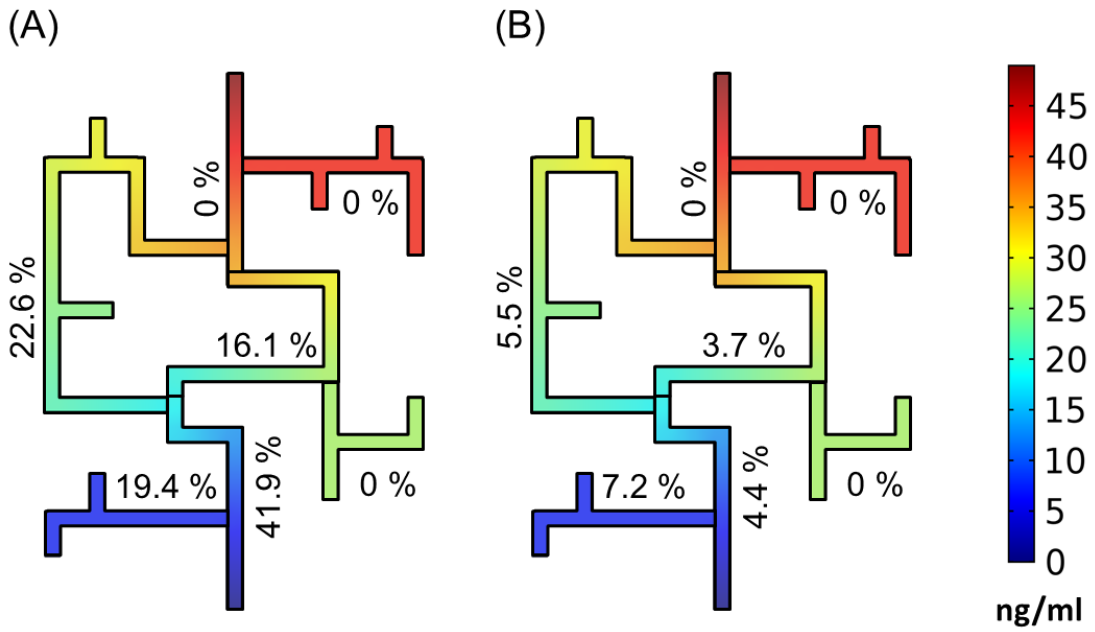

Figure 2.8 Spatial distribution of mitosis events in different maze segments, overlaid on the PDGF-BB concentration profile from COMSOL. (A) Divisions in a maze segment per total number of divisions in the whole maze. (B) Divisions in a maze segment per total number of cell visits into the same maze segment. Black lines indicate boundaries between the maze segments considered.

2.5 Discussion

This manuscript investigated fibroblast chemotaxis in tissue-mimicking microarchitectures, in order to understand how these cells influence each other's directional decision-making under microscopic confinement. Understanding these mechanisms is important to developmental biology, multiple tissue pathologies,(69-74) and regenerative medicine,(8) because fibroblasts are the primary cell type responsible for normal tissue homeostatic processes. For example, they are involved in collagen synthesis, the build-up of connective tissues (e.g., cartilage, bone), and wound healing in response to injury.(13, 75) Therefore, characterizing their migratory behavior in microscopic pores can lead to improved tissue patterning and product uniformity. Subsequently, since tissue generation is a highly dynamic and proliferative process, we

hypothesized that cell-cell interactions and cell division should affect fibroblasts' decisions.

To test the hypothesis, we induced fibroblast chemotaxis in microfluidic mazes, and collected migration statistics as a function of the sequence at which the cells arrived at the path bifurcations. Unexpectedly, we found that consecutive cells alternate their decisions in order to avoid following each other, even if that means choosing the longer path through the maze (i.e., a weaker chemoattractant gradient). This seems to be contradictory to studies performed in similar mazes, but with cancer cells and immune cells.(23, 76) However, a major difference is that those were single cell studies, while ours were multi-cell. Therefore, one possible explanation is that the leading cell alters the local chemoattractant concentration by consuming the PDGF-BB (at a rate higher than it is replenished *via* diffusion). Subsequently, choosing an alternate path may in fact result in a steeper local gradient for the subsequent cells. Another possible explanation is the integrin migration tracks that fibroblasts have been known to leave behind them.(28, 57) However, this is less likely, as those findings report cells following each other's migration tracks, not avoiding them. Moreover, fibroblasts are known to attract each other *via* fibroblast growth factor and ECM degradation proteinase release.(15) Therefore, it is surprising to see them avoiding each other to such a great extent that they would contradict the optimal route expected from the PDGF-BB gradient.

Nonetheless, our simple image-based model is able to explain the experimental observations by using published reaction kinetic parameters (shown in **Table 2.1**),(66, 67) and two simplifying assumptions. Namely, the first assumption is that the endocytosis of PDGF occurs as a pseudo-first order reaction: $-k_{effective} C_P$, where the effective reaction rate constant $k_{effective} = 0.0555/s$ is a product of two other constants,

$k_{endocytosis}$ and $C_{f,max}$. This simplification is necessitated by the fact that the published PDGF endocytosis models treat the fibroblasts as a continuous species with a concentration, while our model has discrete cells (which makes it unobvious what value to use for C_f). However, it does yield a reasonable value for an *estimated* maximum receptor-mediated endocytosis uptake rate per cell of ~ 1 x 10^2 molecules/minute/cell. Moreover, a parameter sensitivity analysis of the model showed robustness in its predictions (see **Appendix A**).

The second key assumption in our model is that the PDGF diffusion occurs much faster than does the cell migration. This is necessary, because the cell geometries are updated at the frequency at which the images are captured by the microscope, once every $\Delta t_{microscope}$ = 15 minutes; while the time resolution in the diffusion solver is chosen to be $\Delta t_{simulation}$ = 1min (based on the observation that a finer time step did not improve the results). The assumption is valid, because fibroblast cells in our maze have an average speed of 2-4 μm/min (or 0.03-0.06 μm/sec); whereas, the diffusion coefficient used to represent the PDGF-BB (MW = 25 kDa) in an aqueous solution was $D_{P,maze}$ = 1 x 10^{-10} m^2/s.(65) A rough estimate of the PDGF-BB diffusion speed can be calculated by dividing $D_{P,maze}$ by a characteristic length scale, which can be taken as the width of the maze channel. Furthermore, the result is multiplied by a factor of 4, to account for two-dimensional diffusion. This yields ~16.7 μm/s. Hence, the PDGF-BB diffusion is about 2 orders of magnitude faster than the cell migration.

Additionally, we demonstrated that the division of the parental fibroblasts was highly asymmetric in terms of the migration choices of their descendants. This was evidenced by one of the daughters being more likely to move against the chemoattractant gradient, often disregarding the oncoming traffic created by the other cells in the maze.

The finding is consistent with previous reports of fibroblast daughter cells creating tracks that are mirror images of each other,(77) when migrating on a gold particle-coated substrate;(28) and also, migrating in opposite directions on a collagen matrix.(52) However, in the latter work, the daughters separated only temporarily when the cells divided on fibrin (instead of on collagen), and eventually came back together along the same path (which was not the case in our study). Therefore, the effect appears to be substrate-dependent. Moreover, these experiments were conducted in the absence of a chemotactic gradient and without micro-confinement, so they are not a one-to-one comparison with our work.

Such heterogeneity between sibling cells is typically attributed to differences in the relative expressions of chemoattractant receptors on their surfaces. The case of the fibroblast PDGF-BB-driven chemotaxis is also a receptor-mediated process.(15, 78) Therefore, it is possible that there were differences in PDGF receptor expression levels between the sibling cells. Similar asymmetric receptor distributions have been observed in migrating cells before.(56) Hence, it would be interesting to image the PDGF-BB receptor distribution in the fibroblasts membranes at the time of mitosis. However, immunofluorescent labelling of the PDGF receptors would also block the receptors sites, subsequently hindering the chemotaxis. Therefore, non-blocking fluorescent tags are needed.

In summary, our study provides insight into how individual fibroblasts affect each other's decision-making processes during chemotaxis in spatially confined microarchitectures. A limitation of this work is that the pore sizes are much larger, and the substrate (poly-D-lysine coated glass) is much stiffer, in the maze compared to a typical extracellular matrix. Therefore, the results presented here are not a one-to-one

comparison with the extracellular space of *in vivo* tissue. Nonetheless, they still carry practical implications for both understanding the biology of chemotactically driven morphogenesis processes *in vivo*, as well as for artificial tissue design *in vitro*. For example, scaffold architectures could be optimized for achieving desired cell distributions by taking into account how the fibroblasts alternate the paths they take at bifurcations. Furthermore, our model could help to select cells with a higher migration potential by selectively isolating the cells that choose the shorter path through the maze. Finally, this study raises some critical questions about what is behind the discovered effects that compete with the chemotaxis. For example, the reason why the mitotic cells display highly distinctive directional choices may be either due to a difference in receptor expression in the daughter cells, or due to the migration tracks left by their parent. Hence, these effects, and other possibilities, need to be investigated further.

2.6 Conclusions

In conclusion, we conducted a study of fibroblast interactions during chemotaxis in a microfluidic maze made to resemble *in vivo* tissue pores. Through this study, we have demonstrated that the directional decisions of these cells are influenced by the sequence in which they arrive at path bifurcations, and that their path choices alternate depending on each predecessor's decision. Also, we showed that cell division occurring during the chemotaxis yields daughter cells with directional bias distinctive from that of their siblings. In addition, in both cases, the fibroblast-fibroblast influence appeared to overcome the directional guiding of the chemoattractant gradient established within the maze. We presented a hypothesis that the sequence effect is likely due to a localized chemoattractant consumption by the leading cells, while the mitotic effect could be caused by an asymmetric PDGF-BB receptor inheritance by the two daughters.

Moreover, we confirmed the former *via* image-based modeling of PDGF-BB consumption by the individual fibroblasts; however, further investigations are needed to validate the latter. Nonetheless, the presented results carry practical implications for developmental biology, multiple pathologies, and tissue engineering.

CHAPTER 3

RELATIVE IMPORTANCE OF DIFFERENT DIRECTIONAL CUES ON THE DIRECTIONAL DECISION OF FIBROBLASTS

3.1 Introduction

During migration through tissues, cells do not only encounter different degrees of physical confinement (79, 80) but also experience varying levels of biochemical agonist gradients.(20, 81) Hence, the physical surroundings which the cells encounter during the migration also exhibit an important role in affecting the direction of their migration.(82) Therefore, the interplay between these factors is crucial to unraveling the underlying biology mechanisms behind the migration directionality and achieving subsequent control of cell behavior.

Recent cell migration assays are mostly assisted by microfluidic technologies, which capitalize on the use of micron-sized channels in creating confined environments and stable gradients. The directional decision of cells has been found to be dependent on the channel width,(25, 26) which are directly related to gradient steepness; contact-guidance;(26) and cell division.(83) However, these studies have little or no comparison between the relative importance of the different directional cues on the cell migration. This is especially important since cells usually encounter various directional cues at the same time when they navigate the tissue pores. Moreover, most of the studies overlooked the effect of the cell-cell interaction on the cell decision making.

In order to address this missing knowledge, we use a migration model which consists of bifurcated maze channels of varying widths. A gradient of platelet-derived growth factor-BB is used to induce the migration of fibroblasts into the mazes. The

migrating cells are exposed to various external cues including chemoattractant gradient, channel width bias, and the contact guidance. The gradient dynamic inside the mazes induced by the cell-cell interaction is calculated using a numerical simulation method termed image-based modeling, which was developed earlier by Alam et al.(43) With this system, we were able to compare the relative importance of the different directional cues, and for the first time rank them basing on their strength in attracting and guiding the cell directionality.

3.2 Methods

3.2.1 Materials

Polydimethylsiloxane (PDMS) Sylgard 184 was purchased from Dow Corning (Midland, MI). Negative photoresist SU-8 was purchased from Microchem (Newton, MA). Bovine collagen Type I 3mg ml^{-1} solution (PureCol) was purchased from Advanced Biomatrix (San Diego, CA). Recombinant rat platelet-derived growth factor-BB (PDGF-BB) was purchased from R&D Systems (Minneapolis, MN). Culture media was prepared from Minimum Essential Medium (MEM) (Sigma, MO) supplemented with 10% (v/v) fetal bovine serum (FBS) (VWR, Radnor, PA), and 1% (v/v) penicillin-streptomycin (10,000 U mL^{-1}) (Thermofisher, Waltham, MA). Basal media was composed of MEM supplemented with 1% (v/v) penicillin-streptomycin. For incubation in 5% CO_2 atmosphere, media was buffered by 26 mM sodium bicarbonate (Sigma, MO). CO_2-independent media buffered by 20 mM HEPES (Sigma, MO) was used for the microscope stage-top experiment.

3.2.2 Device Concept

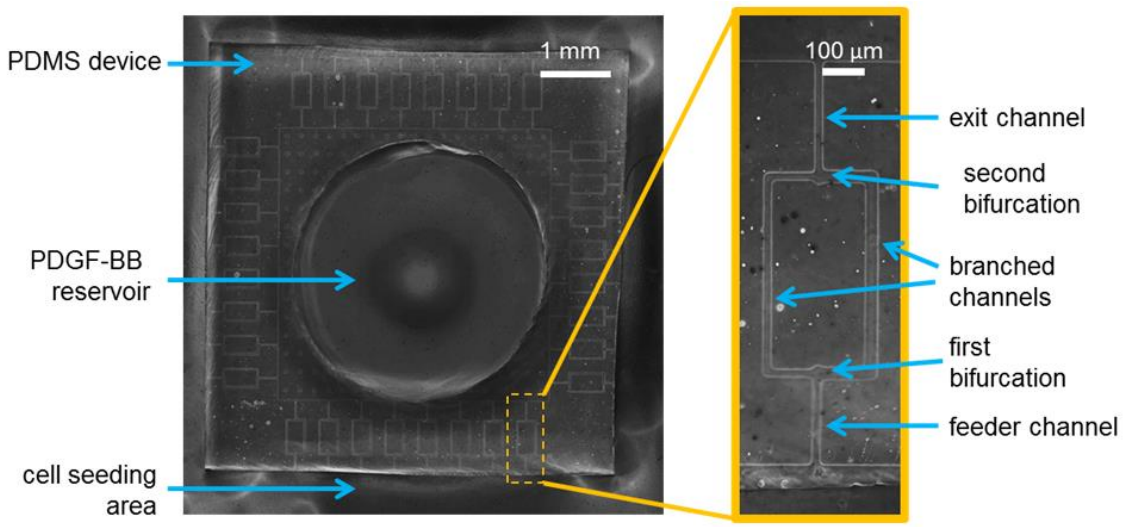

Figure 3.1 Phase-contrast microscopy showing the device concept. Inset is a magnified view of a single maze channel.

The device (made from PDMS) is consisted of an array of 32 20-µm-tall microfluidic maze channels, which connect a central reservoir of the chemoattactant PDGF-BB with a cell seeding area surrounding the device (Figure 3.1). Each maze is consisted of two 20-µm-wide common channels, one feeder and one exit. The feeder channel is bifurcated into two branched channels of the same length but varying widths – ranging from 20 to 75 µm. The two branches merge at the second bifurcation which leads to an exit channels of 20-µm wide. With this setup, cells are allowed to migrate from the cell seeding area towards the central reservoir, following a chemmoattractant concentration gradient established inside the maze channels.

3.2.3 Device Fabrication

The mold for the device was fabricated from SU-8 photoresist using a custom-build mask aligner (Appendix A). The mask for the device was sketched using AutoCAD (Autodesk, Mill Valey, CA) and printed at 20,000 dpi on a transparency (Fineline Imaging, Colorado

Springs, CO). SU-8 2010 was spin coated at 2000 rpm on a 4-in Silicon wafer, exposed to UV light, and developed yield 20-μm-tall microfluidic channels. The devices were fabricated using soft lithography technique similar to the one used in previous chapter. The internal surface of the microfluidic channels were treated with collagen Type I to improve the cell attachment.

3.2.4 Cell Preparation

Mouse embryo NIH/3T3 (ATCC® CRL-1658TM) fibroblasts were purchased from ATCC (Manassas, VA). Prior to being transferred to the microfluidic device for the migration experiments, the cells were incubated in the culture media inside of T75 flasks. The flasks were kept at 37 °C and in a humidified atmosphere of 5% CO_2 in air. The culture media was changed every two days to ensure normal cell growth. Prior to the migration experiments, the cells were trypsinized from the T75 flasks and loaded into the chip, with a seeding density of about 50,000 cells cm^{-2}. The chip was incubated at 37 °C under 5% CO_2 for 6 h to allow cell attachment. Then the cells were cultured in serum-starved media (MEM supplemented with 1% penicillin-streptomycin) for 6 hours.

3.2.5 Cell Migration Experiment

At the start of the experiment, cell culture media in the chip was replaced with CO_2-independent basal media buffered by HEPES. 20 μL of basal media supplemented with 50 ng mL^{-1} PDGF-BB was then added into the central reservoir of each device. The experiment setup is similarly described in the previous chapter of the thesis. Typically, the device was mounted on a condition chamber which is equipped with a temperature regulation system and a humidfied environment. Time-lapse phase-contrast imaging of the fibroblast migration was performed using a fully automated Olympus IX83 microscope fitted with a 10X phase-contrast objective (Olympus, Japan), a CMOS

camera (Orca Flash 4.0 V2, Hamamatsu, Japan), and an autofocus module (ZDC, Olympus, Japan). Time-lapse images were automatically captured at a 15 min interval for a duration of 24 hours. For each device at each time step, 36 tile images were acquired at different locations, stitched, and stabilized using an in-house Matlab® 2016b code (MathWorks, Inc., Natick, MA).

3.2.6 Data Analysis

Migratory cells were tracked using the Manual Tracking plug-in for ImageJ software (National Institutes of Health).(64) The directional decision chosen by each individual cell at the bifurcation was determined *via* manual observation. Quantitative data of cell sequences was generated using an in-house Matlab® 2016b code (MathWorks, Inc., Natick, MA). Significance level was determined by using a non-parametric test for a binomial distribution, unless otherwise stated. Statistical significance was set as $p < 0.05$.

3.2.7 Simulation of Transient PDGF-BB Gradient in the Presence of Migrating Cells

For a complete description of the model see our paper in print.(83) The PDGF-BB concentration gradient established between the two ends of the maze was simulated numerically using COMSOL 5.3a Multiphysics (COMSOL, Burlington, MA). Constant concentration boundary conditions, corresponding to the experiment, were set to $C_{P,exit}$ = 50 ng mL^{-1} PDGF-BB at the maze exit, and zero at the maze entrance. A diffusion coefficient of $D_{P,maze} = 1 \times 10^{-10}$ m^2 s^{-1} was used to represent the PDGF-BB (MW = 25 kDa) in an aqueous solution.(65) Chemoattractant gradient values at every point in the maze were calculated from the vector magnitude of two components, x-axis (horizontal) and y-axis (vertical), both of which increased towards the higher concentration of PDGF-BB.

Phase-contrast microscopy time-lapse images were used to incorporate the effects of the presence of the cells into the COMSOL simulations. While the maze geometry remains static, the cell shapes and locations are obtained *via* image processing and are passed into the diffusion solver. The cell migration is updated at intervals of $\Delta t = 15$ min (corresponding to the experimental acquisition times). Both the natural decay of PDGF-BB and its depletion *via* endocytocis by fibroblasts are taken into account. These effects are represented by a decay constant $k_{decay} = 2.78 \times 10^{-5}$ s^{-1} and a endocytosis rate constant $k_{endocytosis} = 0.555$ cm^3 g^{-1} s^{-1}, respectively. (66, 67) Hence, the following consumption terms are added to the COMSOL model: $-k_{decay} C_P$ everywhere in the maze, and $-k_{endocytosis} C_f C_P$ to the cells domains. Here, 'k' represents reaction rate constants, C_P is the local concentration of PDGF-BB and C_f is the fibroblast "density" – an analogue of a chemical species concentration in a continuum representation of the cells. However, since our model has discrete cells, we assume that $C_f = C_{f,max} = 0.1$g cm^{-3}(corresponding to $\bar{f}$ in Menon et al.), which is derived based on the carrying capacity of the fibroblast cells. Moreover, the diffusivity of the PDGF *inside* of the cells $D_{P,cell}$ was arbitrarily set to two orders of magnitude slower than in the channels or 10^{-12} m^2 s^{-1}, in order to simulate the effect of the chemoattractant diffusion being obstructed by the cells.

3.3 Results

3.3.1 Experimental Observations of Cell Sequence Dependence on Bifurcation Branch Width Asymmetry

In our prior work in Chapter 2, we demonstrated that trailing cells tend to make directional decisions *opposite* from those of the leading cells in front of them, when encountered with a bifurcation of different channel *lengths*. For example, when the latter

takes a shorter path, the former is likely to take a longer path and *vice versa*. However, differences in the *widths* of the bifurcation "branches" have not yet been considered; but instead, microfluidic channels of identical widths – similar in size to that of a single cell - were used. Therefore, the current work aims to assess how the directional decision-making is affected by the channel width differences. To do that, migration of fibroblasts was induced inside of simplified microfluidic "mazes", which contained bifurcating channels of the identical lengths, but of different widths. The left branch of the bifurcation was always kept 20 μm wide, while the width of the right branch was varied as follows: 20 μm (i.e., 1X of the left branch), 30 μm (i.e., 1.5X of the left branch), and 60 μm (i.e., 3X of the left branch). This is shown in **Figure 3.2**a.

Initially, we quantified the cells decision-making at the first bifurcation, which is closest to the maze entrance. In **Figure 3.2**b, the first cells to encounter the bifurcation displayed no obvious preference between the two branches of the identical widths ($p>0.05$). On the other hand, a significant bias towards the wider branch was observed, when there was a width difference between the two bifurcation branches. In fact, **Figure 3.2**b shows that the larger the width difference between the two branches, the higher the bias towards the wider channel. This is evidenced by the trend in the bias confidence level, which equals to $p = 3\times10^{-6}$ for 1.5X width difference, and 4×10^{-7} for 3X width difference. Furthermore, the same trend still holds true even when *all* individual cells to enter the maze are considered, not just the first two (see **Figure 3.2**c). Overall, the results shown in **Figure 3.2**b-c suggest that a wider, open space is more attractive to the migrating fibroblasts, than is the confinement of the 1X branch width.

Next, we assessed whether cell-cell interaction plays a role in the fibroblast directional decision-making. This is done by accounting for the cell *sequences*, when

analyzing the bifurcation branch choices. For clarity, when *both*, the leading and the trailing cells, commit to the same path, is referred to as the "same" sequence; while the case when the cells make *different* choices from each other, is termed as "opposite" sequence. This notation is illustrated in **Figure 3.2** d.

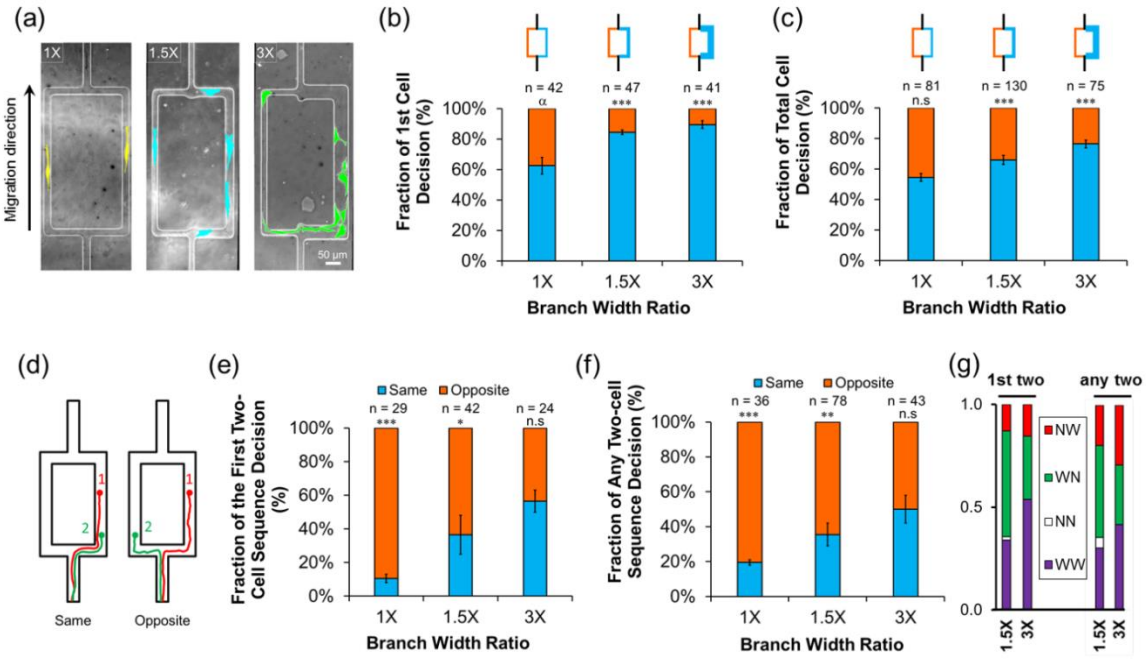

Figure 3.2 Fibroblast directional decision-making statistics when encountered with asymmetric branch widths. (a) Phase contrast microscopy images of cells migrating in mazes, showing the three different branch arrangements explored in this study: 1X, 1.5X and 3X. Cells are false-colored for increased visibility. (b) Fraction of the decision bias made only by the *first* cells to encounter the bifurcation, as a function of "Branch Width Ratio". The latter is the ratio between the width of the wider branch relative to that of the narrower branch. (c) Fraction of the decision bias made by *any* individual cells to enter the maze. (d) Graphic illustratring the definition of the "same" and "opposite" directional decision sequences made by *two consecutive cells*. (e) Fraction of the decision *sequences* made by only the *first* two cells to encounter. (f) Fraction of the decision sequences made by *any* two consecutive cells. (g) Fraction of decision sequences made by the *first* two cells, and by *any* two consecutive cells, with respect to the branch width ratio . WW: both the leading and the follower cells select the *wider* branch; NN: both cells select the *narrower* branch; WN: the leading cell selects the *wider* branch, while the trailing cell selects the *narrower* branch; NW: the leading cell selects the *narrower* branch while the follower cell selects the *wider* branch. In (b),(c): 'n' indicates the number of cells making a decision; in (e), (f): 'n' is the total number of sequences; 'n.s.' is not statistically significant. α: $p < 0.1$; $*$: $p < 0.05$; $**$: $p < 0.01$; $***$: $p < 0.001$.

Like in **Figure 3.2**b, we initially considered the decisions made only by the *first two* cells to encounter the bifurcation. From this analysis, it was observed that as the difference in the branch widths increased, the first two cells had a higher tendency of

making the *same* choice (see **Figure 3.2**e). Furthermore, like before, the choices were biased towards the *wider* branches (see **Figure 3.2**g). The same trend persisted when the sequences made by *any* two consecutive cells were considered (see **Figure 3.2**f). For this case, the "opposite" sequence appeared to be slightly more dominant (e.g., compare the 3X bars between **Figure 3.2**e&f). This may suggest that the follower cells begin to detour into the narrower branches (despite the preference for the wider ones), when the cell population in the wider branches is high (see how the fraction of 'opposite' sequences increases with the greater bifurcation width ratio, in **Figure 3.2**g).

3.3.2 Image-Based Modeling of the Localized Chemo-Attractant Gradient in the Bifurcated Mazes

Next, we wanted to explain the observed experimental behavior *via* computational image-based modeling. In our prior work, the decision-making of fibroblasts during chemotaxis in micro-confined environments was found to be largely influenced by the changes in localized concentration gradients of PDGF-BB (CHAPTER 2). Specifically, the fibroblasts were found to influence each other's decisions *via* PDGF-BB consumption (i.e., endocytosis), and *via* blockage of its transport in the channel space. Hence, we applied the same image-based modelling approach to the three different channel-width biases mentioned above: namely, 1X, 1.5X and 3X. The simulation results for this are shown in **Figure 3.3**.

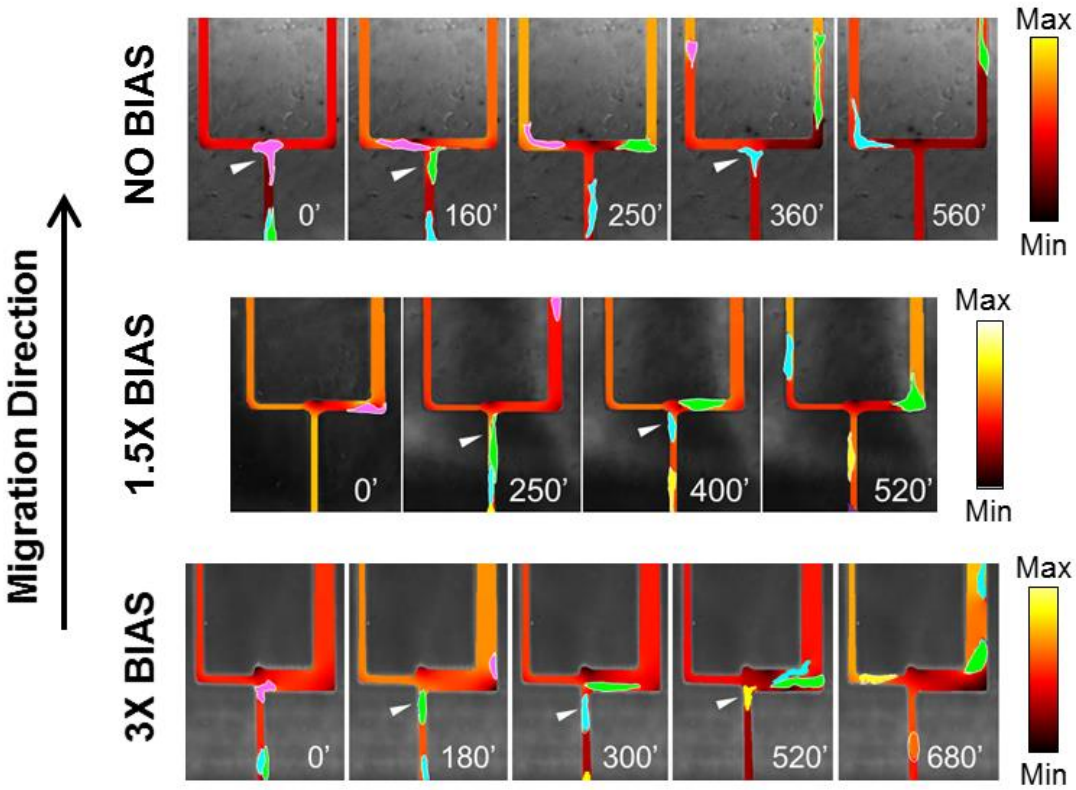

Figure 3.3. Image-based simulation of PDGF-BB gradient inside of different width bifurcations, and in the presence of traveling cells. TOP: time montage showing the gradient dynamics inside of a symmetric 1X bifurcation. MIDDLE: time montage showing the gradient dynamics inside of an asymmetric 1.5X bifurcation. BOTTOM: time montage showing the gradient dynamics inside of an asymmetric 3X bifurcation. White arrows indicate the cells that are about to make a directional choice. Cells are false colored for visibility and to color-code the cell order: PURPLE - first cell, GREEN - second cell, CYAN - third cell, YELLOW - forth cell, etc.

3.3.2.1 Fibroblasts' Preference for the Wider Branches is Not Dictated by the PDGF-BB Gradient. From **Figure 3.2**, it is evident that the *1st* cells to encounter the bifurcation experience no discrepancy in the gradient between the two branches, regardless of their width. However, as mentioned previously, the fibroblasts do tend to prefer the wider branches with a high probability. Hence, this preference appears to not be influenced by the PDGF-BB gradient (at least not in the case of the *1st* cells). Additionally, there was also a trend in the average decision time for these cells. Specifically, it took them: 172 ± 122 min (n = 27), 122 ± 81 min (n=17), and 109 ± 60 min (n=27) to commit to a branch, for the 1X, 1.5X and the 3X cases, respectively. In other words, the cells decide which way to go faster, when there is a higher disparity in the width between the two branch choices. This makes sense, given that the larger the width, the stronger the directional cue of the wide branch appears to motivate the fibroblasts. Furthermore, longer decision times are expected for the 1st cells to face the symmetrical bifurcations, because they may need to do a more thorough evaluation of which direction is preferable (Chapter 2). And given all things being equal, their decision is ultimately prone to random selection, rather than being guided by any directional cues.

3.3.2.2 Trailing Cells Alternate Paths Less in Asymmetric Mazes than in Symmetric Ones. When the cell sequence is taken into account, however, the trailing cells are expected to see a significantly lower PDGF-BB gradient in the branches chosen by the leaders. This is due to the consumption of the chemoattractant, and to the obstruction of its transport in the narrow branches. Thus, the 2^{nd} cells should have a higher tendency of selecting the opposite path, instead of trailing the 1^{st} cells. As expected, **Figure** 3.3 - TOP PANE shows that this holds true for the symmetric bifurcations: the 2^{nd} cells to encounter them take the opposite path at a high frequency of 89.5 ± 2.5% ($p = 8\times10^{-6}$). However, in the case of the asymmetric 1.5X and 3X branch width ratios, there is a higher number of the 2^{nd} cells taking the same path as the 1^{st} ones. This could be explained by the diffusion of the chemoattractant being less limited in the wider branches, since the chemical can go around the leading cells easier. Therefore, the gradient differences between the two branches are less obvious to the trailing cells in the asymmetric bifurcations (see 250' and 180', MIDDLE and BOTTOM panes, respectively, **Figure 3.3**) than in the symmetric ones (see 160', TOP pane, **Figure 3.3**). Consequently, the availability of a wider space for migration outweighs the minute differences in the chemoattractant gradient, for these cells.

3.3.2.3 Sufficiently Low PDGF-BB Gradient Outweighs the Desire to Migrate into Wider Channels. Similarly to the other *symmetric* cases, the 3rd and 4th cells to enter such bifurcations follow the alternating decision-making pattern that is driven by the steeper gradient (see 360', TOP pane, **Figure 3.3**). In the *asymmetric* cases however, the behavior varies depending on the accumulation of cells in the wider branches. For example, a 3rd cell in the 1.5X bifurcation (see 400', MIDDLE pane, **Figure 3.3**), is faced with a *significantly lower* gradient inside the wider branch when compared to the narrower one. This is due to the presence of both the 1st and the 2nd cells in the wider branch at the same time. Together, the two cells both consume and block the PDGF-BB so much, that the 3rd cell behind them opts to migrate into the narrower path (despite it being less desirable). A similar situation occurs in the 3X bifurcation, where the simultaneous presence of the 2nd and 3rd cells in the wider branch (see 520', BOTTOM pane, **Figure 3.3**), ultimately diverts the 4th cell into the narrower less-desirable route (680', BOTTOM pane, **Figure 3.3**). Hence, there appears to be some minimal threshold of the PDGF-BB gradient that the cells consider unacceptable, and go into the narrower path instead.

What has been shown so far is that the difference in the gradient steepness has a smaller influence on the fibroblast directional decision-making process, when compared to the spatial effect of the difference in the branch width. From this standpoint, it may be concluded that the chemoattractant gradient is *secondary* to the branch width effect, when it comes to influencing the directionality of cell migration.

3.3.3 Division Increases the Likelihood of Migration into Narrower Channels in Width-Asymmetric Bifurcations

From previous studies it is known that mitosis influences the direction of migrating cells: specifically, it has been shown that daughter cells have a high chance to move in *opposite* directions following cell division.(28, 29) However, these studies were conducted only in uniform concentration environments, which is not representative of the physiological cell migration. Consequently, our own study in Chapter 2 demonstrated that this effect remains true even when one of the daughters has to go against an established chemoattractant gradient. Yet, the influences of the geometrical constraints on the cell division, and subsequently on their migration, have not yet been explored. To that end, here we aim to provide a closer look at how mitosis influences the fibroblast migratory decisions in the *width-asymmetric* bifurcations.

First, we tracked the amount of divisions occurring at different locations in the mazes. According to **Figure 3.4**a, the fraction of divisions occurring in the 3X bifurcation is significantly higher than in the 1.5X ($p = 0.014$, between the 1.5X and the 3X) and the 1X bifurcation, while the latter two are statistically similar to each other ($p = 0.32$, between the 1X and the 1.5X). Additionally, the extent of divisions was also found to vary between the different locations in the maze. For example, most of the divisions occur at the part of the maze near the entrance, which essentially falls into the lower range of chemoattractant concentrations. This agrees with our previous results reported in Chapter 2. Additionally, we also observed that as the two daughters split up, they move in opposite directions similar to the previous findings. However, in our width-asymmetric system, one of the daughters has a high chance of migrating into the narrower branch (see **Figure 3.4**b), which has a very low probability of occurrence in the case of the undivided cells that mostly avoid the narrower branches (**Figure 3.4**c). Thus,

this result suggests that the divisions can circumvent the repelling nature of constrained spaces in microscopic tissue pores, and thus are able to widely distribute the cells in a variety of spatial dimensions.

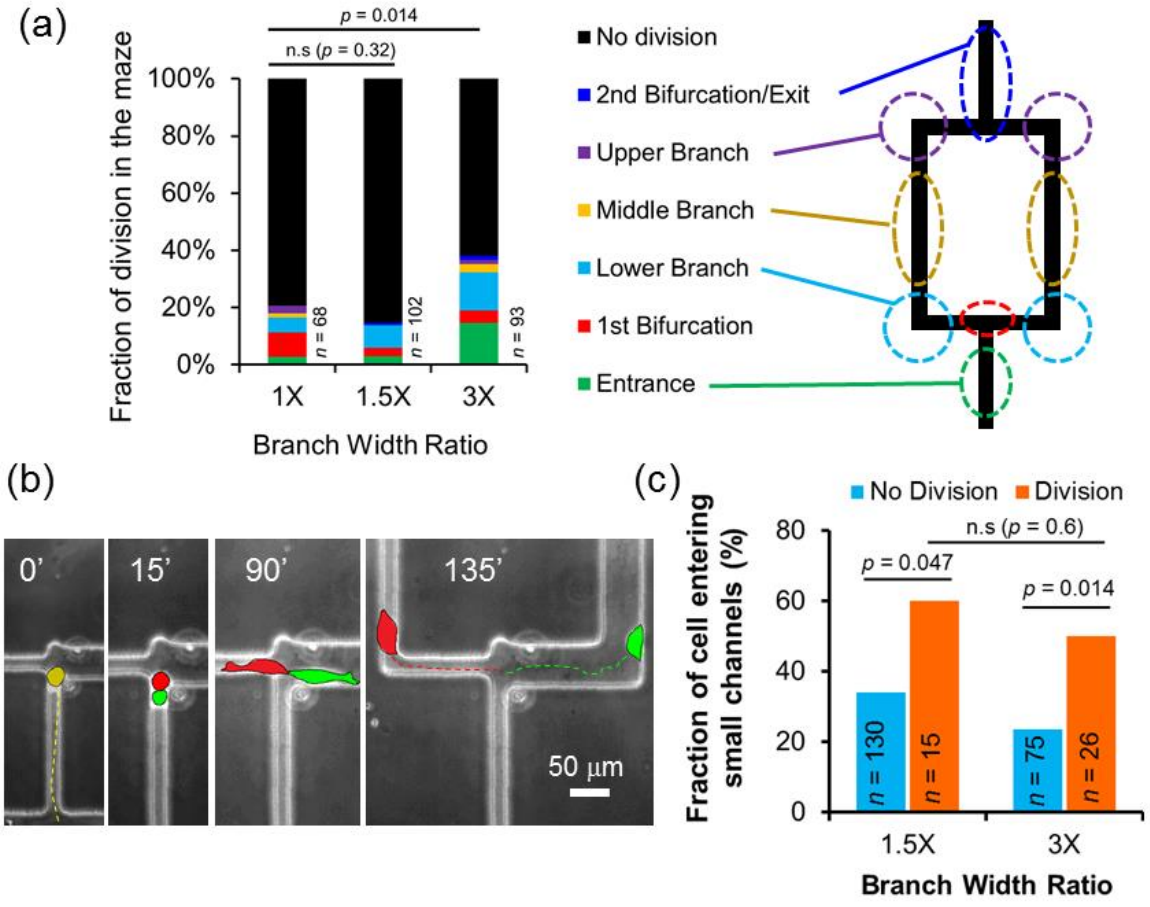

Figure 3.4 Divisions increase the chance of cells accessing the narrower branches in width-asymmetric bifurcations. (a) Spatial distribution of division occurrences within the maze. (b) Phase contrast montage showing the daughter cell migrating into the small branch after division as a function of the Branch Width Ratio. Cells are false-colored to improve visibility. Dashed lines indicate the tracked migration path (c) Bar graph showing the fraction of the cells entering the narrower branches being increased with divisions. The "No Division" fraction is based on the number of cells entering the small channel versus the total cells making decisions, while excluding all cells undergoing mitosis inside the maze. The "Division" fraction is calculated by the number of daughters entering the narrower branches versus the total cells undergoing division. The p-value between the mean of any two independent groups is found using the nonparametric Mann Whitney U test, with a statistical significance level of 0.05; 'n' indicates the number of cells; 'n.s.': not statistically significant.

3.3.4 Control Experiment Proves that Width Symmetry, not Width alone, Causes Decision Alternation

Thus far, we have demonstrated that the sequence-dependent alternation occurs less frequently when the width asymmetry in between the two bifurcation branches becomes higher. However, it is also possible that the wide size of the branch alone is responsible for the observed migration behavior. Hence, we performed a control experiment where the cells were allowed to migrate through *symmetric* bifurcation mazes with varying branch widths (see **Figure 3.5**a). Similarly to the previous sections, we quantified the directional decisions statistics of individual cells irrespective of their sequence, and also with the sequences made by any two consecutive cells being accounted for. As expected, we observed that the cells display the alternating decision pattern regardless of the branch width, even though the difference in the gradient between the left and the right branches is effectively negligible (see **Figure 3.5**b). The latter is especially true in the cases of wider branch sizes, such as the 50 and 75 μm. Specifically, the fraction of the total decisions made by all individual cells, irrespective of their sequence, show no significant differences between the cells selecting the left branch versus the right one (see **Figure 3.5**c). Furthermore, the alternating sequences (a.k.a. "opposite" path) dominated the fibroblast decision-making with a high statistical significance, regardless of the branch width (see **Figure 3.5**d). This result suggests that the branch alternation is natural to the symmetric bifurcations; and that the minute chemoattractant gradient differences are the main factors that drive the *trailing* cells toward the branches opposite of what was chosen by the ones preceding them.

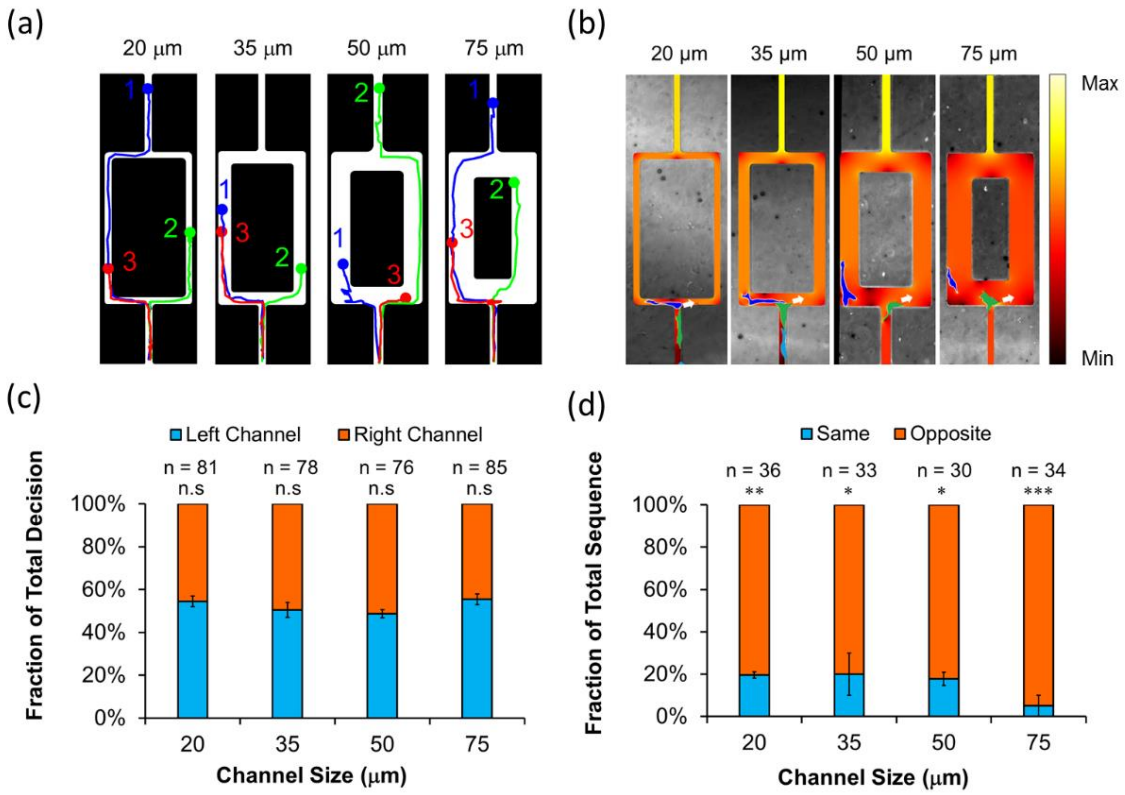

Figure 3.5. Directional decision of cells migrating inside of *symmetric* bifurcations. (a) Cell migration tracking line showing alternation patterns between consecutive cells. The lines are color-coded and numbered to indicate the order in which the cells make decisions at the first bifurcation. (b) Image-based simulation of the PDGF-BB gradient formed inside the symmetric bifurcation maze, in the presence of migrating cells. Cells are false colored to increase the visibility. Blue cells are the leading cells while the green cells are the trailing ones. White arrows indicate the direction the green cells are about to take. (c) Fraction of *all* cells moving into one branch of the bifurcation versus the other, with respect to different branch widths. 'n' is the total number of the cells making the decision. (d) Fraction of total decisional sequences made by any two *consecutive* cells. "Same" means two cells taking the same path – either left or right – while "opposite" means the trailing cell turns left when the leading cell is in the right branch, and *vice versa*. 'n' is the total number of sequence events; 'n.s.': not statistically significant ($p > 0.19$); $*$ $p < 0.001$; $**$ $p < 0.0002$; $***$ $p < 10^{-7}$.

3.3.5 Contact-Guidance is Key to Directional Decision-Making in Symmetric PDGF-BB gradient Fields

This section investigates the mechanism by which the *1st* cells to enter the bifurcation of *symmetric* branch widths decide to commit to either one branch or the other. Given that

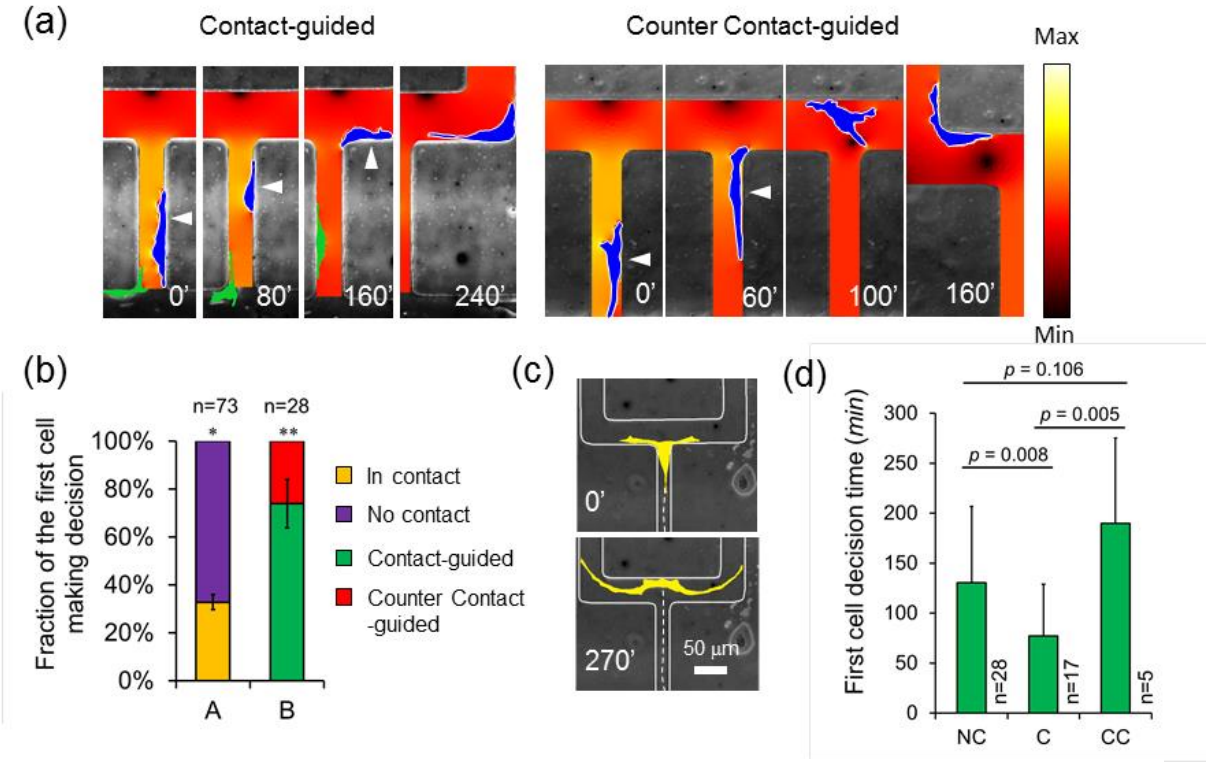

Figure 3.6 (a) Image-based simulation of PDGF-BB gradient, showing two different scenarios of the cell contacting the wall of the feeder channel, when reaching the first symmetric bifurcation. Cells can either select their path by following the wall that they are touching (i.e., contact-guided, LEFT) or go across to the opposite side of the channel (i.e., counter contact-guided, RIGHT). White arrows indicate cells being in contact. Cells are false colored to increase the visibility. (b) Fraction of 'contact' versus 'no contact', when the 1st cell travels through the first bifurcation (bar A) and fraction of cell being contact-guided (bar B). Cell touching both walls are lumped into "no contact" group; 'n' indicates the number of cells. ∗p = 0.013; **p = 0.0014. (c) Phase contrast microscopy montage showing the morphology of a cell touching both walls, thus not being contact-guided. The cells are false-colored to increase visibility. (d) Decision time of the cell at different categories. Namely, NC (no contact), C (contact-guided), and CC (counter contact-guided). The statistical significance p-value between the mean of any two independent groups is tested using the nonparametric Mann Whitney U test, with a statistical significance level of 0.05.

the chemoattractant gradient in both branches is the same, it is interesting to understand whether the cell decisions are merely random or being driven by an unknown directional cue needs to be elucidated. Interestingly, we noticed that in such *symmetrical* situations, the side of the feeder channel that the cell happens to be crawling along (a.k.a. being "in contact with") is important to the directional decision. Specifically, there are two

scenarios that can happen when the cells are in contact with a wall: either they can migrate in the branch of the same side as the wall (a.k.a. "contact-guided", **Figure 3.6**a, LEFT) or they can cross the channel to the opposite side (a.k.a. "counter contact-guided", **Figure 3.6**a, RIGHT). In both cases, the gradient in both branches of the fork is the same by the time when the decision is made.

Among the cells displaying the wall contact (as opposed to those not touching the wall, which has ~ 60% chance to occur), about ~ 80% commit to the same branch as the wall they are touching, while only ~ 20% of them move to the opposite branch (**Figure 3.6**b). Furthermore, the cells that are successfully contact-guided display a faster decision speed, when compared to the cells that choose the counter contact-direction; and to those being categorized as "no contact" (which includes the cells touching both walls simultaneously). The latter is commonly seen to display the extended body morphology shown in **Figure 3.6**c. Since such membrane protrusions are a part of the spatial gradient-sensing mechanism of the migrating cells, the symmetric body extensions shown in c indicate that the cell is still in the process of determining the branch with the most attractive PDGF-BB gradient (which appears to be highly balanced at that time). The decision time is therefore prolonged extensively and may take up to over ~130 min for the cell to make a commitment (**Figure 3.6**d). On the contrary, the decision time of the cells being *contact-guided* is significantly faster: as short as ~ 70 min; while the *counter* contact-guided cells are the slowest ones in making their decisions. The reason why this happens is likely due to the intrinsic properties of the cells rather than due to any external factors. In overall, the contact guidance is important for both the selection of direction and for the decision-making speed. Thus, it is an imperative piece of information for forecasting the cell chemotaxis in confined environments.

3.3.6 Contact-guidance is Secondary to Chemical Gradient When it Comes to Trailing Cells

Contact-guidance has been demonstrated to be effectively driving the cells' directional decisions in *symmetric* gradient conditions. However, whether it is sufficiently strong to do the same in *asymmetric* gradient situations needs to be assessed. To that end, we characterized the decision-making of the 2nd cells approaching the bifurcation (while in contact with a wall), after the 1st cells have made their choice. Essentially, the 2nd cells are *initially* either in contact with the same side as the branch selected by the leading cells, or craw along the opposite wall. In each case, they can *subsequently* either follow the leading cells, or choose the opposite branch (**Figure 3.7**a). Therefore, the 2nd cells experience more degrees of freedom (i.e., there are more variables affecting their decisions) when compared to the 1st cells.

We observed that more than 40% of the 2nd cells are *initially* in contact with the wall of the feeder channel, and over 60% of those adhere to the side of the channel opposite to that chosen by the 1st cells (**Figure 3.7**b). Interestingly, *all* of the cells that initially contacted the same side as the 1st cell selected the *opposite* channel. Similarly, over 90% of the second cells that initially contacted the *opposite* side selected the *opposite* channel, instead of trailing in the same branch as their predecessor. Such strong consistency across the results suggests that the gradient, which is higher in the opposite branch (**Figure 3.7**a, min 100), outperforms the contact-guidance in directing the trailing cells' migration.

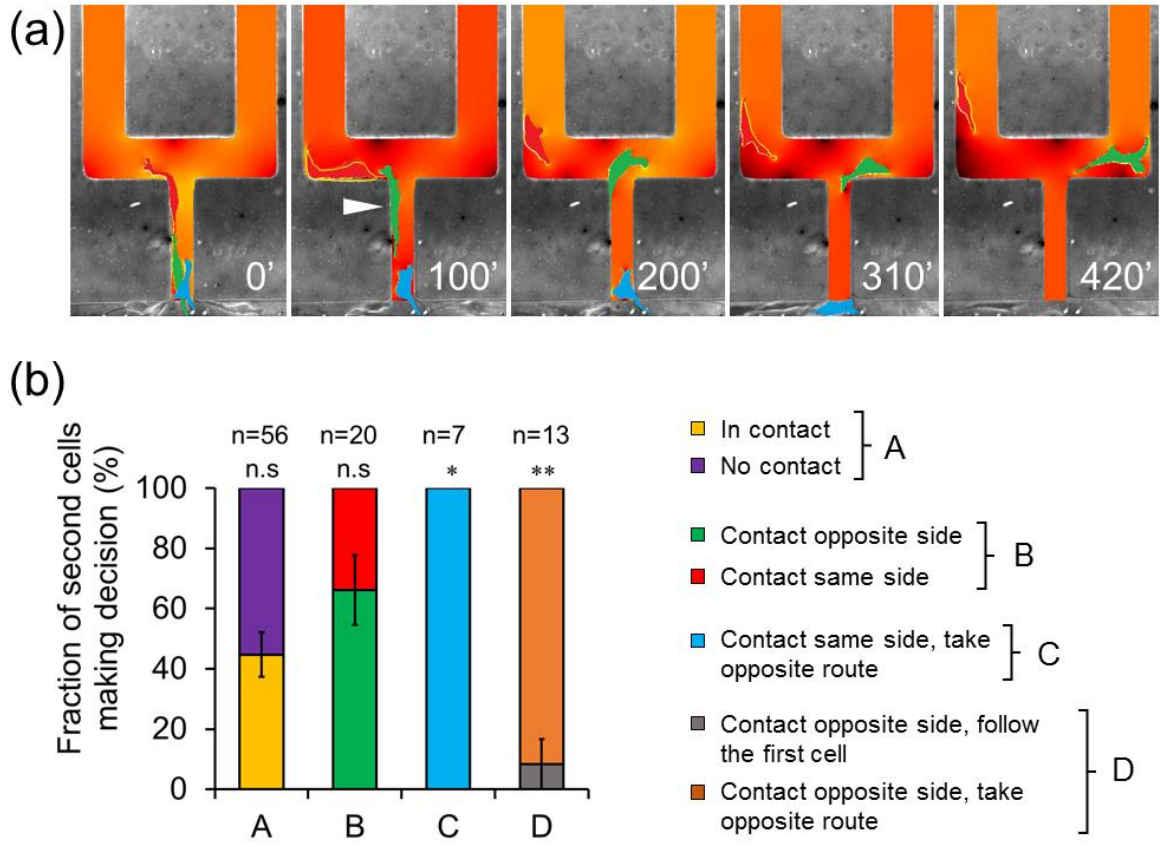

Figure 3.7 (a) Montage showing a 2nd cell taking an opposite path to the wall it contacts, due to the presence of the first cell in the adjacent branch. White arrow indicates the second cell being in contact with the wall. (b) Fraction of the 2nd cells making decision. A: Fraction of the 2nd cell contacting the feeder channel's wall; B: Fraction of the 2nd cells contacting the wall, which is on the same side as the branch chosen by the 1st cells, versus those contacting the opposite wall; C: Fraction of the 2nd cells contacting the *same* side as the 1st cells branch, but taking the *opposite* route. The case of contacting the *same* side and following the 1st cell has no statistical data to report; D: Fraction of the 2nd cell contacting the *opposite* side but following the first cell, versus *contacting* the opposite wall and taking the opposite route to the first cell. n.s: not significant ($p>0.13$); *$p = 0.008$; **$p = 0.002$.

3.4 Discussion

Understanding the cell migration in physically-confined environments is important for developing cell control and manipulation strategies for achieving artificial tissue growth both *in vivo* and *in vitro*. This is important for the fields of tissue engineering and developmental biology. Early studies have demonstrated that there are various factors

that may contribute to the migration decision of the cells inside micron-sized channels – analogous to physiological tissue pores – including channel width (22, 23, 25-27), chemical gradient steepness (23), and contact-guidance (26). However, there have not been any reports about comparison of the relative importance between these factors in guiding the cells' decision-making processes. Moreover, most of the current migration studies focus on cancer and immune cells, while little attention is paid to tissue engineering cells such as fibroblasts – that play a vital role in tissue formation such as synthesizing, remodeling, and depositing extracellular matrix materials.(9) Our study, for the first time, provides a comparison of the effects of the various directional cues on the migration of individual fibroblast cells: including the chemoattractant concentration gradient, the channel size, and the contact-guidance. We created simple bifurcated mazes with two branches of different widths, and allowed fibroblasts to travel across these geometries by introducing a gradient of PDGF-BB at the 'exit' of the device. By incorporating image-based modeling methodology (43) into our experimental approach, we have provided an insight into (i) how individual cells make directional decisions in the presence of complex migration cues and (ii) how the cell-cell interaction influences it.

Firstly, we have found that a larger width ratio between the two bifurcated branches outdoes a gradient difference in attracting the cells. This results in a large number of cells selecting the same path with a wider dimension, instead of alternating between the two branches, as is normally seen with the symmetric maze designs. However, when the difference in the gradient between two bifurcated channels becomes sufficiently significant (i.e., at the exit of the maze), the branch width ratio no longer wins over the gradient difference. As a result, the cells still opt for the narrower branch in

order to ascend a steeper gradient. This to our best knowledge, has not been demonstrated elsewhere.

Secondly, we found that when cells encounter a symmetric bifurcation (i.e., no difference between the branch widths), the gradient is predominant in deciding which path the cell will take. Typically, a higher chemoattractant gradient will attract the cells more than the lower one. This result agrees well with previous findings by Ambravaneswaran et al. (23) in neutrophils, and Scherber (22) in epithelial cancer cell studies, where the cells are observed to prefer steeper gradients. However, cancer cells and neutrophils are fast moving cells, which are fundamentally different in their sensing mechanisms when compared to the fibroblasts (19). Therefore, it is novel to know whether fibroblasts share this directional decision characteristics with the other cell types.

Furthermore, the cells were found to be guided by the way they contact the walls of the maze branches. A previous study by Paul et al. (26) have demonstrated that contact-guidance can outdo the channel size difference in guiding the breast cancer cell migration; however, whether the chemical gradients have any impacts on this behavior, and how the leading cells influence the trailing ones, are not addressed. Our study, instead, has provided an insight into these unknown questions. We found that in a *symmetrical* gradient field (i.e., inside a bifurcation of similar branch widths, and in the absence of any leading cells), the contact guidance is important for guiding the cells in making directional choices. Typically, there is an 80% confidence that the cell will select the same path as the side they contact. However, contact-guidance is less important when the gradient is asymmetric, as the fibroblasts tend to follow the higher gradient (regardless of which side they contact).

In summary, from the findings presented above, we developed a pyramid model that ranks the relative strength of different directional cues on the migration of fibroblasts (see **Figure 3.8**). The stronger the cue is, the higher its position is on the pyramid. This study has potentially widespread implications to the field of cell migration studies, as it provides an insight into the understanding of cellular behavior in a complex combination of different directional cues. It also opens a potential avenue to those who aim to control the cellular behavior (e.g., minimizing the product variability for the sake of successful biomanufacturing of artificial tissues).

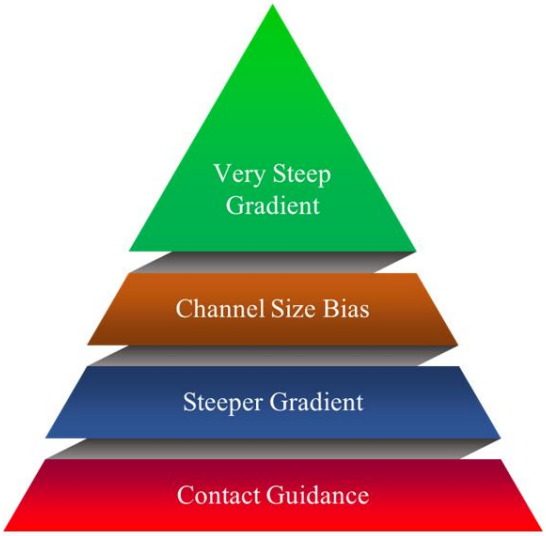

Figure 3.8 Pyramid showing the strength of decision making cue.

CHAPTER 4

OVERALL CONCLUSIONS AND FUTURE WORK

4.1 Overall Conclusions

4.1.1 Finding Summary

On the one hand, we have investigated how the cell-cell interaction and the mitosis influence the directional decision of fibroblasts during chemotaxis in microfluidic mazes of different channel lengths. On the other hand, the cooperative effects of various directional cues including channel width, gradient steepness, contact-guidance, and division on the directional decision of the cells were studied and the relative importance between them in guiding the cell directionality was demonstrated.

The experiment results on the maze with length-asymmetry revealed that cells tend to select different paths when facing a length-asymmetric bifurcation, instead of navigating the shortest route with steeper gradient. Our simulation results suggest that the leading cell consumed the chemoattractant and changed the gradient experienced by the trailing cells, thus leading to the latter to opt for an alternate route. In addition, the cellular division was found to result in daughter cells making *opposite* directional choices from each other; even it meant that one of the daughter cells had to move *against* the chemotactic gradient, and overcome oncoming traffic of other cells.

In the second experiment with the maze of various channel width, we found that a larger width ratio between the two bifurcated branches outdoes a gradient difference in attracting the cells. However, when cells encounter a symmetric bifurcation (i.e., no difference between the branch widths), the gradient is predominant in deciding which

path the cell will take. In a symmetrical gradient field (i.e., inside a bifurcation of similar branch widths, and in the absence of any leading cells), the contact guidance is important for guiding the cells in making directional choices. From the acquired results, we were able to rank these directional cues in the order from the most importance to the least: vast gradient difference between the two branches, channel width bias, mild gradient difference, and contact.

4.1.2 Implications to Tissue Engineering

The understanding of cellular behavior inside the scaffold pore is practically important to tissue engineering. Our works have demonstrated the use of microfluidic technology in understanding the directional migration of fibroblasts inside physically-confined environments, an analogy for scaffold pores. In particular, the combinatory effects of different directional cues on how cells make decision have been assessed. These include the difference in the width and the length of migration paths, the steepness of the chemoattractant gradient, and the contact surface of the migration path. Obviously, during the migration in a porous structure, migrating cells are required to make a vast number of decisions. This means they have to weigh the importance of different directional cues and follow the one that have the most significant attraction. Unlike previous studies which merely focus on isolated individual cells with no social interaction, our study provides an insight into how cell interact with each other via the consumption of chemoattractant. In addition, the comparison between different directional cues basing on their relative importance was demonstrated. Our results suggest that the directional choices of the cells inside the tissue scaffold can be controlled. For instance, we can use the chemoattractant gradient to create a uniform distribution of the cells, especially at places where the bias in directional choices exist (i.e., between a short and a long channels or between a large and a small paths). Also, we can design scaffold of different surface properties at places where the contact guidance is expected to dominate (i.e., at bifurcations of symmetric dimension and uniform gradient). Our study also demonstrated that we can optimize the cell distribution inside the scaffold by considering an optimum distribution index as a function of path length, dimension, and the proliferation rates, which is related to the growth factor concentration.

4.2 Future Work

It is obvious that when navigating the tissue pores, cells have to make countless number of directional choices. Their migration is influenced not merely by individual directional stimulations but rather by the mutual effects of various directional cues. Therefore, in order to successfully direct the cell movement, the understanding this mutuality is critical. We have provided a proof-of-concept of realizing and evaluating the cooperated influences of some factors such as channel width, lengths, gradient steepness, cell division, etc. on the cell directional decisions. However, other factors including but not limited to surface properties (i.e., stiffness) and hydraulic resistance have also been found to bias the cell directionality. Therefore, in the future, our model should account for these factors to provide more accurate understanding of realistic cell behavior.

Moreover, human tissue is a complex system which is consisted of a large variety of cell types. Our model can be developed further by accounting for the presence of different cell lineages (i.e., human dermal fibroblasts, mesenchymal stem cells, epithelial cells, neuron cells, etc.). Also, a large quantitative comparison between cues is needed to increase the accuracy of optimization calculation mentioned above.

APPENDIX A

A.1 Model Sensitivity Analysis

In order to test the robustness of the image-based model, we have performed a sensitivity analysis on the key input parameters listed in **Table 2.1**. Specifically, we tested the most uncertain biological inputs: the maximum fibroblast density $C_{f,max}$ and the rate constants k_{decay} and $k_{endocytosis}$. However, since the PDGF-BB degradation constant and the maximum Fibroblast "density" are both constants that a part of the product $-k_{endocytosis}$ $C_{f,max}$ C_P, they have the same effect on the model. Hence, we defined a new parameter called $k_{effective} = k_{endocytosis} * C_{f,max}$ for simplicity.

The effect of each parameter on the predictive capacity of the model was obtained by arbitrarily increasing or decreasing each one of them by an order of magnitude. We then measured the effect that the change had on whether the follower cells saw a steeper gradient through the shorter or the longer path, at the time when they had to make a directional decision. For illustration purposes, we display the model sensitivity analysis results (**Figure A.1**) for the same dataset and timeframe as in **Figure 2.6**C.

For the case where k_{decay} is *low*, there is almost no PDGF degradation, and the model's prediction is unaffected (since the cell sees a higher gradient in the long channel). Overall, the absence of PDGF degradation does not appear to change the model's results significantly, because it is relatively negligible to begin with. In fact, this case is most similar to the original result in **Figure 2.6**C.

For the case where k_{decay} is *high*, the PDGF in the maze degrades so fast that there is almost nothing left in either channel for the cell to follow. However, the

chemoattractant gradient is still slightly more favorable in the longer path, which makes the model's result consistent with the original prediction.

	Low	High
k_{decay}	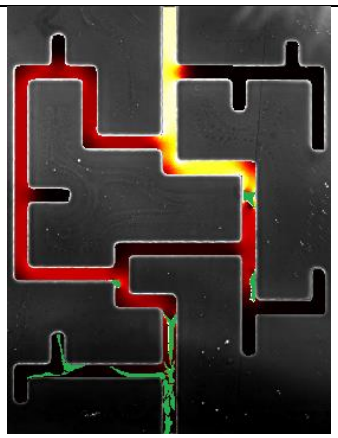	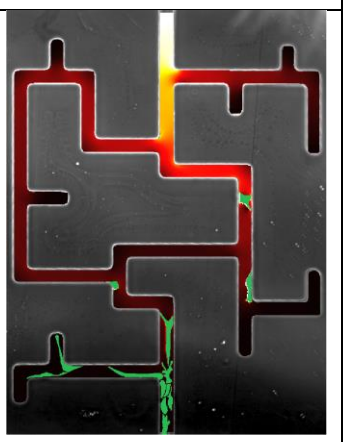
$k_{effective}$	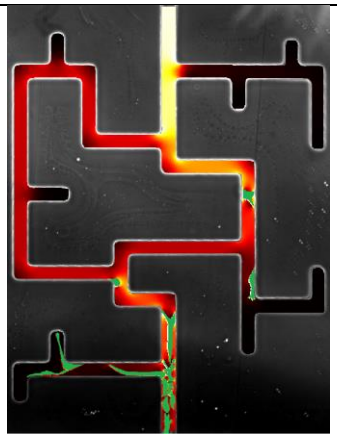	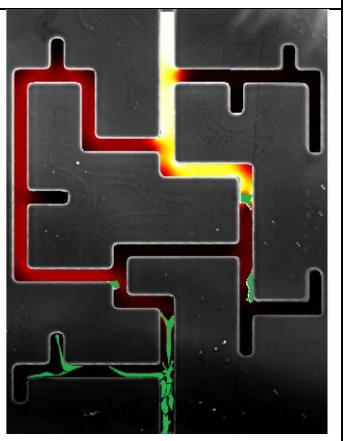

Figure A.1 Sensitivity of Model predictions, as a function of varied parameters.

For the case where $k_{effective}$ is *low*, the consumption of PDGF by the fibroblasts is *slower*. This becomes problematic, because both the short and the long path look equally favorable to the follower cell. Hence, the model has roughly a 50-50 chance (depending on the cells' locations and sizes and shapes) to make a mistake in this case.

For the case where $k_{effective}$ is *high*, the consumption of PDGF by the fibroblasts is *faster*. This leads to a greater consumption of the chemoattractant in the shorter channel

by the leading cell. Consequently, the favorability of the longer path becomes only amplified for the follower cell, and the model's prediction is again unaffected.

In summary, the model's predictive capacity is susceptible to overestimation of k_{decay} and underestimation of $k_{effective}$. Thus, extra care should be taken when it comes to estimating these two parameters. Overall, this example is representative of predicting the other cells' decisions as well.

A.2 Effects of Diffusion Limitations on the PDGF Uptake Rate by the Cells

In order to estimate the PDGF uptake rate per cell yielded by the model, we assume that it occurs as a pseudo-first order reaction in a *porous catalyst*. First, we need to determine whether the reaction is diffusion-limited or not. This is done by calculating the Thiele modulus, $\emptyset$. The first order rate constant is the same as before, $k_{effective} = k_{endocytosis} * C_{f,max}$ = 0.1 x 0.555 = 0.0555/sec. With an assumed intracellular diffusivity of $D_{P,cell} = 10^{-12}$ m^2/s, and an order of magnitude estimate of the characteristic half-length L ~ 30 microns, the Thiele modulus becomes equal to: $\emptyset = L\sqrt{\frac{k_{effective}}{D}} = 7$. Thus, the reaction is in fact in the diffusion-controlled regime, given that the physical meaning of $\emptyset$ is diffusion time / reaction time. Therefore, we have to use the 'effectiveness factor' in order to gauge the effect that diffusion has on slowing down the PDGF uptake reaction happening in the cell.

The effectiveness factor is calculated as: $\eta_p = \frac{tanh(\emptyset)}{\emptyset} \approx \frac{1}{7}$. Given that its physical meaning is $\eta_p = \frac{r_{observed}}{r_{max}}$ (where $r_{observed}$ is the reaction rate with pore diffusion resistance, and r_{max} is the reaction rate at surface conditions), this result tells us that the PDGF uptake reaction is slowed down by diffusion limitations within the cell by a factor

of 7. To estimate the actual uptake rate, we need to first calculate the PDGF uptake rate at the ideal (without diffusion limitations) conditions, r_{max},

To r_{max}, we take the product of a modest PDGF concentration of 0.1 nM; an approximate cellular volume of $4x10^{-12}$ L; Avogadro's number $6x10^{14}$ molecules/nmol; the assumed effective rate constant $k_{effective}$ = 0.0555/s; and the conversion of 60 s/min. This yields a value for $r_{max} = 8 \times 10^2$ molecules/ minute/cell. Finally, we multiply this value by the effectiveness factor, in order to get the diffusion-limited uptake rate, $r_{observed}$. Thus, for this sub-saturating ligand concentration it is estimated that an order of magnitude for the uptake rate per cell in our model is $r_{observed} \sim 10^2$ molecules/minute/cell. This a reasonable value, given that the upper limit on the uptake rate *via* receptor-mediated endocytosis is $\sim 10^4$ molecules/minute/cell.

APPENDIX B

A COMPACT LOW-COST LOW-MAINTENANCE OPEN ARCHITECTURE MASK ALIGNER FOR FABRICATION OF MULTILAYER MICROFLUIDICS DEVICES

B.1. Abstract

A custom-built mask aligner (CBMA), which fundamentally covers all the key features of a commercial mask aligner, while being low cost, light weight, and having low power consumption and high accuracy is constructed. The CBMA is comprised of a custom high fidelity LED light source, vacuum chuck and mask holder, high-precision translation and rotation stages, and high resolution digital microscopes. The total cost of the system is under $7,500, which is over ten times cheaper than a comparable commercial system. It produces a collimated ultraviolet illumination of 1.8-2.0 mW cm^{-2} over an area of a standard 4-inch wafer, at the plane of the photoresist exposure; and the alignment accuracy is characterized to be < 3 μm, which is sufficient for most microfluidic applications. Moreover, this manuscript provides detailed descriptions of the procedures needed to fabricate multilayered master molds using our CBMA. Finally, the capabilities of the CBMA are demonstrated by fabricating two and three-layer masters for micro-scale devices, commonly encountered in biomicrofluidics applications. The former is a flow-free chemical gradient generator and the latter is an addressable microfluidic stencil. Scanning electron microscopy is used to confirm that the master molds contain the intended features of different heights.

B.2 Introduction

Multilayer photolithography has played a central role in the microfabrication of multi-height photoresist master molds for polydimethylsiloxane (PDMS) microfluidic devices, which is widely used in various fields of biological, micro electro-mechanical systems (MEMs), micro total analysis systems (μTAS), sensors and other applications.(22, 84-88) Moreover, with the current explosion of the lab-on-a-chip technology in diagnosis and fundamental medical research, the need for the miniaturization of systems *via* deposition and etching procedures is greater than ever before.(89-91) Nevertheless, the high cost of the equipment and its maintenance, combined with the expensive and space-consuming installation requirements associated with commercial systems, limit the access of many small laboratories and companies to manufacturing microfluidics devices in-house. For example, at the center of the photolithography fabrications is a mask aligner, which simultaneously provides precise mask-to-wafer alignment and generates a uniform ultra violet (UV) illumination over an exposed photoresist surface. On the other hand, current commercial systems (i.e. Karl Suss, OAI, Kloe and EVG) are very costly (e.g., $60,000-100,000 capital investment, plus $1,000-3,000 annual maintenance), heavy (> 250 lbs.), and relatively bulky (> 700 in^2). Therefore, there is an unmet need for photolithography systems that are fully functional, yet compact and affordable. To that end, this manuscript aims to present a custom-built mask aligner (CBMA), that can be constructed easily and for as little as $7,500 (and potentially even lower, if an in-house machine shop is used).

A collimated UV light source is the key component of any mask aligner, as it is directly responsible for creating the master molds for the microfluidics devices by crosslinking photoresist coated on wafers in a masked pattern. Typically, a high-pressure mercury lamp is used for this purpose by commercial systems. However, the UV light alone

requires a significant capital investment (~$10,000-20,000), and accounts for a dominant portion of a mask aligner's annual maintenance costs. Moreover, the mercury lamps tend to provide a broadband illumination (bad for fabricating tall features) with an intensity that often drifts with time. Consequently, several efforts have been made to produce low-cost alternatives to the mercury lamp. For example, Huntingtan et al. (92) introduced a portable light source composed of an array of hundreds of light emitting diodes (LEDs), which could be powered by AA batteries. Though such sources can provide a relatively uniform illumination that yields sub-micron features, they are not suitable for thick photoresist masters (i.e., over 100 μm) due to the large divergence of the illumination. Yet, many microfluidics applications require features this high. As a result, a more recent light source addressed this problem by improving the light collimation using optical lenses that help to reduce the divergence of the light beam.(93) As a result, it was able to pattern thick masters of up to several hundred microns, while using an array of just nine high power 365nm LEDs. Thus, we chose this light source for our CBMA for its superior quality and minimalistic design.

In addition to the light source, a complete mask aligner system should have the capability for a mask-to-wafer alignment, which is critical for multi-layer soft lithography. Alignment systems have been made by other researchers. For example, Li et al. (94) introduced a desktop aligner that combines digital microscopes with high-precision translation stages for aligning polydimethylsiloxane (PDMS) slabs. However, photolithography is not the main purpose of this system, and thus it is not equipped with a UV light source for photoresist exposure. Hence, there is a need for an alignment system with an integrated high fidelity light source, capable of deep (i.e., > 100 μm) photoresist exposure.

Table B. 1 Key Feature Comparison Between The CBMA and A Typical Commercial Mask Aligner

Features	Custom-built	Commercial
Cost/Price, *$*	< 7,500	60,000 - 120,000
Weight, *lbs*	< 50	> 250
Light source power, *W*	~ 22	> 1000
Width x Depth, in^2	15 x 10	32x23
XY Alignment Accuracy, μm	2.96	< 0.5

To that end, we designed a low cost alternative to current commercial systems that is well equipped with the fundamental functions of a complete mask aligner: a uniform UV light with deep photoresist penetration, high-resolution rotation and translation stages, vacuum chucks and mask holder, and digital microscopes for high-precision alignment, etc. Along with the instructions for how to build the system, this manuscript also provides the detailed procedures for how to optimize its performance and manufacture multi-layer master molds with a high accuracy. Given that this system is affordable and low maintenance, it is expected that it will have widespread applications, especially in small and medium laboratories that do not have access to an in-house microfabrication facility.

B.3. Key Features and System Description

Key features of our CBMA include cost-savings, light weight, space savings, and an alignment accuracy sufficient for most typical microfluidics applications. A comparison of some of these the key features between the CBMA and a typical commercial system is given in Table B.1. Relative to a professional system (i.e., Karl Suss MA100, EVG 620, OAI 200), our system is an order of magnitude cheaper, weighs ~5 times less, occupies ~5 times less space, and consumes ~50 times less power. Moreover, it has an open adjustable architecture and a negligible annual maintenance cost. Finally, although the

resolution of CBMA is not as high as that of a commercial system, it is still sufficient for most MEMS and microfluidics applications.

A detailed cost breakdown of all the main components of the CBMA is provided in Table B.2. The major cost comes from the use of translation and rotation stages, which provide the high precision, stable, and smooth motion of the mask, wafer, and microscopes, thus allowing for a fine and accurate alignment. Other components include a collimated UV light source, custom-machined wafer chuck and mask holder, digital microscopes, and other minor mechanical and electronic components. All of these components are discussed in detail in the subsequent sections of this manuscript. The entire unit can be mounted on an optical breadboard with imperial threaded holes in order to dampen vibrations.

Table B.2 Cost Breakdown Showing The Approximate Costs of The Main Components of Our CBMA

Item	Part Numbers (quantity)	Company	Cost, $
Translation & rotation stages	423-MIC (3), 461-XZ-M(1) 360-90 (2), UTR80 (1), 39 (1)	Newport, Irvine, CA	4,100
Machined adapters	-	Zera Development, S. Clara, CA	1,000
Digital microscopes	AD4113T (2)	Dino-lite, Torrance, CA	900
UV LED	UV LED 897-LZ110U600 (9)	Mouser, Mansfield, TX	390
Machined wafer chuck	-	Emachineshop, Mahwah, NJ	300
Dovetail optical Rail & carrier	10R300 (2), 20C (2)	Optic Focus Solution, China	280
UV-collecting lens	FCN12592_LE1-D-COP (9)	Mouser, Mansfield, TX	140
0-50 V power supply	29612 PS (1)	MPJA, West Palm Beach, FL	100
Laser cut & engraving	Mask holder (1), Lens mount (1)	Ponoko, Oakland, CA	100
Analog relay timer	H3CR-A8-AC100-240 (1)	Mouser, Mansfield, TX	70
T-slotted aluminum frame	1010 (160 in)	Knotts Co, Berkeley Heights, NJ	40
Total			7,420

B.3.1 Light Source

The LED-based light source for the CBMA is reproduced from a system published by Erickstad et al.(93) This system was selected because it offers several advantages such as excellent illumination uniformity, low cost, short response time, and stable and low power consumption. Hence, the LED light source is significantly cheaper and more energy efficient when compared to a standard UV mercury lamp, which requires significant capital investment and annual maintenance, costs.

The complete technical details of the LED light source have been discussed elsewhere.(93) For the sake of brevity, we describe some its main components, and the modifications we made to the original design. Typically, the light source consists of a 3x3 square array of nine LEDs mounted on an aluminum plate, 50 mm apart from each other. The LEDs were soldered to 26G electric wires using low temperature solder cores (Indium Corporation, Clinton, NY). A UV-collecting lens was glued to each LED to reduce the divergence angle of the emitted light from 80° to 12°. The divergence angle was further brought down to ~4.7° using a squared array of credit card-sized plastic Fresnel lenses (with the same pitch as the LEDs). Light passing through the lens array is projected down to create an overlapping area of uniform illumination at the wafer plane. The plane is located 906 mm away from the aluminum plate that serves as a base for the LEDs.

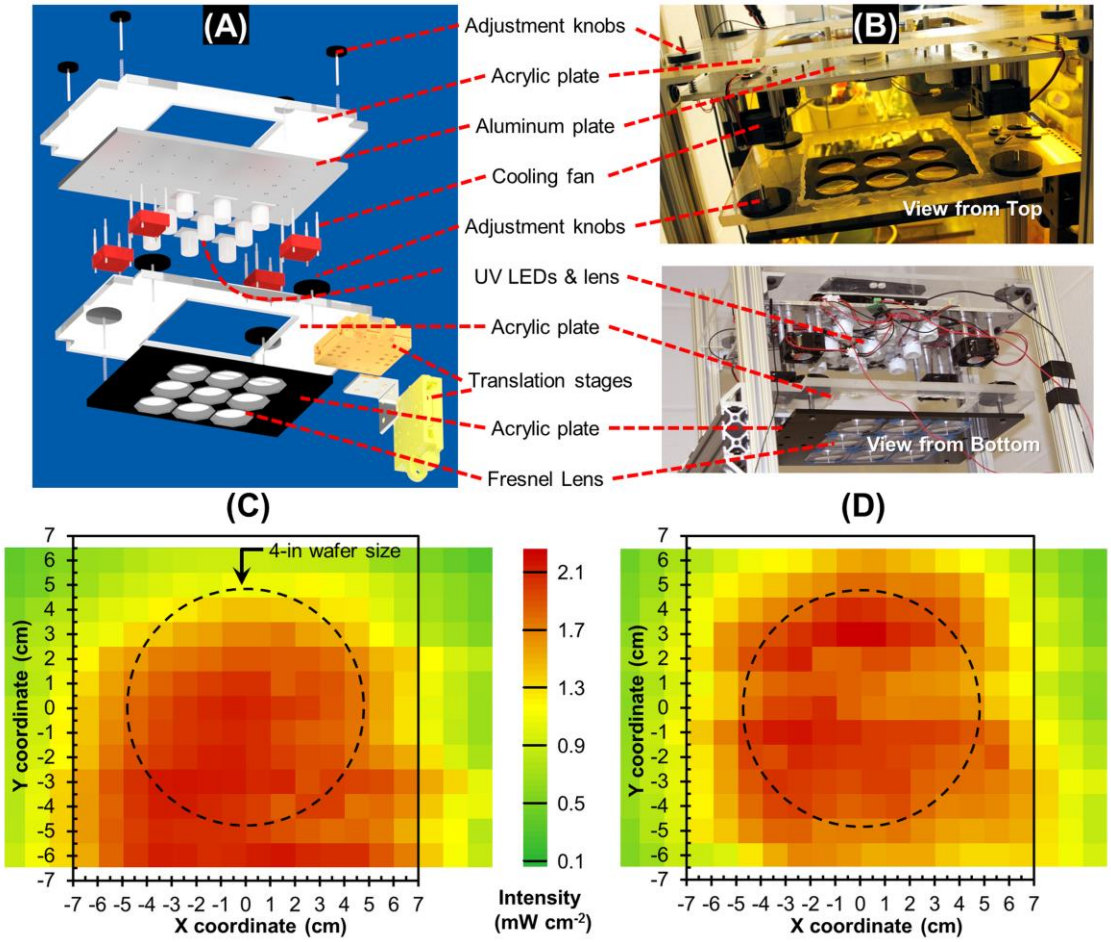

Figure B. 1 (A) An "exploded" view of the custom UV light source constructed from a squared array of nine LEDs. Compared to original design,11 the tip/tilt adjustment is added in order to further to aid the accurate alignment of the light source components. (B) Photograph of the light source assembly viewed from the top and from the bottom of the mask aligner. (C) & (D) Heat maps showing the distribution of light intensity before and after LED alignment, respectively. The dashed circles represent the location of a 4-in Si wafer, which is aligned co-centrically with the LED array.

In the original design, the light source was fixed to a ceiling of a room. This does not provide flexibility to the system, especially when it needs to be moved around the lab space. Instead, we mounted the light source on a supporting frame made from T-slotted aluminum 80/20 extrusions (Knotts Co, Berkeley Heights, NJ). This way, the frame and the light source can be moved together easily. We further modified the system by introducing a tip/tilt translation to the light source using an acrylic plate with adjustment

knobs (Figure B.1A, B). This adjustment ensures the perpendicularity of the light beam. The tip/tilt translation and a linear translation were also added to the Fresnel lens plate to make sure the lenses were co-aligned with the light source. Five cooling fans were provided to dissipate heat generated from long-exposure LEDs. However, they were usually turned off to avoid vibration when working with patterns of small feature sizes, since they require a short exposure time. It was found that doing this would not significantly affect the performance of the CBMA.

The adjustment of the illumination is demonstrated in Figure B.1C, D. Here, it can be seen that without the adjustment, the illumination was not well centered, and is thus unable to provide a uniform photoresist exposure over a wafer surface (Figure B. **1**C). However, by tuning the tip/tilt adjustment knobs as well as the translation stage, we were able to center the light, thus providing a more uniform illumination over the wafer area (Figure B.1D). In order to generate Figure B.1C and D, the spatial distribution of the light intensity at the theoretical wafer plane (i.e., ~906 mm from the light source) was measured using a Traceable UV meter (#06-662-65, Fisher, Waltham, MA) at 1-cm increment in the X and Y directions. The light source was supplied with 34-V, 0.6-A power, and the heat maps were generated using the "Color Scales" function of Microsoft Excel (Microsoft, Belleville, WA).

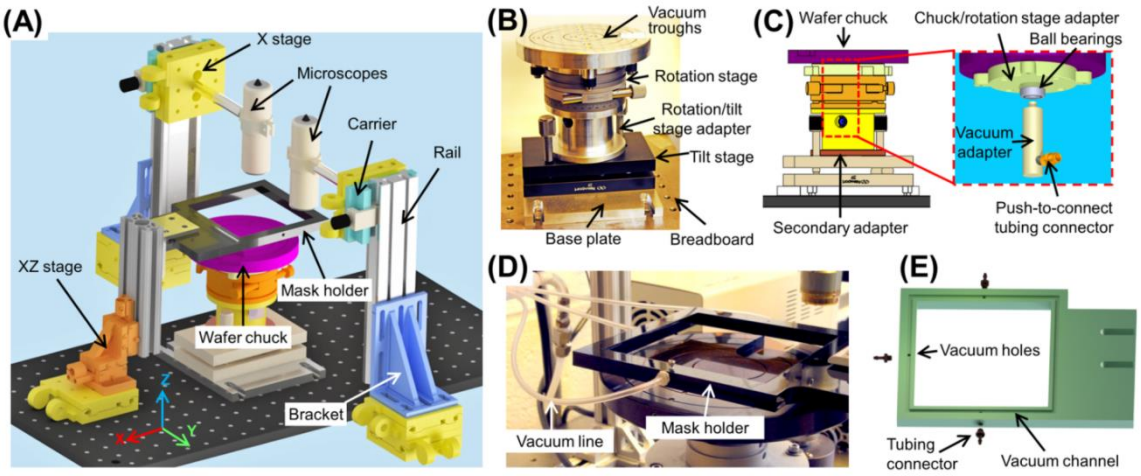

Figure B. 2 (A) A 3D illustration view showing the design of the alignment assembly comprised of a wafer chuck, mask holder, microscopes, and high-precision positioning stages. (B) A photograph of a wafer-mounting assembly showing the wafer chuck placed on top of a rotational and tip/tilt translational station. (C) An illustration showing different parts of vacuum adapters that help to connect the wafer chuck to the house vacuum. (D) A photograph showing an acrylic mask holder connected to the house vacuum *via* tubing. (E) A 3D view of the mask holder showing a vacuum channel engraved on the holder's surface, and ports supplying vacuum to the channel.

B.3.2 Vacuum Wafer Chuck and Mask Holder

In order to securely fasten the wafer and the photomask during alignment and exposure, an aluminum chuck (machined by Emachineshop, Mahwah, NJ) and an acrylic holder (laser cut and engraved by Ponoko, Oakland, CA) were designed (Figure B.2). Both the wafer chuck and the mask holder operate *via* vacuum. The wafer chuck was patterned with 0.8-mm wide, 1-mm deep concentric troughs, which help to hold the wafer tightly and minimize any vibration due to rotation (Figure B.2B). The chuck is compatible with a wafer size of 4 in or smaller. The vacuum was supplied to the innermost trough through 4 vacuum holes, which were connected to a 15-Torr house vacuum *via* a bearing adapter (machined by Zera Development Co, Santa Clara, CA) attached to the bottom of the chuck (Figure B.2D). This setup allows the chuck to be rotated freely in 360°, thus offering a high-flexibility alignment. The holder for the photomask was laser-cut from a 10-mm thick acrylic plate in order to create a window with 4 in square aperture for the

UV light. Additionally, it was engraved with a 1-mm deep, 3.25-mm wide vacuum channel for holding the mask. The holder was also connected to the house vacuum *via* tubing, as shown in Figure B.2C. Once the vacuum was activated, the chuck could firmly hold a 5-inch square 90 mil-thick quartz mask (Photomaskportal, Richardson, TX). Both the wafer chuck and the mask holder were levelled using a bull‘s eye level to ensure that the mask and the wafer were in full contact. The 3D drawings for the wafer chuck and mask holder assemblies can be found in the supplemental materials.

B.3.3 Alignment Microscopes

The registration of multiple masked patterns on a wafer requires placement of “alignment” marks on the masks and “reference” marks on the wafer. This process relies heavily on the visibility of the micron-size marks, often located diametrically opposite to each other on the wafer / mask. Herein, we used two digital microscopes (AD4113T, Dino-lite Digital Microscope, Taiwan) positioned on both sides of the CBMA to provide microscopic views of the marks (Figure B.2A). These microscopes were used since they are cheap, compact, and simple to operate. Moreover, they can be connected to a laptop *via* a Universal Serial Bus (USB) interface, and controlled using the Dino Capture 2.0 software provided by the manufacturer. During alignment, both microscopes were used simultaneously to acquire a live view of the marks at various magnifications (Figure B.3). The UV content of the microscopes’ light sources is negligible, as measured by a UV meter; however, to ensure the photoresist was completely intact during alignment, the microscopes were covered with amber UV filter films (#F007-006, UVPS, Chicago, IL), which absorbed any UV radiation emanated from the microscopes’ light sources.

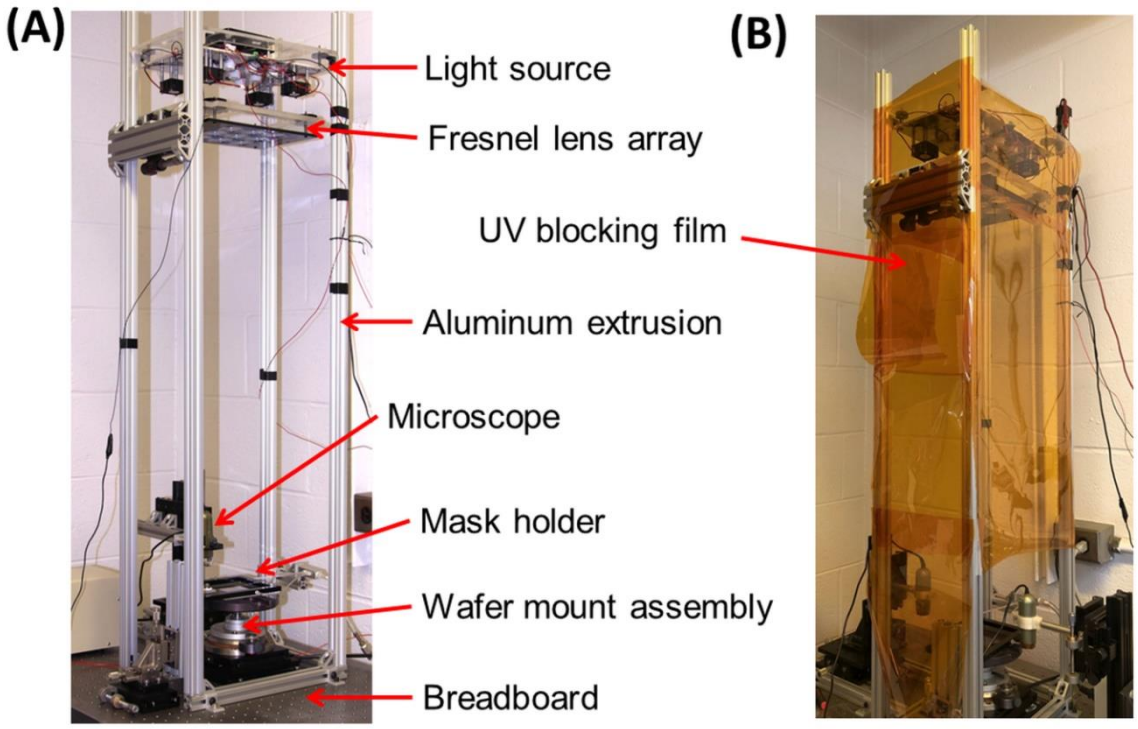

Figure B.3 (A) Photograph of the CBMA showing all of its major components: the light source, the microscope, the mask holder, and the wafer-chuck assembly. The light source and the Fresnel lens array are mounted on a supporting frame assembled from T-slotted 8020 aluminum extrusions. (B) Photograph showing the CBMA covered with UV-resistant plastic film, which protect the user from being exposed to the UV during operation.

B.3.4 Kinematic Mask Alignment System

In order to ensure of a robust mask-to-wafer alignment with a high fidelity, high-precision positioning stages were used. The wafer chuck was mounted on a rotary stage (#UTR80, Newport) and a tip/tilt stage (#39, Newport), which offer high sensitivities of 0.001° and 0.002°, respectively (see Figure B.2B). The mask holder was mounted on a translation complex, which consisted of a XZ translation stage (#461-XZ-M, Newport) and a Y translation stage (#423, Newport) combined. This allows the mask to travel in all three directions, with travel distances of 1 inch in X and Z, and 2 inches in Y (see Figure B.2A). Digital microscopes were also mounted on linear translation stages (#423-MIC,

Newport, Irvine, CA) configured in XYZ directions, thus allowing the microscopes to be accurately positioned and focused in a highly repetitive manner. Fast and coarse vertical motion of the microscopes was facilitated using tail optical rail and carrier (10R300 and 20C, respectively; Optics Focus Instruments Co, China).

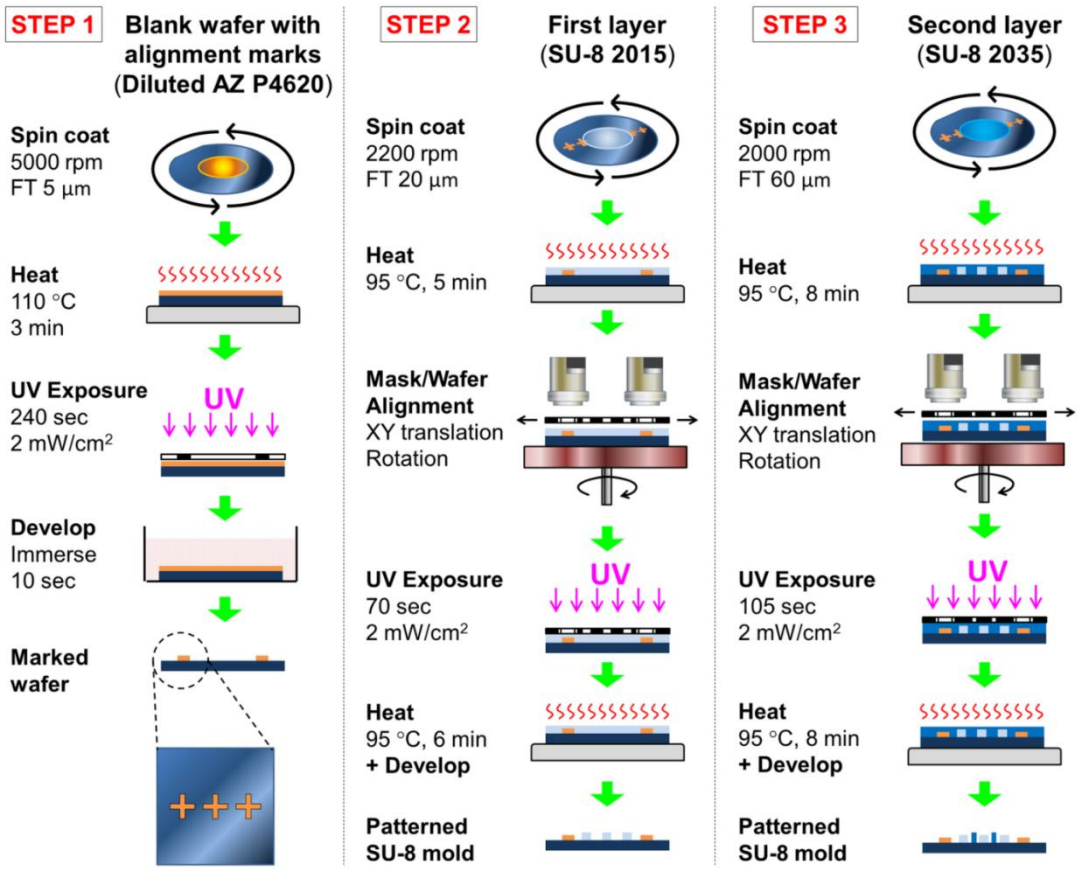

Figure B.4 Fabrication of a multi-height master mold on a 4-in Si wafer using the CBMA in a 3-step procedure. In step 1, reference marks are imprinted on the wafer using a diluted positive photoresist (#AZ P4620, Microchem) via a "reference" mask. In step 2, a 20-µm high SU-8 photoresist layer is patterned on the wafer, which is aligned with the mask using the CBMA. In step 3, a 60-µm thick SU-8 layer is patterned on the same wafer following a similar procedure mentioned in step 2, but with a different mask. Abbreviations: FT = Film Thickness.

B.3.5 Electronics

A bench-top variable 0-50 V power supply (#29612 PS, MPJA, West Palm Beach, FL) was used to power the light source using a voltage setting of 34 V and a current of 0.6 A. This provides an average illumination power of ~1.85-2.00 mW/cm2 at the wafer's surface (see Figure B.1 C, D). The exposure time was controlled by a mechanical relay timer from Omron (#H3CR-A8-AC100-240, Mouser, Mansfield, TX) which automatically disconnects the light source from the power supply when the set time is reached. The cooling fans (#SY124020L, Scythe Co., Germany) were powered by a 12V AC power supply (#1670, Current USA, Vista, CA).

B.3.6 Supporting Frame

The frame of the CBMA was constructed from T-slotted 8020 aluminum extrusions (Knotts Co, Berkeley Heights, NJ) which offers stable mounting of the hardware components, and at the same time provides for the light-weight nature of the CBMA (Figure B.3A). The light source was attached directly to the frame, while the wafer chuck, the mask holder, and the microscopes were not connected to it. To ensure the safety of the user, the frame is covered with a UV blocking film (#F007-010, UV Process Supply Inc.) (Figure B.3B). This frame can be conveniently mounted on top of an optical table with imperial threaded holes. Alternatively, it can also be used as a standalone setup, without the optical table. However, one is recommended in order to reduce fabrication defects caused by vibration. This setup offers the flexibility often desired in laboratories with a limited space.

B.4 Fabrication Procedure

The fabrication of a master mold of a microfluidic device (shown in Figure B.7 and discussed in detail in the "Mask Aligner Application" section) with two different heights is used to illustrate a typical alignment procedure for the CBMA. Generally, this type of fabrication follows a standard photolithography technique, which includes three basic elements: spin coating, UV exposure, and development. In order to generate a master mold with two different heights, we used three photomasks: a "reference" mask

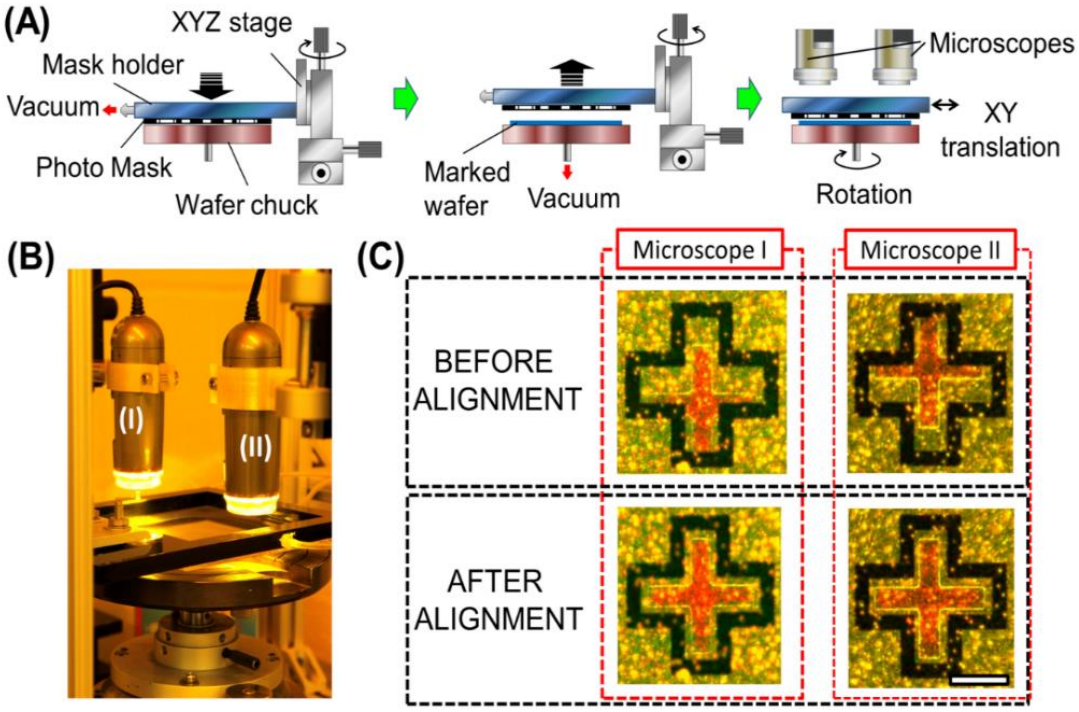

Figure B. 5 (A) Diagram showing a step-wise alignment procedure using the CBMA. (B) Two alignment microscopes in operation. (C) Visualization of the fine alignment process captured by the alignment microscopes at 245x. Black hollow and red solid crosses are the mask "alignment" and the wafer "reference" marks, respectively. Scale bar is 200 µm.

containing only reference marks to be imprinted on the wafer, and two "device" masks containing templates for the different photoresist heights. These masks can be either chrome coated on a glass substrate or printed on transparencies at a high resolution (>

10,000 dots per inch). Even though the transparency masks are not likely to offer feature sizes smaller than 10 µm, they are inexpensive and suitable for most standard microfluidic applications. Therefore, we went with this option.

The transparency masks were taped onto 5-in square bare quartz substrates (90-mil thickness) (Photomaskportal, TX) with the printed side facing outward, using a ¼-in polyimide film tape (#5413, 3M, Mapplewood, MN). A 3-step procedure for the fabrication of a multi-height master is outlined in Figure B.4. In the first step of this procedure, the two reference mark arrays were fabricated diametrically opposite to each other on a 4-in Si wafer (#1196, University wafer, South Boston, MA), using the "reference" mask. The marks were 70-80 mm apart from each other. Positive photoresist (# AZ P4620, Microchem, Westborough, MA) was diluted prior to spin-coating with an edge bead removal solvent (#EBR PG, MicroChem). A resist:EBR ratio of 1:4 was used to achieve a thin layer of 5 µm. This photoresist was selected due to its amber shade when developed, which provides alignment marks that are highly contrasted relative to the color of the wafer. The alignment accuracy is significantly enhanced as a result.

In the second step of the procedure in Figure B.4, the 20 µm-high feature of the master mold was generated from a negative photoresist SU-8 2015 (Microchem). The negative photoresist was spin-coated on the "marked" wafer generated in step 1. After the coating, the first layer "device" mask is aligned with the wafer's reference masks using the alignment procedure discussed in the subsequent "Mask Alignment Procedure" section of this manuscript. After alignment, the wafer was exposed to UV (140 mJ), and developed to create a 20-µm high resist pattern. The third step of the procedure in Figure B.4 is needed in order to generate the 60-µm high feature of the master mold. It essentially repeats the second step, but with a different "device" mask. Photoresist SU-8

2035 (Microchem) was again spin-coated on the same wafer to achieve a 60-μm thick film. This was then followed by alignment of the second layer "device" mask using the CBMA. The resist was then exposed to UV (210 mJ) and developed to attain the final master mold.

B.5 Mask Alignment Procedure

A detailed aligning procedure is illustrated in Figure B.5A. First, a "device" photomask is placed on top of a vacuum wafer chuck with the pattern side facing downward. The mask holder is lowered in the Z direction by a XYZ translation stage, until it is in contact with the mask. Then vacuum is applied in order to seal the mask to the mask holder. Once the mask is securely attached to the holder, the assembly is raised up in order to vacuum-seal a marked wafer (described in Step 1 of Figure B.4) on to the wafer chuck. The mask is then brought in close proximity to the wafer (i.e., less than 100 μm, assuming the resist film thickness is smaller than that). Note that the distance between the mask and the wafer can be judged by observing the reflection of the mask on the wafer surface. Excessively close proximity is not necessary, as it would restrict the movement of the mask and the wafer during alignment.

The coarse alignment begins by focusing two digital microscopes on the two alignment mark regions on the "device" masks, as shown in Figure B.5B. The reference marks on the wafer are brought into the microscopes' views using the translation and rotation stages. This is first done at a 30x magnification of the two microscopes in order to achieve coarse alignment (Figure B.6A). Fine alignment then follows at a 245x magnification (Figure B.6B). At this time, the marks viewed by Microscope I should be symmetrically opposite to those viewed by Microscope II with respect to the center of the wafer. This helps to minimize the rotational error of the alignment. In addition, it should

also be noted that at the 245x magnification, the Dino-Lite microscopes have a working distance of ~ 10 mm. This allows both the wafer's reference marks and the mask's alignment marks to stay in focus at the same time (Figure B.5C), which also greatly enhances the alignment accuracy.

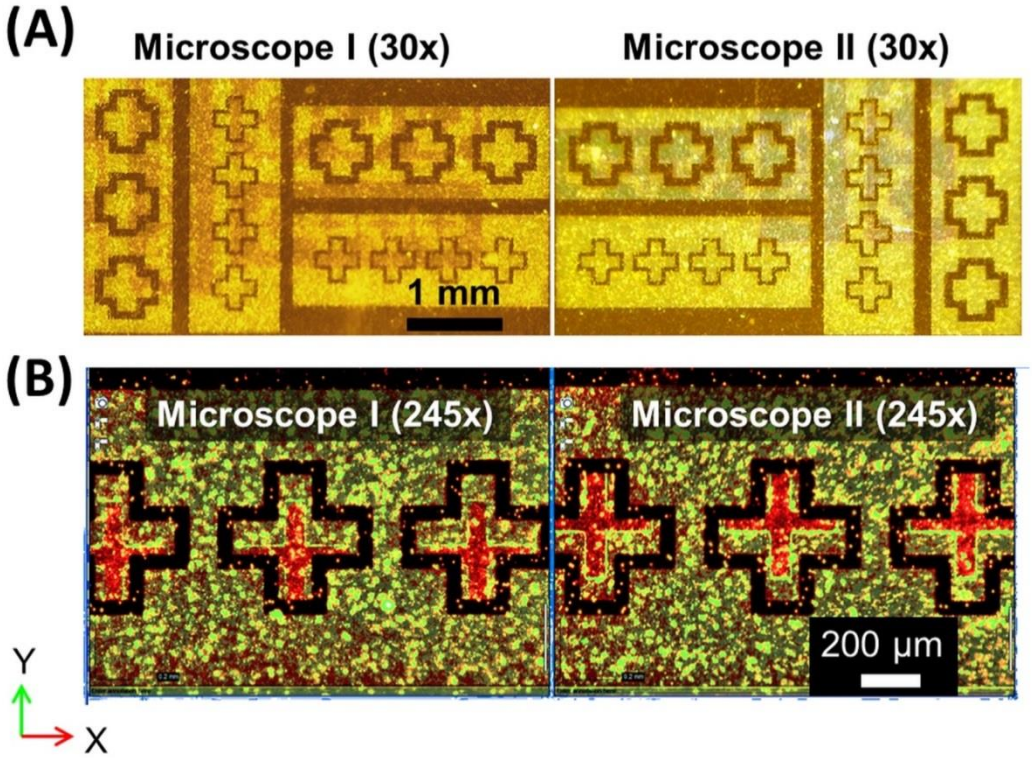

Figure B.6 Screenshots from two monitors, showing the live-view microscopy acquisition windows corresponding to the two alignment microscopes. Alignment and reference marks are positioned at the same Y location on each respective screen. (A) Two alignment/reference mark arrays being focused upon at a 30x magnification. (B) Individual alignment/reference marks being focused upon at a 245x magnification. Alignment marks (black color) of the on the left side and on the right side of the "device" mask were brought into same Y positions on each of the view screens.

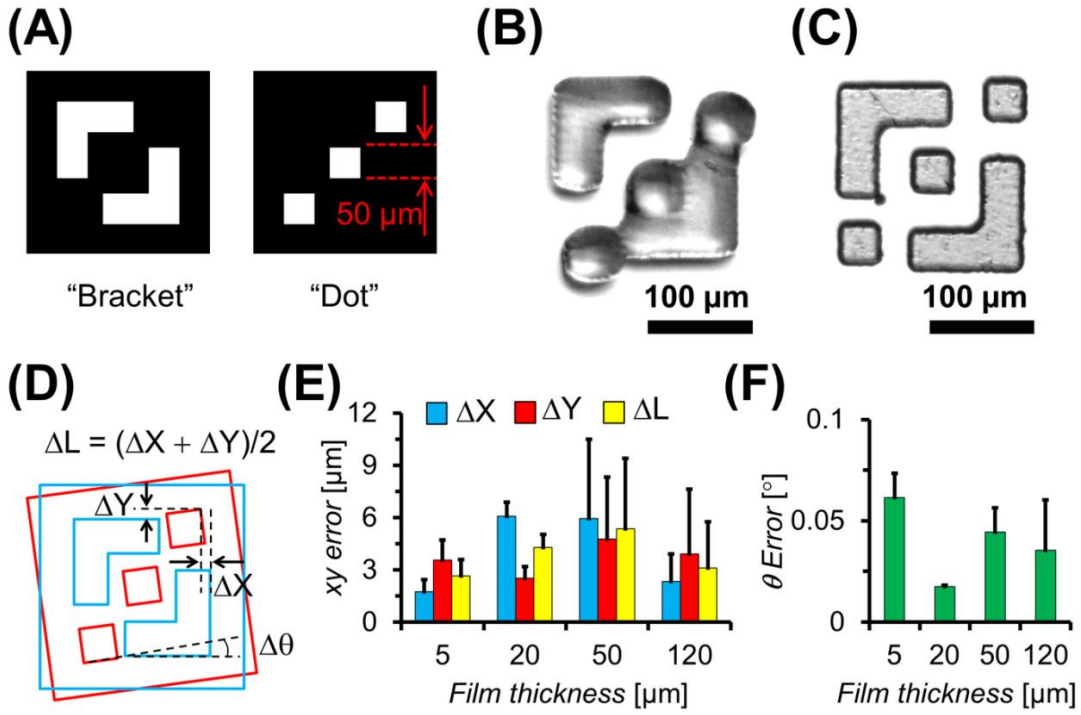

Figure B.7 (A) Two photomasks containing different alignment patterns, "bracket" and "dot", were used to generate a photoresist profile for the alignment accuracy measurement. (B) Micrograph of a defective SU-8 print caused by misalignment of the two patterns. (C) Micrograph of a SU-print obtained from well-aligned patterns. (D) Illustration of how translational X-Y and rotational θ error values are determined. (E) & (F) CBMA alignment errors quantitatively determined from the SU-8 prints with respect to the photoresist's thickness.

The fine adjustment is first started by bringing the two masks' alignment marks to the same Y position on the observation monitor (see coordinate axis in Figure B.6B). Rotation of the wafer is then performed in order to bring the wafer reference marks to the same Y position on the view screen. After that, the rotation stage is locked to restrict the rotation movement of the wafer. This is followed by bringing the mask closer to the wafer by adjusting the Z stage attached to the mask holder. The actual proximity depends on the operation type that is most appropriate for the user's purpose: either contact-free or hard contact. Following that, the mask is then translated in the XY plane in order to center the wafer reference marks inside of the mask's alignment marks, as shown in

Figure B.5C. Once the alignment is finished, the two microscopes are moved out of the way, and the light source is turned "on" in order to start the exposure.

B.6 Characterization of Mask Alignment Accuracy

Table B.3 Resolution of the CBMA's Individual Components, Based on The Manufacturers' Specifications

Resolution Type	Value
Microscope Visual, μm	1.25
θ Sample Displacement, °	0.001
XYZ Mask Displacement, μ	1

The alignment resolution of the overall system depends on the limitations of each of the individual components that the CBMA is made up of: the microscopes' visualization, the θ stage's sample rotation, and the mask stages' XYZ displacement (see Table B.3). Thus, in order to attain optimal alignment accuracy, the digital microscopes should be at their maximum magnification of 245X (corresponding to a visual resolution of 1.25 μm per pixel) for fine alignment. Moreover, other factors such as the film thickness may also contribute to the imperfection of the alignment by increasing the distance between the mask and the wafer.(95) This makes it progressively more difficult to keep both the mask's marks and the wafer's within the microscope's depth of field. Consequently, the inability to focus on both of the marks simultaneously creates more room for error. Therefore, in order to test this hypothesis, we characterized how the alignment accuracy of our CBMA varies with respect to the different photoresist thicknesses: ranging from 5 to 120 μm.

The accuracy of the alignment was quantitatively determined from SU-8 prints which are constructed using two different mask patterns, as shown in Figure B.7A. The masks with feature size of 50 μm were printed on plastic transparencies at 10,160 DPI

(Fineline Imaging, Colorado Springs, CO). The first mask contains “bracket” patterns and the second mask has “dot” patterns. SU-8 resist films of various thicknesses, ranging from 5 µm to 120 µm, were coated on a 4-in Si wafer containing positive photoresist alignment marks. The “bracket” mask was then aligned with the wafer following the protocol mentioned in the previous section. The photoresist layer was then exposed to UV radiation for a duration of 40 to 120 seconds, depending on the film’s thickness. After that, the “bracket” mask was replaced by the “dot” mask, and followed by alignment. The resists were then exposed at the same UV dose, baked at 95 °C for 5-10 min, and developed to generate the measurement patterns (see Figure B.7 B, C). Images of the patterns were acquired using a CCD camera Guppy Pro F-146 (Allied Vision, Germany) coupled to a reflected microscope Reichert Zetopan Trinocular (Austria). The acquisition was performed using a 10X objective (PLN10X, Olympus, Japan). Measurement of the patterns was conducted using open source ImageJ software.(64) Each of the experiments were performed in triplicate in order to ensure that the human error was minimized.

Upon successful alignment, the final SU-8 replica should contain the “dot” pattern centered inside of the “bracket” pattern, without offsets in any direction. Severe misalignment leads to the overlapping of the “dot” on the “bracket”, as shown Figure B.7B. In contrast, careful alignment results in a well-defined print that looks closer to what is expected from the superposition of the two masks (see Figure B.7C). The aligned patterns were then used for the characterization of the alignment accuracy. Figure B.7D demonstrates how the translational and rotational alignment errors are determined quantitatively.(94) Namely, the translational errors Δx and Δy were calculated from the offset of the “dot” pattern with respect to the “bracket” pattern in the x and y directions,

respectively. In addition, the mean translational error ΔL was calculated by averaging the translational errors in the two individual directions. On the other hand, the rotational error Δθ was determined from the angular amount that the former pattern was offset from the latter one. In practice, errorless alignment (i.e., zero delta values), is not possible even with a state-of-the art mask aligner, which can achieve sub-micron alignment accuracy.

Surprisingly, both the translational and the rotational effective accuracies were found to not be highly dependent on the film's thickness (Figure B.7E, F); however, the thinner ones resulted in a higher consistency (Figure B.7E). With film thickness of 50 μm or thinner, the translational errors appear to increase with the resist's thickness. Typically, the 5-μm film thickness resulted in average translational and rotational errors of 2.96 ± 0.92 μm and 0.062 ± 0.012°, respectively. Alignment errors of 20 and 50-μm thick prints were 4.29 ± 0.74 μm, 0.018 ± 0.0007° and 5.36 ± 4.04 μm, 0.045 ± 0.012° respectively. On the other hand, the rotational errors did not exhibit any distinguishable pattern, with values ranging well below 0.1° for all thickness values. This is likely due to the high resolution of the rotation stage, which is about an order of magnitude higher than the alignment accuracy of the translational stages. Finally, to our surprise we were able to achieve a high accuracy with the 120-μm thick film (3.12 ± 2.65 μm, 0.036 ± 0.025°), suggesting that film's thickness is not the only factor that hampers the alignment. For example, other factors like vibration, glare, unevenness in the transparency mask, and others could have also contributed to the variation in the alignment results.

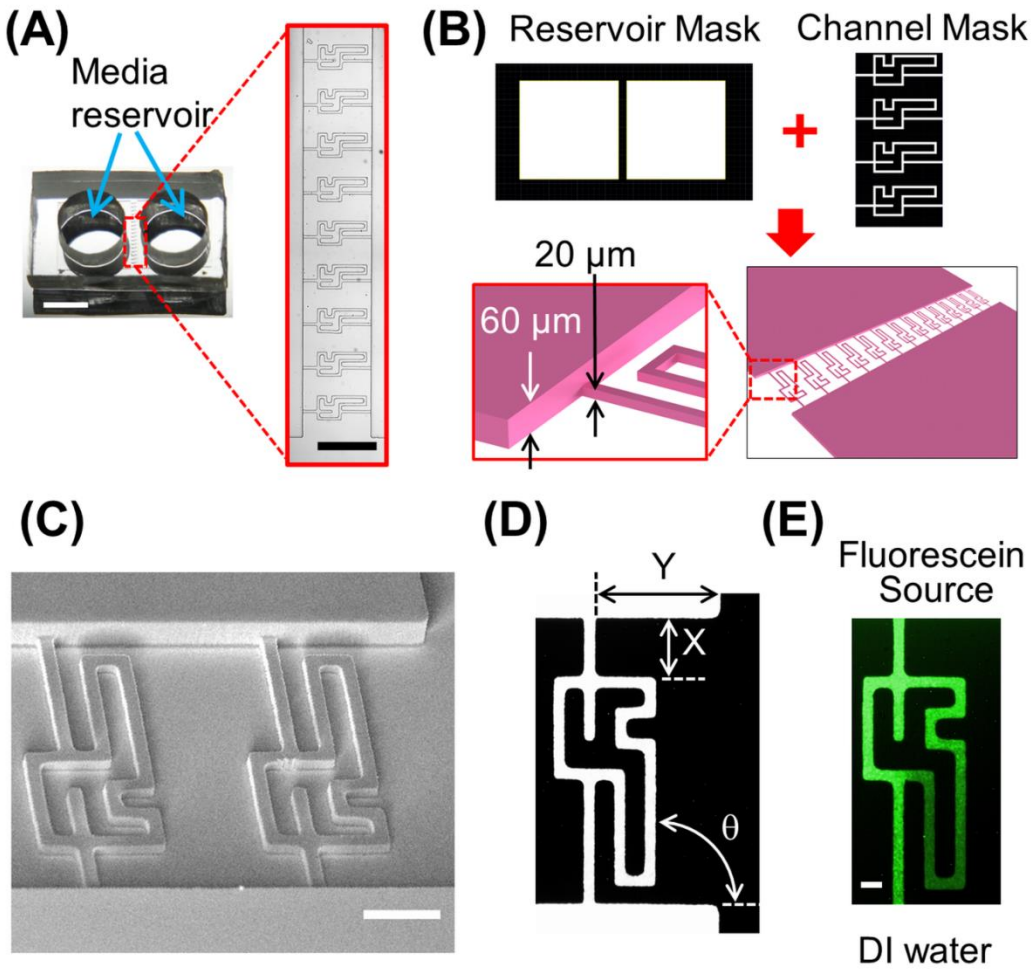

Figure B.8 (A) A photograph of the chemotaxis microfluidic device used as a demonstrative application of our CBMA. The device consists of an array of 15 x 20 (W x H) µm channels connecting two media reservoirs of 60-µm in height. Inset is a bright-field microscopy view showing how the microfluidic channels connect the two media reservoirs. Scale bar is 4 mm for the photograph and 400 µm for the inset. (B) Two photolithography masks used to fabricate the master mold for the device: one for the reservoir and one for the channel. Bottom is a 3D drawing of the resulting mold. (C) SEM image of the fabricated two-height SU-8 master. Scale bar is 100 µm (D) Interpretation of how the alignment of the device is characterized. The quantities ΔX, ΔY, and $\Delta\theta$ are calculated from the difference in X, Y, and θ between the device and the reference mask. (E) Fluorescent microscopy image of fluorescein gradient formed inside the micro channel of a PDMS device. Scale bar is 50 µm.

B.7 Mask Aligner Application

In order to demonstrate an application of our CBMA, we fabricated a SU-8 master mold for a PDMS device similar to ones commonly used to study cell chemotaxis in response

to a concentration gradient of a chemoattractant (see Figure B.8A).(22, 96-98). The device consists of an array of 20 μm-high diffusion "maze" channels that connect two identical reservoirs, each of which are 60 μm in height. In the chemotaxis application, one of the reservoirs is meant to hold the cells, while the other typically serves a source of the chemoattractant. In order to generate the device, a master of two different heights (20 and 60 μm) was fabricated from SU-8 photoresist using two different masks: one for the reservoir and one for the diffusion channel (see Figure B.8B). The distance between the two reservoirs was 462 μm and the distance between the two ends of the channel was 482 μm. Since, carrying out experiments in parallel requires that the mazes are identical, it is critical to align the two mask patterns accurately. Moreover, any mismatch between the diffusion channel and the reservoir would result in the malfunction of the device. Scanning electron microscopy (SEM) image (Figure B.8C) shows that a two-thickness master was successfully generated. SEM was acquired at 45° tilt angle using Field Emission Scanning Electron Microscope (FESEM, LEO 1530VP, Zyvex, Richardson, TX). Prior to imaging, the sample was sputter coated with 5-nm thin gold layer using a sputter coater (EMS150T ES, Quorumtech, Lewes, UK).

The alignment accuracy of the device was characterized in the x, y, and θ directions (Figure B.8D), using the same procedure as in Figure B.7D. The quantities Δx and Δy were determined to be $\pm$ 3.9 μm, while $\Delta\theta$ was 0.02°. This result suggests a successful alignment of the device.

We further investigated the performance of the device by testing chemical gradient generation within the diffusion channel using fluorescence tracer Alexa Fluor 488 (Thermofisher, Waltham, MA). The top of the reservoirs was punctured by a 5-mm biopsy punch in order to form a circular inlet port for the liquid media input. The

fluorescent solution (Alexa Fluor 488 (1 µg ml^{-1}) in deionized water) was added to one of the reservoirs, while deionized water was added to the other reservoir. Figure B.8E show that the resulting concentration profile of the tracer established inside the channels, between the source and the sink of the fluorescein. This result suggests that the device functioned successfully without any defects (i.e., no mismatch between the channels and the reservoirs) and was able to generate a stable gradient, which is suitable for a chemotaxis study of cells. Fluorescence microscopic images were acquired using an inverted microscope (IX83, Olympus, Japan) coupled to a 488-nm laser light source.

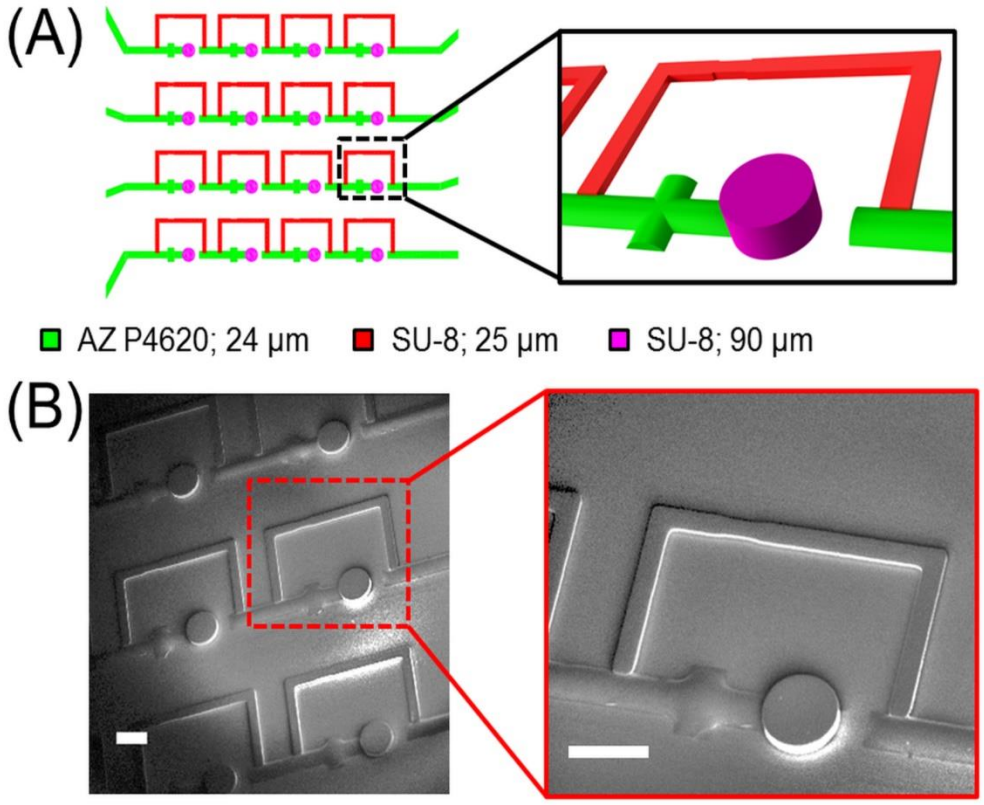

Figure B.9 (A) Design of a master mold for the "flow" layer of an addressable stencil device that consists of three photoresist patterns of various heights: 24-µm high main flow channel made out of positive photoresist AZ P4620 (green), 25-µm high bypass channel made out of negative photoresist SU-8 (red), and 90 µm-high delivery port made out of SU-8 (pink). Colors indicate individual photoresist patterns achieved *via* different photomasks. (B) SEM images showing different feature heights of the resulting master mold. Scale bars are 200 µm.

In a second application, we use our CBMA to fabricate something even more complex: a 3-height replica of an addressable stencil device, which was inspired by a work published by others.(88) This type of device is commonly used to deliver varied concentrations of chemicals to different "addresses" in the chip. Typically, the stencil device is comprised of three PDMS layers: a "control" layer, a "flow" layer, and a "display" layer. However, since the "control" and the "display" layers require just a single-height master mold (which could be easily fabricated using just a UV lamp without the need for a mask aligner), we focus exclusively on the fabrication of the 3-height "flow" layer master-mold. This fabrication includes the use of three different mask patterns: a 24-μm high main flow channel to transport liquid from a media source, a 25-μm high bypass channel, and a 90-μm high port pattern to deliver media to the "display" layer underneath (Figure B.9A).

In order to generate this master mold, a 3-exposure process was conducted using three different photomasks, each of which corresponds to a featured pattern. Firstly, the flow layers was fabricated by double coating the positive photoresist AZ P4620 to obtain 24-μm thick film on an "reference" mark-containing 4-in Si wafer, following a 3-min soft bake at 110 °C. Then the wafer was aligned with a photomask containing the pattern for the flow channel, and exposed to UV (2 mW cm^{-2}) for 960 seconds using the CBMA. The resists were developed and heated to 150 ℃ on a hot plate for 20 min to generate a round channel profile, as well as for improving the adhesion of the resist to the wafer for subsequent fabrication. After that, the wafer was coated with a 25-μm thick layer of the negative photoresist SU-8 2015, aligned with the second mask containing the pattern of the bypass channels, and exposed to 75 seconds of UV (2 mW cm^{-2}) . It was then developed and heated on a hot plate at 150 °C for 5 min. Next, the wafer was coated with

90-µm thick SU-8 2035, aligned with the third mask containing the pattern for the ports, and exposed to UV (2 mW cm^{-2}) for 110 seconds. Finally, the wafer was developed, and hard baked at 150 °C for 5 min to generate the final master. The master was then examined using SEM. The SEM images reveal that the master was successfully generated, with all the patterns were well aligned with each other (Figure B.9B).

B.8 Conclusion and Future Work

In this chapter, we demonstrated a cost-effective, lightweight, and accurate custom-built CBMA for the fabrication of multi-height photoresist patterns which are subsequently used as master molds for microfluidic applications. The CBMA was approximately tenfold cheaper than analogous commercial systems, thus making it suitable for medium and small laboratories in need of in-house microfluidic device fabrication. Owing to its lightweight and space-saving feature, the CBMA can be integrated into any lab space as a bench top unit. In addition, it is suitable for thick resist layers (> 100 µm) with an alignment accuracy of <3 µm, making it a potential replacement for the high-cost, high-maintenance commercial systems typically used in microfabrication.

Although our CBMA, is capable of achieving a wide spectrum of layered features that cover most of the microfluidics applications in its presented form, several major and minor improvements can be made to it based on the user's needs. For example, a simple enhancement can be achieved *via* supplementing the two alignment microscopes with a dedicated tablet PC each (simple ones can cost as low as ~$100). This can save the user time involved with connecting/disconnecting the microscopes to computers and monitors every time the CBMA is used.

Another possible upgrade is automating the alignment stages with electronic controllers. For example, the manual rotation stage can be replaced by a motorized

version (#URS75BPP, Newport); while the linear translation stages can be actuated by motorized actuators (#TRA25, Newport). This can both make the resulting products more accurate and repeatable by eliminating the possibility of inaccuracy introduced by manual operation error. However, the increased price associated with the automation and the need for custom software are, of course, the trade-off with this option.

Additionally, the use of Grating Light Waves (GLV), Digital Micro-mirror Devices (DMD), Spatial Light Modulators (SLM), and Liquid Crystal Displays (LCD) as electrically controllable active photomasks has recently become increasingly common because it can significantly simplify the 3D structuring of the photoresist.(99, 100) In this case, a computer-generated pattern serves as a reconfigurable mask in the lithography system, rendering a mask alignment procedure unnecessary because the position of the photomask is always fixed. Although alignment of the wafer with the mask may still be necessary (e.g., if multiple coatings of different photoresists are required), the active-mask photolithography makes the pattern alignment precise at the exposure plane and allows for rapid fabrication of 3D microstructures. Among these, the LCD is an especially promising for high-resolution lithography, because of its small pixel size: 8.5μm vs 17μm for DMD.(99, 100) Moreover, the LCD mask enables "gray-tone" photolithography (useful for tapered devices)(101) by allowing the user to adjust the percent transmittance of each individual pixel in order to produce advanced 3D features.

Other potential design modifications could include exposing the photoresist from the bottom by defining the mask as a part of the substrate.(102) By spinning the photoresist directly on to the mask, perfect contact alignment is achieved enabling the fabrication of tall high aspect ratio structures. Finally, recent exciting developments in LED technology such as the Nano-LED single photon lithography, could potentially be

implemented in our CBMA once the technology matures. (103) The advantage of this LED type is that it can significantly improve the resolution (down to molecular scale) while at the same time eliminating the need for a physical photomask if arranged in an electronically driven individually addressable array.

APPENDIX C

CUSTOM-BUILT GRAPHIC USER INTERFACE FOR TIME-LAPSE ACQUISTION OF MICROSCOPY IMAGE

C.1 Introduction

Live time-lapse microscopy is essential for a wide range of biological applications, including studying tissue engineering cultures as well as monitoring cell signaling and behavior.(104-106) Unlike sacrificial analysis methods, where results for each time point are collected from a *different* sample, time-lapse microscopy provides a *continuous* record of the experiment. This yields more complete information about the biological phenomena at hand. However, given that most biologically-relevant time scales require long-term experimentation, manual time-lapse microscopy becomes too cumbersome for human labor. Consequently, software-based automation offers a solution for overcoming this problem.

However, a big challenge for such software is that biological experiments typically involve multiple hardware components in addition to the microscope itself (e.g., motorized stage, filter turret, fluorescence light source, laser, and digital camera.) These components are often made by different companies, each of which provides proprietary drivers and software specific to the devices that they sell. Hence, the automation software must act as an "umbrella" that supports the individual drivers that come with the hardware, and should be able to synchronize all these parts .

Several such commercial software packages exist, such as MetaMorph7 (Molecular Devices, San Jose, CA), Element 4 (Nikon, Tokyo, Japan), iQ 2.6 (Andor, Belfast, UK), and cellSens (Olympus, Japan). Although these can drive a large number of *microscopy* devices and provide some basic image processing capabilities, they also have

significant disadvantages: (1) prohibitive cost, (2) lack of complex programming capabilities, such as hardware automation, image analysis, and mathematical modeling, and (3) inability to communicate with *non-microscopy* hardware, such as solenoid valves, syringe pumps, culturing chambers, and other electronic devices that are commonly used in biological experiments (e.g., microfluidics).

In addition to these commercial solutions, μManager (MM) is a free option that supports a wide range of *microscopy* hardware devices. Like the commercial analogues, it comes with its own graphical user interface (GUI) that provides basic experiment setup and data post-processing capabilities.(107) Consequently, it has become a popular tool for microscopy imaging.(108, 109) However, the MM GUI is limited to basic experiment customization/automation functionality, and only a few additional features are provided *via* external plug-ins. It does not allow for complex structured programming, or non-microscopy functions that could be useful, such as image processing, mathematical analysis and the ability to communicate with *non-microscopy* hardware.(110) For these purposes, application programming interfaces (API)(111) are provided that allow the user to interface with more advanced programming environments, such as Java, C++, and Matlab®.(112)

Among these, Matlab enables a much wider range of experiment customization *via* toolboxes like Computer Vision and Image Processing, Supercomputing, and Machine Learning. Another advantage of Matlab is that it offers support for a wide range of *non-microscopy* hardware.(113) Matlab offers support for ARM, Arduino, Altera, National Instruments, Raspberry Pi, Xilinx, Android, STMicroelectronics, and other devices that are frequently integrated into biological experiments. Finally, despite being a commercial package, Matlab is available to most researchers through their universities.

For these reasons, Matlab is the natural choice for implementing the advanced automation of microscopy experiments *via* MM.

Despite the benefits of this method, developing custom Matlab code which sends commands to the microscopy hardware *via* MM is an impractical undertaking for most labs. Development can be time intensive and challenging because there are only a few examples (most of which are very simple) available in the online Matlab documentation. Furthermore, most of the basic functionality around the microscope (e.g., capturing and stitching images, moving the stage, changing objectives, compensating for vibrations and artifacts, etc.) should be the same for different labs, rendering the work of creating the code redundant. Finally, even if one is successful in writing such Matlab-MM automation code, it would likely be difficult for other lab members who lack an advanced programming background to use it. Therefore, a Matlab-MM GUI would be ideal for simplifying the end-user experience, while also retaining the flexibility of utilizing advanced Matlab features for experiment customization and automation. Yet, adding a GUI on top of Matlab-MM is even more labor-intensive and redundant. Hence, the microscopy community would benefit from a freely-available Matlab-MM GUI that contains all of the basic features expected of microscopy software. This would save researchers time by providing them with a substantial starting point that they can then build upon in order to meet their specific needs.

To that end, this manuscript offers such a Matlab-MM GUI to the public as an open-source code. The GUI contains a wide variety of fundamental microscopy control and image acquisition features, as well as some additional post-processing functions. Some of the latter include stitching multiple tiles into a single panorama, light intensity flattening, and tile-based video stabilization. Although the code was developed using the

Olympus IX83 platform, in principle it should be compatible with any other hardware brands as long as they are supported by MM. This code will benefit researchers by providing them with a template for adding their own features into it. Some examples of the possible advanced customizations using Matlab include enhancing the experiment *via* support for additional electronic devices and/or with feedback loops based on real time image interpretation *via* computer vision; increasing computational processing power by off-loading data analysis to supercomputers and then retrieving the results automatically; and supplementing experimental analysis with COMSOL® Multiphysics simulations using the Matlab Livelink® interface. Not only would these enhancements save time for others, but they would also open up limitless new possibilities in terms of experiment design

C.2 Methods

C.2.1 Hardware and Software

Our GUI was developed on hardware commonly used by biological research laboratories. As noted earlier, our code is compatible with any hardware supported by MM. The hardware mentioned in this text serves were chosen as an example to demonstrate our software's capability. The individual components used in the setup include an inverted two-deck microscopy system (IX83, Olympus, Japan), an XY motorized linear-encoded translational stage (96S106-O3-LE2, Ludl, NY), a digital complementary metal-oxide semiconductor (CMOS) camera (Orca Flash V4.0, Hamamatsu, Japan), and a custom-built workstation with 64-bit operating system Microsoft Window 8.1, an Intel Xeon E5-2650 Processor (2x 2.00 GHz), 16 GB of DDR3 RAM, and a 512 GB SATA 2.5" solid state hard drive. The Ludl stage is driven by a motor drive controller (MAC 6000, Ludl)

which is connected to the computer *via* universal serial bus 2 (USB2) interface. The camera is connected to the computer *via* USB3. The microscope itself is a fully automated platform that is comprised of several modules that can communicate with a computer *via* a firewire interface. In particular, it includes: a motorized long working distance (LWD) condenser (IX3-LWUCDA, Olympus) which can switch between phase contrast and bright field, but can also act as a shutter for the camera; a motorized/coded fluorescent mirror turret (IX3-RFACA, Olympus); the microscope body (IX83P2ZF), which contains a motorized nosepiece for switching between objective lens as well as moving the objectives in Z direction for sample focusing; an LED lamp house (IX3-LHLEDC) whose illumination power can be controlled externally; and an autofocus module called the Z-drift compensator (IX3-ZDC), which can search for the shift in the imaging plane and compensate for it during the course of the experiment. The microscope uses objective lenses of various magnifications for different purposes. There are 1.25X objective lenses (PLAPO1.25X, NA 0.04, Olympus) for fast acquisition of a large "overview" area for region of interest (ROI) selection, 10X phase contrast objectives (UPLFLN10X PH1, NA 0.30, Olympus) for acquiring the phase contrast image, and 60X objectives (LUCPLFLN60XPH, LWD NA 0.70, Olympus) which work with the ZDC module for autofocus.

The latest version of μManager (Version 2.0 Beta) does not support the Olympus IX83 microscope, which is a popular brand and has been widely used in biological research. In order to make our code compatible with a wider range of microscopes, we built it using the older version 1.4 of μManager. The GUI was built using Matlab R2016b, but a newer version of Matlab can still be used with minimal modification of the code. The GUI was produced using a Matlab Tool called the GUI Development

Environment (GUIDE). The GUI elements (i.e. buttons, check boxes, message boxes, dialog boxes, and drop-down list) are designed and organized using the GUIDE layout. The elements' functions are defined using the command window of the Matlab GUI. Postprocessing is done with ImageJ version 1.5n, a free open source image processing tool.(64)

C.2.2 Microfluidic Device Fabrication

The microfluidic device was fabricated from a silicone elastomer poly(dimethyl siloxane) (PDMS, Sylgard 184, Dow Corning, MI) using soft lithography techniques. The master mold for the device was generated using a negative photoresist (SU-8 2015, MicroChem, MA). First, the microscale pattern was sketched using AutoCAD (Autodesk, Mill Valley, CA) and printed at 16,525 dpi on a transparency to generate a high-resolution photomask. The SU-8 was spin coated, exposed to UV light, and developed on a 4-inch silicon wafer to generate micron-sized channels. Then, PDMS with a base-to-agent ratio of 10:1 was poured over the mold and cured at 65 °C overnight. The cured PDMS was removed from the master mold and treated with air plasma prior to being bonded to a glass substrate. Right after bonding, the channels were coated with poly-D-lysine to enhance cell attachment.

C.2.3 Cell Preparation and Culturing

Mouse embryo NIH/3T3 (ATCC® CRL-1658TM) fibroblasts were purchased from ATCC (Manassas, VA). Prior to being transferred to the microfluidic device for the migration experiments, the cells were incubated in culture media inside of T75 flasks. The flasks were kept at 37 °C and in a humidified atmosphere of 5% CO_2 in air. The culture media was changed every two days to ensure normal cell growth. Prior to the migration experiments, the cells were trypsinized from the T75 flasks and loaded into the

devices, with a seeding density of about 50,000 cells cm^{-2}. The devices were incubated at 37 °C under 5% CO_2 for 6 h to allow cell attachment. Then, the cells were cultured in serum-starved media (MEM supplemented with 1% penicillin-streptomycin) for 6 hours.

C.2.4 Cell Migration Experiments and Image Acquisition

At the start of the experiment, the cell culture media in the chip was replaced with CO_2-independent basal media buffered by HEPES. 20 µL of basal media supplemented with 50 ng mL^{-1} PDGF-BB was then added into the central reservoir of each device. The devices are placed inside a condition chamber maintained at 37 °C mounted on top of the motorized stage of the microscope. Time-lapse phase-contrast imaging of the fibroblast migration was performed using the 10X phase-contrast objective. Images were automatically captured at 10 min intervals for the duration of 18 hours. For each device at each time step, 25 or 36 tile images were acquired at various locations, with autofocus enabled. Images are stitched and stabilized using the GUI.

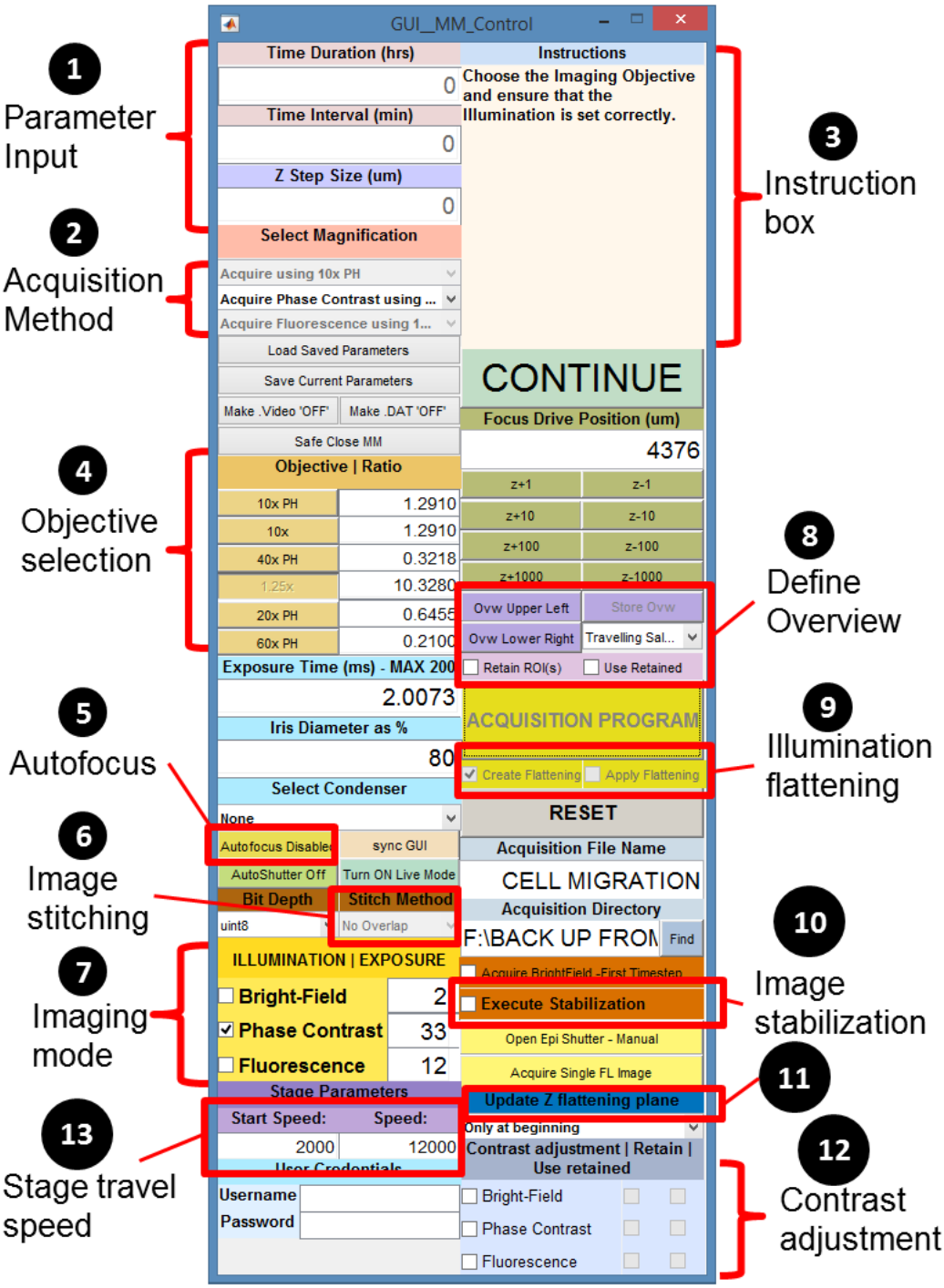

Figure C.1 Structure of the Matlab-based Graphic User Interface with different options and functions.

C.3 Description of the GUI and Instructions for Its Use

The GUI code can be readily downloaded from: https://git.njit.edu/rvoronov/ROBOSCOP.git, while MM is available at: https://micro-manager.org/wiki/Download%20Micro-Manager_Latest%20Release For the latter we recommend version 1.4.21, as it is the latest to support the Olympus IX83 microscope.

C.3.1 Setting up the μManager-Matlab Environment

The following instruction show how set up Matlab interfacing with μManager for Windows computers (adapted from μManager web page) (114, 115)

1. Install μManager (version 1.4) to "C:\Micro-Manager-1.4". From Windows, open the Command Prompt and type in "cd C:\Micro-Manager-1.4". Then, use the following command to save a list of all *.jar files in the folder: *dir /s /b /o:gn *jar > jarlist.txt*. This will create a new file called jarlist.txt in the current folder.

2. Open Matlab and run : *edit([prefdir '/javaclasspath.txt']);*. This opens a .txt file within the Matlab interface. Copy all of the filenames from jarlist.txt and paste them into the .txt file opened by Matlab. Save and close the file.

3. In Matlab, type: *edit([prefdir '/librarypath.txt']);*. Copy the μManager installation path (i.e. "C:\Micro-Manager-1.4") to this .txt file. Save and close the file.

4. Restart Matlab. μManager can now be started through Matlab using the following two commands (already integrated into our code): *import org.micromanager.MMStudio; gui = MMStudio(false);*

5. Set up the MM hardware configuration wizard (the GUI code obtains the objective labels from the MM hardware configuration profile *.cfg).
6. Finally, run the OLYMPUS_MICROMANAGER_GUI.m using Matlab in order to initiate the Matlab-MM GUI.

Structure of the GUI is shown in Figure C.10. Different elements of the GUI and their functions are described below:

7. PARAMETER INPUT: Dialog boxes that allow the user to input parameters such as the duration of imaging, time interval, and Z step (the distance interval the objective lens moves in the Z direction between a defined travel range). Usually, for 2D imaging in which the objective lens is fixed in the Z direction, the Z step is set to 0. In the case of imaging at different Z planes (i.e. for 3D construction), the Z step needs to be defined by the user. Z step is set in μm.

8. ACQUISITION METHOD: By default, the image acquisition is performed using a 10X objective for all of the imaging modes. If the user wants to image to a different magnification, they can select it from the drop down list.

9. INSTRUCTION BOX: A static box displaying instructions to guide the user through each step of the set up process.

10. OBJECTIVE SELECTION: Buttons allow the user to manually switch between objective lenses without actually touching the microscope hardware. Each number in the "Ratio" column indicates the pixel size (in µm) of the image acquired using the corresponding objective lens. (Note: the micron-to-pixel ratios are either calibrated or estimated in MM, and subsequently pulled from the hardware configuration *.cfg file by the GUI) .

11. AUTOFOCUS (OPTIONAL): A button that, once enabled, can send Matlab commands to the Z drift compensating module *via* µManager. The Autofocus function needs to be activated by checking "Focus Limit Settings" on the microscope control pad (Figure C.11A). This is indicated by the yellow line with a lock symbol on the bottom right corner of the acquisition window of the control pad (Figure C.2B). Even though this setting is specific to the Olympus IX83 microscope used in our setup, the setting procedure for other microscope brands should be analogous. Note: the GUI assumes that the *last* position in the motorized objective nosepiece is an autofocus-compatible objective (consult the autofocus instruction manual to check compatibility).

Figure C.2 Focus Settings on the touch pad of the IX83 microscope. (A) In order to activate the Z drift compensating IX3-ZDC module, Focus Limit Setting needed to be checked. (B) The main control panel showing a yellow line at a certain Z position. This indicates the ZDC has been activated and ready to be controlled by the GUI.

12. IMAGE STITCHING: A drop down list allows users to select different stitching methods. There are non-overlap and overlap stitching options. In the former method, the tiles have no overlapping in the field of view (FOV). Hence, the

stitching is done by merely positioning the tiles next to each other in the right order to form the panorama image. The latter, on the other hand, overlaps the tiles' FOV in order to produce seamless results by having the overlapping regions (20% overlap is chosen as default) serve as "registration marks" for the XY alignment of one tile onto another. Two options are available for the overlap stitching: "Grid: using BF" (which stands for bright field) and "Grid: using PC" (which stands for phase contrast). While the BF option relies on bright field imaging for the point feature matching, the latter is based on images collected from phase contrast microscopy. There is no option for stitching based on fluorescence (FL) tiles, since FL generally does not give sufficient information for registering all of the tiles. However, either BF or PC can be used to aid the stitching of fluorescence images. (*Note:* the stitching algorithim does not compensate for tile θ-rotation relative to each other. Hence, the orientation of the camera in the microscope's light port needs to be tuned manually by trial-and-error, using a sample with a distinct pattern across all tiles).

13. IMAGING MODE: Check boxes that allow users to select different imaging modalities (BF/PC/FL), and a dialog box that allows them to input the desired exposure time for each.

14. DEFINE OVERVIEW: A total imaging area is created using a low-magnification objective (1.25X by default, but could be chosen to be anys). Users need to define the upper left and lower right corner of an overview image by manualy moving the stage. A dropdown list allows users to select different travelling modes to optimize the travel of the XY stage (i.e. obtain the same number of images using the shortest travel path length or a user-specified one). Users can also either select the "Retain ROI(s)" option to restore the selected coordinates for future use, or "Use Retained" to skip the ROI selection by using coordinates restored from a prior aquisition.

15. ILLUMINATION FLATTENING: Users can select: (1) "Create Flattening", to create a reference "background" image for correcting Vignette illumination artifacts; or (2) "Apply Flattening", to subtract the background from current image using the reference created in (1).

16. IMAGE STABILIZATION: Once "Execute Stabilization" is checked, a Matlab function will be called to initiate an algorithm to generate a series of stabilized time-step images, which will be saved in "Stabilized" folder, located in the same folder that contains the stiched images.

17. UPDATE Z FLATTENING PLANE: The user can specify how frequently the autofocus takes place during the acquisition by selecting from a dropdown list the "x" number of time steps between two consecutive autofocus events. The hardware autofocus uses a laser beam to measure the distance from the objective to the sample, and then updates the objective height accordingly to keep the sample in focus. In our code, the measurement takes place at the four corners of the user-defined "overview" region (see Step 8 above). To that end, the frequency with which these measurements are updated throughout the aquisition is

controlled by the user here. For example, if "only at beginning" is selected, the autofocus only happen before the 1st time step, while "every 5 time steps" means the autofocus will happen every 5 time steps during the whole imaging sequence. Once the autofocus measurements are obtained, a 3D plane is fitted to these points, and is subsequently used to interpolate the appropriate Z height of the objective at every individual tile (see section 2.12 for additional information). The same interpolation plane is used until it is updated with a subsequent autofocus measurement. If more than 3 autofocus measurements fail for any reason, the code defaults back to the interpolation plane from the most recent successful measurement.

18. CONSTRAST ADJUSTMENT: This function allows the user to adjust the contrast of each ROI and each imaging mode (i.e. BF, PC, and FL) before a time-lapse acquisition is run. This function is needed to prevent the final image from being too bright or too dark, according to the user's preference.

19. STAGE TRAVEL SPEED: Here the user can manually input the travelling speed of the motorized stage. By increasing the travel speed, the user can achieve faster image acquisition. However, higher travel speed may lead to some issues with the imaging, such as blurring of the images. Moreover, the inertia force that may disturb the specimen (e.g. causing waves of liquid), especially at a high frequency. Hence the stage's speed should be chosen while keeping in mind the camera's exposure time as well as the overall experimental design.

The GUI also offers some basic control of the microscope without the user needing to touch the microscope's hardware. These controls include moving the objective in the Z direction, switching between objective lenses, swapping condenser optics, and changing the illumination power and the opening size of the iris diaphragm.

C.4 Hardware Synchronization and Software Communication

The synchronization between software and hardware is illustrated in Figure C.3. The Matlab-based GUI plays a central role in orchestrating all of these components by simultaneously communicating with μManager for hardware control while interfacing with ImageJ for image post-processing. The Matlab-MM interfacing allows the images to be acquired at different XY positions, Z planes, time intervals, and microscopy modes. The communications between μManager and the XY stage include toggling XY translation, real-time updating of sample position, and changing travel speed and

acceleration. The GUI interfaces with the camera in capturing images. In the case of bright field and phase contrast imaging, the image is captured using the camera's electronic shutter mode only to optimize the imaging speed, while in the case of fluorescence microscopy, the physical shutter of the microscope is used during the acquisition (i.e. between two consecutive stage's travel or between time steps) to avoid photobleaching of the sample. The GUI-microscope interaction includes controlling illumination, changing the Z position of the objectives, rotating the motorized objective nosepiece and the filter cube turret, swapping optics in the condenser turret, and opening/closing the epifluorescence shutter.

There are some basic image processing options that users can activate using the GUI. The processing requires communication between the GUI and other software. Image stitching is done using the Collection Stitching Plugin of ImageJ, which is launched using Matlab commands. Image stabilization is done *via* the Computer Vision System Toolbox in Matlab. Other functions such as rotation and brightness/contrast adjustment, which are created by the Matlab core commands, are also provided by the GUI .

C.5 Operational Instructions

C.5.1 Collect "Background" for Intensity Flattening (Optional)

Microscope raw images usually come with a vignetted features, which leads to detrimental artifacts on a stitched image. Therefore, a flat-field correction is necessary to remove the vignettes from the image tiles' background prior to stitching.(116) The flattened background for illumination is created using a reference sample. The reference sample can be a clean glass slide in the case of bright field and phase contrast microscopy

or a cover glass coated with a layer of fluorescein in the case of fluorescent microscopy. The flattening data is specific to the magnification and illuminiation parameters. Therefore, the objective magnification and its Z position, light intensity, exposure time, condenser iris opening, and microscopy mode (i.e., phase contrast, bright field, or fluoresecence) for creating flattening data must be the same as the one used in image acquisition. The below procedure describes a stepwise process of acquiring flattening data, which is normally done once, unless the imaging parameter is changed:

1.1. In the Select Magnification section, select the right objective from the drop-down list

1.2. Locate the folder where the raw images are saved.

In the GUI, check the "Create Flattening" box, then press "CONTINUE" to go to the next step. A live view window appears and the instruction box displays a guideline to select the upper left and lower right corner for an overview. By default, the microscope will change to lower magnification (1.25 X objective lens) to gain faster acquisition thank to its larger field of view.

1.3. Moving the stage to the upper left and right corners of the sample and registered

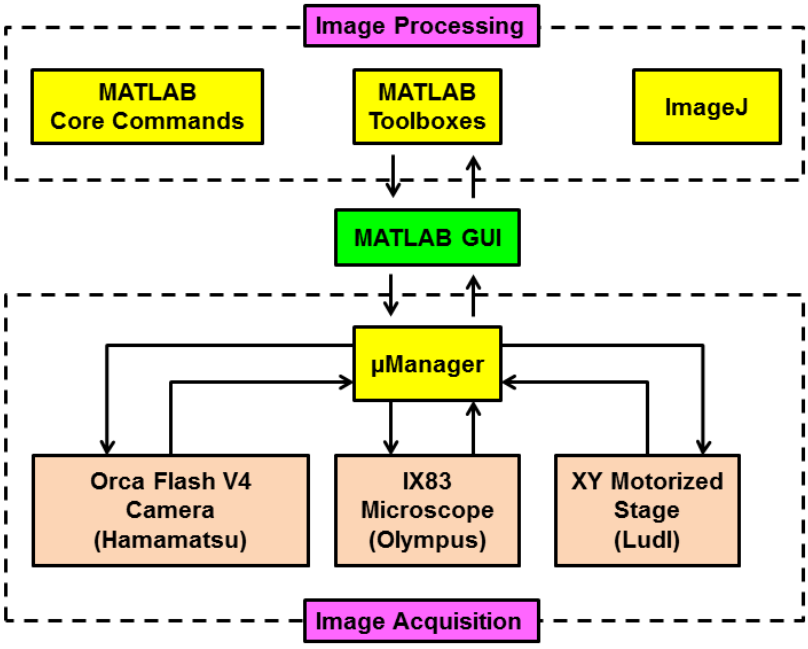

Figure C.3 Block diagram showing communication between software (MATLAB, µManager, and ImageJ) and hardware (automated microscope, motorized stage, and digital camera)

their coordinate by hit the “Ovw Upper Left” and “Ovw Lower Right” buttons, respectively, following by pressing the “Store Ovw” button. Once “CONTINUE” button is pressed, the microscope automatically starts acquiring image to build an overview of the selected area.

1.4. Once the overview window pops up, the user can select the ROI(s) by drawing rectangular box(es) around the region where he wants the background data to be collected (Figure C.4). Multiple ROIs may not be necessary in this case; however, the flattening can be improved when more reference images are acquired. After the ROIs are selected, hit “Crop All Selected Regions”.

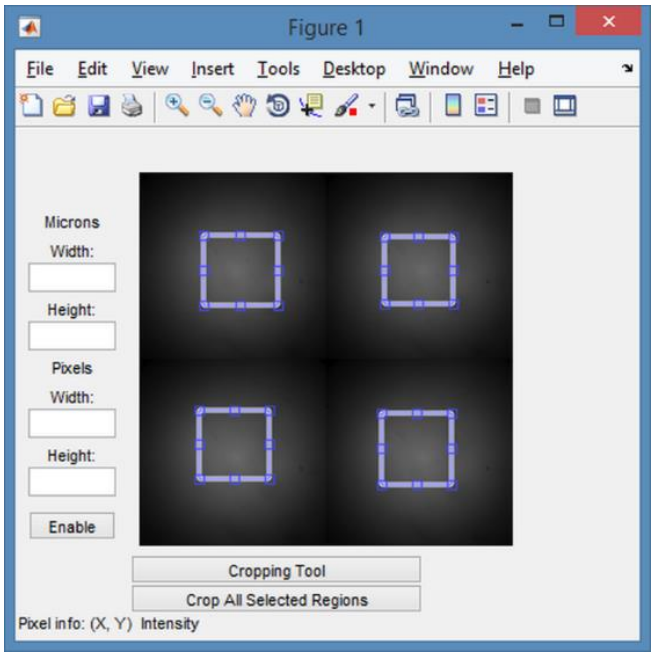

Figure C.4 Selecting region of interests (ROIs) from an overview. In this example, the overview was stitched from four image tiles captured using a 1.25X objective. The artifact in the overview is specific to 1.25 X objective. Hence, it does not affect the flattening data collected by other objective such as the 10X lens

1.5. The microscope then automatically switches to the imaging objective lens (i.e. 10X objective) selected earlier by the user. The sample is brought into focus by adjusting the Z position of the objective. After minimum and maximum Z is defined, the acquisition begins. The “average” images are calculated from ROIs and stored in the subfolder “resume”, which is located at the acquisition folder. These images will be used whenever “apply flattening” option is selected prior to acquisition.

C.5.2 Acquire High-Throughput Time-Lapse Images

The stepwise procedure below demonstrates the use of the GUI in generating time-lapse images of a large sample in a high-throughput manner. Note that all of the defined parameters are specific to this example and are subject to change upon the user's needs.

2.1. Press "ACQUISITION PROGRAM" to initiate the first step of the acquisition.

2.2. Enter an acquisition time of 18 hours, time step of 10 min, and Z step of 0 µm into the "Time Duration (hrs)", "Time Interval", and "Z step size (um)" dialog boxes, respectively.

2.3. In the "Select Magnification" section, select the acquisition method and the magnification from the dropdown list. Select "Acquire using 10X PH" and "Acquire Phase Contrast using 10X objective". These options indicate that the microscope should use the 10X phase objective and condenser lenses during the acquisition.

2.4. Press the "Autofocus Disabled" button to enable the Autofocus module. Once the button is clicked, its label is changed to "Autofocus Enabled".

2.5. Select image quality in under the Bit Depth section and select the stich method (i.e. "Grid: using BF"). The user can select either 8-bit (~ 2MB tile size) or 16-bit (~ 8 MB tile size). The latter comes with 4 times higher file size per image than the former one. However, its disadvantage is that it will quickly consume storage space.

2.6. In the "Illumination | Exposure" area, check the phase contrast and an exposure time of 33 milliseconds.

2.7. Select the stage travelling mode. There are two modes available: "User-defined" and "Traveling Salesman". The former takes into account the order in which the user selects the regions of interest (ROIs) (mentioned in step 2.11 below), and allows the user to manually define the stage traveling route. The "Traveling Saleman" mode, will trigger an algorithm that defines the shortest route for the stage travel (despite of the order in which the user selected the ROIs).(117) This is the most commonly used traveling mode.

2.8. Check "Apply Flattening" to use the flattening data created previously. At the end of each time step, the flattening data is used to generate uniform illumination of the tiles before they are stitched.

2.9. Define the image name in the "Acquisition File Name" box. Specify the location of the image folder in the "Acquisition Directory"

2.10. In the "Update Z flattening plane" section, select "every 5 time steps" to ask the microscope to run the autofocus event every 5 time steps to compensate to any movement/drifting of the sample.

After all the parameters/options are set, hit the CONTINUE button to proceed to the next step. The microscope will automatically switch to the low-magnification 1.25 X objective and μManager's live view window will be turned on, showing the camera view of the sample. Then continue to the following steps:

2.11. Define an overview of the imaging area by moving the sample to the top left position, hitting the "Ovw Upper Left" button, moving the sample to the bottom right position, and hitting "Ovw Lower Right" button. After that, press "Store Ovw" and "CONTINUE" to complete this process. The microscope will start to acquire an overview image of the sample using the low-magnification objective. After the acquisition is finished, all of the image tiles will be stitched to generate a full overview of the selected area (Figure C.5A). Define the ROI by drawing rectangles around the interested regions (Figure C.5B). Press "Crop All Selected Regions" once all the ROIs are selected to proceed to the next step.

The microscope will switch to the 60X objective lens (LUCPLFLN60x, 0.7 NA, 1.5-2.2 mm adjustable working distance, Olympus) to start searching for the reference focal point (i.e. the top surface of the coverslip where sample is present). Once the focal point is successfully located, the microscope will automatically switch to the acquisition objective lens (i.e., 10X Phase objective).

2.12. Define the maximum and minimum Z positions of the 10X objective. In the case of 2D imaging at a single focal plane, the max and min positions have the same Z value. Thus, for 2D imaging the user just needs to focus on the sample by moving the objective lens in the Z direction to attain the focused image shown on the live view window. However, if Z range needs to be specified, as is the case with 3D imaging, move the objective to the lowest Z value to register the minimum Z and to the highest Z value to register the maximum Z. (*Note: Do not manually move the sample in the XY direction after the autofocus. Otherwise, it will cause a miscalculation of the drift compensation*). After both the max and min Z positions have been specified, the Z positions of four reference points, which are the corners of the overview selected earlier, are determined. This step is necessary to compensate for the initial tilting of the sample. The Z position of individual image tiles can thus be determined by linear interpolation based on their relative position from the reference points. Once all the references have been recorded, a 3D graph illustrating a fitted plane will appear. After that, the acquisition begin. (*Note: these fitting graphs can be found in the subfolder "ZFlattening" located inside the*

acquisition folder, while detailed coordinates of the 4 reference points can be found in the "AcquisitionLog.txt" file).

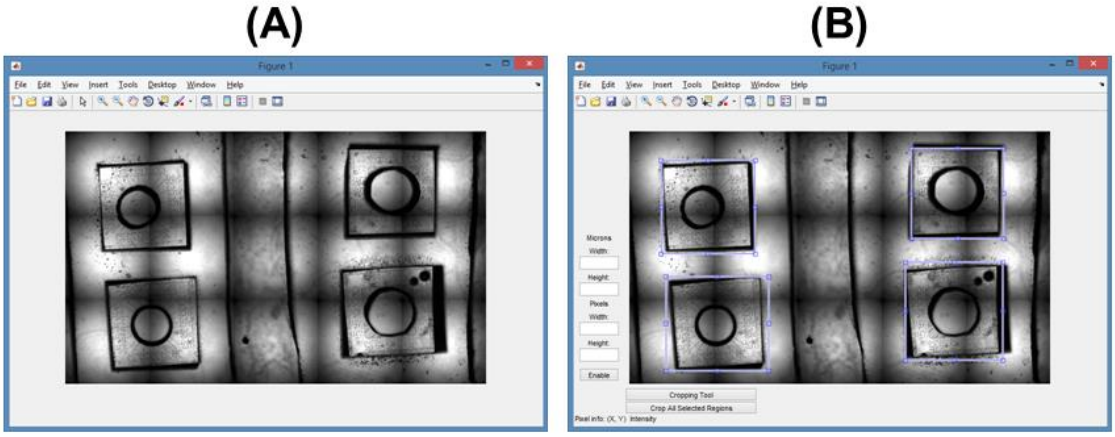

Figure C.5 (A) Overview of an imaging area acquired using 1.25X objective and stitched using ImageJ plugin. The "upper left" and "lower right" corners of the rectangular area are defined by the user using the GUI. (B) Regions of interest defined by the user. These selected areas will then be "cropped" from the overview, meaning that imaging only happens inside the crops while ignoring the rest of the overview

C.6 Applications

In the following section, cell migration (a typical time-lapse imaging experiment,(22, 118, 119)) is used to demonstrate the use of the GUI. For this experiment, the chemotaxis of fibroblasts inside a series of microfluidic maze channels is monitored. In order to recruit and guide the cell migration, a concentration gradient of platelet-derived growth factor-BB (PDGF-BB) was generated inside the channels using a flow-free gradient generator. Each microfluidic device contains multiple channels and several devices are placed inside a condition chamber (Figure C.6). This allows a high-throughput manner of study. Each selected ROI (step 2.11 above) corresponds to a maze device which has dimensions of 5x5 mm. At 10X magnification, the FOV of the camera is only 1.36x1.36 mm. Therefore, it needs 25 (for "No overlap" stitching type) and 36 (for BF or PC stitching type) tiles to build a panorama of an ROI.

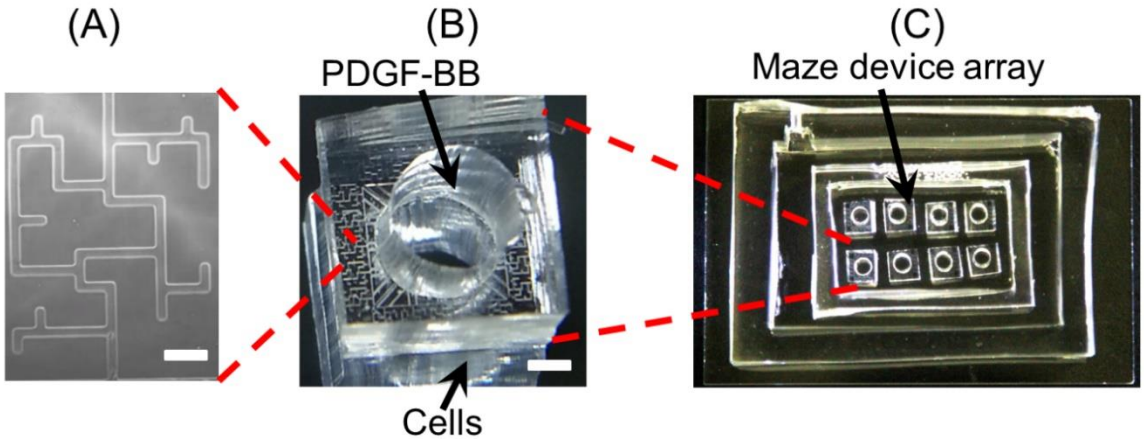

Figure C.6 Microfluidics maze device used in the experiment. (A) Micrograph of a single maze channels with 24 μm width. Scale bar is 100 μm. (B) Photograph of a single microfluidic device made from PDMS. The central hole is added with chemoattractant and cells are seeded to the outside. Scale bar is 1 mm. (C) Photograph of a chip which contains an array of maze devices.

The ability of the software to stitch raw tiles to produce seemless panorama of the ROI is demonstrated. Different stitching methods are compared (Figure C.7). The acquisition with "No Overlap" option does not generate tiles with overlapping pixels for registration. Therefore, misalignment occurs in both XY directions when these tiles are stitched (Figure C.7, top pane). The "Grid: using BF" and "Grid: using PC" options, on the other hand, yield images with about 20% overlaps, thus being able to create seamless bright field and phase contrast panoramas, respectively (Figure C.7, middle and bottom panes).

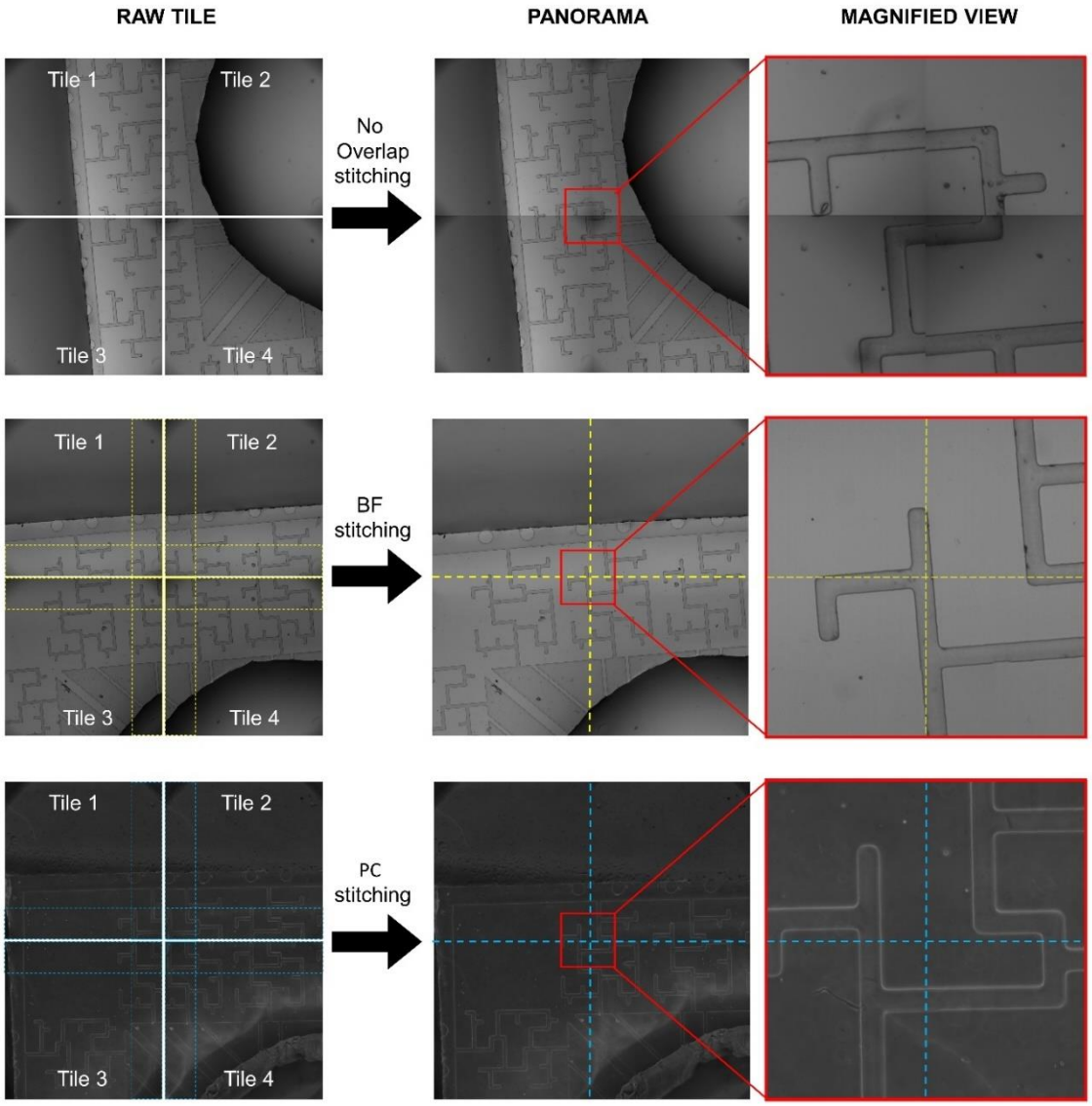

Figure C.7 Comparison between different stitching method. Top pane: Raw tiles are stitched using "No Overlap" option. Tiles are bright field images collected at 10X magnification. Middle Pane: Raw tiles are stitched using "Grid: using BF" option. Raw tiles are bright field images collected at 10X magnification. Bottom Pane: Raw tiles are stitched using "Grid: using PC" option. The tiles are generated from phase contrast mode. Dash lines in the left image show the overlaping areas between neighboring tiles. Dash line in the middle and right images indicate the border between different tiles.

In order to demonstrate the capability of the GUI to correct for shading issues, the imaging was performed with and without the "Apply Flattening" option, using bright field and phase contrast modes, acquired with 10X objective. When the flattening option

is disabled, the panoramas display 2D lattice-like artifacts as seen in Figure C.8A,B. These artifacts are created by the "vignette" corners of individual tiles, which is inevitable for the CMOS camera.(120) With "Apply Flattening" being enabled, the GUI eliminate artifacts using the flattening data created above. Thus, the shaded background is

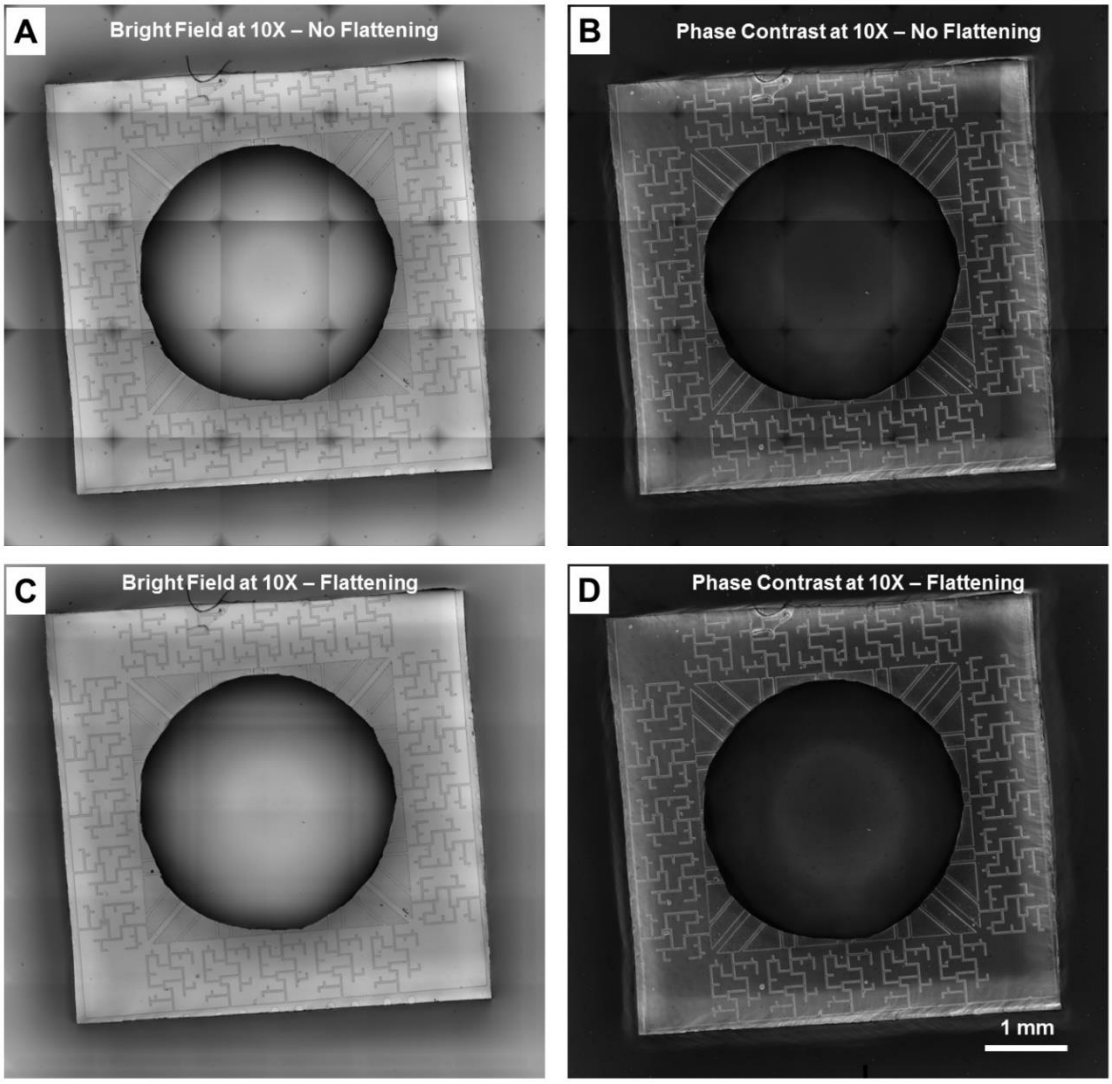

Figure C.8 Panorama produced from bright field and phase contrast image tiles obtained with 10X objective with and without flat-field correction or "flattening". (A) & (B) "Apply Flattening" option of the GUI is not selected. (C) & (D) "Apply Flattening" is enabled in GUI.

significantly diminished compared to the non-corrected version (Figure C.8C,D).

During acquisition, the mechanical movement of the stage is likely to introduce vibration which may result in blurry images and videos. Our GUI accounts for the frame-to-frame shifting of the images by using a stabilization algorithm, which compensates for the XY displacement of pixels in one image with respect to other images in the same sequence. The stabilization ability of the GUI is demonstrated in Video S1 (https://www.youtube.com/watch?v=DGpyypJozCA). When the "Execute Stabilization" option in the GUI is not selected, the final video appears to be "shaky" with static objects (i.e., the maze) moving from frame to frame (Video S1, LEFT). However, when the "Execute Stabilization" is enabled by the user, significant enhancement is achieved with static objects displaying negligible motion as seen in Video S1, RIGHT.

C.7 Conclusions

We introduced a Matlab-based custom GUI which can simultaneously communicate with the open-source, cross-platform program μManager for synchronizing hardware and with other software for image processing. It can cover a wide variety of basic controls of automated microscopes, digital cameras, motorized stages, illuminators, and other microscope accessories necessary for time-lapse imaging. These controls include automatically translating the XY stage; capturing images at a predefined frequency; switching between objective lenses, condenser optics, and filter cubes; autofocusing; and adjusting illumination. In addition, the GUI offers options for image processing, such as stitching image tiles for panorama generation, stabilizing time-lapse videos, and flat-field correction by background subtraction. Step-wise instructions for using the GUI were provided, and a demonstrative fibroblast chemotaxis experiment was described. In this experiment, images were automatically acquired on pre-defined regions over 18 hours at

a 10-min interval. The resultant panoramas were stitched from image tiles attained with bright-field and phase contrast microscopies, and they showed seamless features due to the application of flat-field correction. The GUI's image processing functions, such as flat-field correction and video stabilization significantly enhance the quality of the final images and videos. These results suggest that this GUI is useful for automating the process of generating high-quality, high-throughput time-lapse images and videos. Since this software is compatible with a wide range of hardware, it can be used by many biological research labs worldwide. Additionally, the Matlab source code is open to modification and upgradation, providing researchers with a foundation for adding in their own features, such as support for additional hardware control (i.e., microfluidic pumps, valves, and sensors) and software applications (i.e., data analysis, computational simulation, computer vision, etc.).

REFERENCES

1. Langer R, Vacanti JP. Tissue engineering. Science. 1993;260(5110):920-6.
2. Wobma H, Vunjak-Novakovic G. Tissue engineering and regenerative medicine 2015: a year in review. Tissue Engineering Part B, Reviews. 2016;22(2):101-13.
3. O'Brien FJ. Biomaterials & scaffolds for tissue engineering. Materials Today. 2011;14(3):88-95.
4. Ma PX. Scaffolds for tissue fabrication. Materials Today. 2004;7(5):30-40.
5. An J, Teoh JEM, Suntornnond R, Chua CK. Design and 3d printing of scaffolds and tissues. Engineering. 2015;1(2):261-8.
6. Solchaga LA, Tognana E, Penick K, Baskaran H, Goldberg VM, Caplan AI, et al. A rapid seeding technique for the assembly of large cell/scaffold composite constructs. Tissue Engineering. 2006;12(7):1851-63.
7. Hu D, Wu D, Huang L, Jiao Y, Li L, Lu L, et al. 3D bioprinting of cell-laden scaffolds for intervertebral disc regeneration. Materials Letters. 2018;223:219-22.
8. Wong T, McGrath JA, Navsaria H. The role of fibroblasts in tissue engineering and regeneration. British Journal of Dermatology. 2007;156(6):1149-55.
9. Singer AJ, Clark RA. Cutaneous Wound Healing. N England Journal of Medicine. 1999;341(10):738-46.
10. Li B, Wang JHC. Fibroblasts and myofibroblasts in wound healing: force generation and measurement. Journal of Tissue Viability. 2011;20(4):108-20.
11. Asuelime GE, Shi Y. A case of cellular alchemy: lineage reprogramming and its potential in regenerative medicine. Journal of Molecular Cell Biology. 2012;4(4):190-6.
12. Costa-Almeida R, Soares R, Granja Pedro L. Fibroblasts as maestros orchestrating tissue regeneration. Journal of Tissue Engineering and Regenerative Medicine. 2017;12(1):240-51.
13. Sriram G, Bigliardi PL, Bigliardi-Qi M. Fibroblast heterogeneity and its implications for engineering organotypic skin models in vitro. European Journal of Cell Biology. 2015;94(11):483-512.
14. De Donatis A, Comito G, Buricchi F, Vinci MC, Parenti A, Caselli A, et al. Proliferation versus migration in platelet-derived growth factor signaling: the key role of endocytosis. The Journal of Biological Chemistry. 2008;283(29):19948-56.
15. Albini A, Adelmann-Grill BC, Muller PK. Fibroblast chemotaxis. Collagen and Related Research. 1985;5(3):283-96.
16. Li W, Fan J, Chen M, Guan S, Sawcer D, Bokoch GM, et al. Mechanism of human dermal fibroblast migration driven by type I collagen and platelet-

derived growth factor-BB. Molecular Biology of the Cells. 2004;15(1):294-309.

17. Wu NL, Chiang YC, Huang CC, Fang JY, Chen DF, Hung CF. Zeaxanthin inhibits PDGF-BB-induced migration in human dermal fibroblasts. Experimental Dermatololy. 2010;19(8):e173-81.

18. Shreiber DI, Enever PA, Tranquillo RT. Effects of pdgf-bb on rat dermal fibroblast behavior in mechanically stressed and unstressed collagen and fibrin gels. Experimental Cell Research. 2001;266(1):155-66.

19. Schneider IC, Haugh JM. Mechanisms of gradient sensing and chemotaxis: conserved pathways, diverse regulation. Cell Cycle. 2006;5(11):1130-4.

20. Haugh JM, Codazzi F, Teruel M, Meyer T. Spatial sensing in fibroblasts mediated by 3' phosphoinositides. The Journal of Cell Biology. 2000;151(6):1269-80.

21. Schneider IC, Haugh JM. Quantitative elucidation of a distinct spatial gradient-sensing mechanism in fibroblasts. The Journal of Cell Biology. 2005;171(5):883-92.

22. Scherber C, Aranyosi AJ, Kulemann B, Thayer SP, Toner M, Iliopoulos O, et al. Epithelial cell guidance by self-generated EGF gradients. Integrative Biology (Camb). 2012;4(3):259-69.

23. Ambravaneswaran V, Wong IY, Aranyosi AJ, Toner M, Irimia D. Directional decisions during neutrophil chemotaxis inside bifurcating channels. Integrative Biology (Camb). 2010;2(11-12):639-47.

24. Prentice-Mott HV, Chang CH, Mahadevan L, Mitchison TJ, Irimia D, Shah JV. Biased migration of confined neutrophil-like cells in asymmetric hydraulic environments. Proceedings of the National Academy of Sciences of the United States of America. 2013;110(52):21006-11.

25. Mak M, Erickson D. Mechanical decision trees for investigating and modulating single-cell cancer invasion dynamics. Lab on a Chip. 2014;14(5):964-71.

26. Paul CD, Shea DJ, Mahoney MR, Chai A, Laney V, Hung WC, et al. Interplay of the physical microenvironment, contact guidance, and intracellular signaling in cell decision making. FASEB journal : official publication of the Federation of American Societies for Experimental Biology. 2016;30(6):2161-70.

27. Rao S, Tata U, Lin V, Chiao J-C. The Migration of Cancer Cells in Gradually Varying Chemical Gradients and Mechanical Constraints. Micromachines. 2014;5(1):13.

28. Albrecht-Buehler G. The phagokinetic tracks of 3T3 cells. Cell. 1977;11(2):395-404.

29. Albrecht-Buehler G. Daughter 3T3 cells. Are they mirror images of each other? The Journal of Cell Biology. 1977;72(3):595-603.

30. Abercrombie M, Heaysman JE. Observations on the social behaviour of cells in tissue culture. II. Monolayering of fibroblasts. Experimental Cell Research. 1954;6(2):293-306.

31. Chen HC. Boyden chamber assay. Methods in Molecular Biology. 2005;294:15-22.

32. Ozaki Y, Nishimura M, Sekiya K, Suehiro F, Kanawa M, Nikawa H, et al. Comprehensive analysis of chemotactic factors for bone marrow mesenchymal stem cells. Stem Cells Dev. 2007;16(1):119-29.

33. Riahi R, Yang Y, Zhang DD, Wong PK. Advances in wound-healing assays for probing collective cell migration. J Lab Autom. 2012;17(1):59-65.

34. Rodriguez LG, Wu X, Guan JL. Wound-healing assay. Methods in Molecular Biology. 2005;294:23-9.

35. Wu J, Wu X, Lin F. Recent developments in microfluidics-based chemotaxis studies. Lab on a chip. 2013;13(13):2484-99.

36. Sun W, Darling A, Starly B, Nam J. Computer-aided tissue engineering: overview, scope and challenges. Biotechnology and Applied Biochemistry. 2004;39(Pt 1):29-47.

37. McCoy RJ, Jungreuthmayer C, O'Brien FJ. Influence of flow rate and scaffold pore size on cell behavior during mechanical stimulation in a flow perfusion bioreactor. Biotechnology and Bioengineering. 2012;109(6):1583-94.

38. Hossain MS, Bergstrom DJ, Chen XB. Modelling and simulation of the chondrocyte cell growth, glucose consumption and lactate production within a porous tissue scaffold inside a perfusion bioreactor. Biotechnology reports (Amsterdam, Netherlands). 2015;5:55-62.

39. Zhao F, Vaughan TJ, McNamara LM. Multiscale fluid–structure interaction modelling to determine the mechanical stimulation of bone cells in a tissue engineered scaffold. Biomechanics and Modeling in Mechanobiology. 2015;14(2):231-43.

40. Guyot Y, Papantoniou I, Chai YC, Van Bael S, Schrooten J, Geris L. A computational model for cell/ECM growth on 3D surfaces using the level set method: a bone tissue engineering case study. Biomechanics and Modeling in Mechanobiology. 2014;13(6):1361-71.

41. Guyot Y, Papantoniou I, Luyten FP, Geris L. Coupling curvature-dependent and shear stress-stimulated neotissue growth in dynamic bioreactor cultures: a 3D computational model of a complete scaffold. Biomechanics and Modeling in Mechanobiology. 2016;15(1):169-80.

42. Guyot Y, Luyten FP, Schrooten J, Papantoniou I, Geris L. A three-dimensional computational fluid dynamics model of shear stress distribution during neotissue growth in a perfusion bioreactor. Biotechnology and Bioengineering. 2015;112(12):2591-600.

43. Alam TA, Pham QL, Sikavitsas VI, Papavassiliou DV, Shambaugh RL, Voronov RS. Image-based modeling: A novel tool for realistic simulations of artificial bone cultures. Technology (Singap World Sci). 2016;04(04):229-33.

44. Kurosaka S, Kashina A. Cell biology of embryonic migration. Birth defects research Part C, Embryo Today : Reviews. 2008;84(2):102-22.

45. Reig G, Pulgar E, Concha ML. Cell migration: from tissue culture to embryos. Development. 2014;141(10):1999-2013.

46. Franz CM, Jones GE, Ridley AJ. Cell migration in development and disease. Developmental Cell. 2002;2(2):153-8.

47. Scarpa E, Mayor R. Collective cell migration in development. The Journal of Cell Biology. 2016;212(2):143-55.

48. Rappel W-J. Cell–cell communication during collective migration. Proceedings of the National Academy of Sciences. 2016;113(6):1471-3.

49. Ellison D, Mugler A, Brennan MD, Lee SH, Huebner RJ, Shamir ER, et al. Cell–cell communication enhances the capacity of cell ensembles to sense shallow gradients during morphogenesis. Proceedings of the National Academy of Sciences of the United States of America. 2016;113(6):E679-E88.

50. Trepat X, Chen Z, Jacobson K. Cell migration. Comprehensive Physiology. 2012;2(4):2369-92.

51. Vedel S, Tay S, Johnston DM, Bruus H, Quake SR. Migration of cells in a social context. Proceedings of the National Academy of Sciences. 2013;110(1):129-34.

52. Miron-Mendoza M, Lin X, Ma L, Ririe P, Petroll WM. Individual versus Collective Fibroblast Spreading and Migration: Regulation by Matrix Composition in 3-D Culture. Experimental eye research. 2012;99:36-44.

53. Leong MC, Vedula SRK, Lim CT, Ladoux B. Geometrical constraints and physical crowding direct collective migration of fibroblasts. Communicative & Integrative Biology. 2013;6(2):e23197.

54. Levinstone D, Eden M, Bell E. Similarity of sister-cell trajectories in fibroblast clones. Journal of Cell Science. 1983;59:105-19.

55. Abercrombie M, Heaysman JE. Observations on the social behaviour of cells in tissue culture. I. Speed of movement of chick heart fibroblasts in relation to their mutual contacts. Experimental Cell Research. 1953;5(1):111-31.

56. Dona E, Barry JD, Valentin G, Quirin C, Khmelinskii A, Kunze A, et al. Directional tissue migration through a self-generated chemokine gradient. Nature. 2013;503(7475):285-9.

57. Kirfel G, Rigort A, Borm B, Herzog V. Cell migration: mechanisms of rear detachment and the formation of migration tracks. European Journal of Cell Biology. 2004;83(11-12):717-24.

58. Costa G, Harrington KI, Lovegrove HE, Page DJ, Chakravartula S, Bentley K, et al. Asymmetric division coordinates collective cell migration in angiogenesis. Nature Cell Biology. 2016;18(12):1292-301.

59. Yan J, Irimia D. Stochastic variations of migration speed between cells in clonal populations. Technology (Singap World Sci). 2014;2(3):185-8.

60. Paul CD, Mistriotis P, Konstantopoulos K. Cancer cell motility: lessons from migration in confined spaces. Nature Reviews Cancer. 2017;17(2):131-40.

61. Seppä H, Grotendorst G, Seppä S, Schiffmann E, Martin GR. Platelet-derived growth factor in chemotactic for fibroblasts. The Journal of Cell Biology. 1982;92(2):584-8.

62. Siegbahn A, Hammacher A, Westermark B, Heldin CH. Differential effects of the various isoforms of platelet-derived growth factor on chemotaxis of fibroblasts, monocytes, and granulocytes. Journal of Clinical Investigation. 1990;85(3):916-20.

63. Lepisto J, Peltonen J, Vaha-Kreula M, Niinikoski J, Laato M. Platelet-derived growth factor isoforms PDGF-AA, -AB and -BB exert specific effects on collagen gene expression and mitotic activity of cultured human wound fibroblasts. Biochemical and Biophysical Research Communications. 1995;209(2):393-9.

64. Schneider CA, Rasband WS, Eliceiri KW. NIH Image to ImageJ: 25 years of image analysis. Nature Methods. 2012;9(7):671-5.

65. Akar B, Jiang B, Somo SI, Appel AA, Larson JC, Tichauer KM, et al. Biomaterials with persistent growth factor gradients *in vivo* accelerate vascularized tissue formation. Biomaterials. 2015;72:61-73.

66. Haugh JM. Deterministic model of dermal wound invasion incorporating receptor-mediated signal transduction and spatial gradient sensing. Biophysical Journal. 2006;90(7):2297-308.

67. Menon SN, Flegg JA, McCue SW, Schugart RC, Dawson RA, McElwain DL. Modelling the interaction of keratinocytes and fibroblasts during normal and abnormal wound healing processes. Proceedings. Biological sciences. 2012;279(1741):3329-38.

68. Tse HTK, Weaver WM, Di Carlo D. Increased Asymmetric and Multi-Daughter Cell Division in Mechanically Confined Microenvironments. PLoS One. 2012;7(6):e38986.

69. Kisseleva T, Brenner DA. Mechanisms of fibrogenesis. Experimental Biology and Medicine. 2008;233(2):109-22.

70. Lerman OZ, Galiano RD, Armour M, Levine JP, Gurtner GC. Cellular dysfunction in the diabetic fibroblast: impairment in migration, vascular endothelial growth factor production, and response to hypoxia. The American Journal of Pathology. 2003;162(1):303-12.

71. Kisseleva T, Brenner DA. Fibrogenesis of parenchymal organs. Proceedings of the American Thoracic Society. 2008;5(3):338-42.

72. Beacham DA, Cukierman E. Stromagenesis: the changing face of fibroblastic microenvironments during tumor progression. Seminars in Cancer Biology. 2005;15(5):329-41.

73. Castello-Cros R, Cukierman E. Stromagenesis during tumorigenesis: characterization of tumor-associated fibroblasts and stroma-derived 3D matrices. Methods in Molecular Biology. 2009;522:275-305.

74. Rouillard AD, Holmes JW. Mechanical regulation of fibroblast migration and collagen remodelling in healing myocardial infarcts. The Journal of Physiology. 2012;590(18):4585-602.

75. Rhee S. Fibroblasts in three dimensional matrices: cell migration and matrix remodeling. Experimental & Molecular Medicine . 2009;41(12):858-65.

76. Scherber C, Aranyosi AJ, Kulemann B, Thayer SP, Toner M, Iliopoulos O, et al. Epithelial cell guidance by self-generated EGF gradients. Integrative Biology. 2012;4(3):259-69.

77. Albrecht-Buehler G. Daughter 3T3 cells. Are they mirror images of each other? The Journal of Cell Biology. 1977;72(3):595-603.

78. Christensen ST, Veland IR, Schwab A, Cammer M, Satir P. Analysis of primary cilia in directional cell migration in fibroblasts. Methods in Enzymology. 2013;525:45-58.

79. Serbo JV, Kuo S, Lewis S, Lehmann M, Li J, Gracias DH, et al. Patterning of fibroblast and matrix anisotropy within 3d confinement is driven by the cytoskeleton. Advanced Healthcare Materials. 2016;5(1):146-58.

80. Alexander S, Koehl GE, Hirschberg M, Geissler EK, Friedl P. Dynamic imaging of cancer growth and invasion: a modified skin-fold chamber model. Histochemistry and Cell Biology. 2008;130(6):1147-54.

81. Wu D. Signaling mechanisms for regulation of chemotaxis. Cell Research. 2005;15:52.

82. Balzer EM, Tong Z, Paul CD, Hung W-C, Stroka KM, Boggs AE, et al. Physical confinement alters tumor cell adhesion and migration phenotypes. The FASEB Journal. 2012;26(10):4045-56.

83. Pham QL, Dijamco T, Brito J, Stein E, Tong NAN, Basuray S, Voronov RS. Cell sequence and mitosis affect fibroblast directional decision-making during chemotaxis in tissue-mimicking microfluidic mazes. arXiv:170906199. 2017.

84. Ma S, Loufakis DN, Cao Z, Chang Y, Achenie LEK, Lu C. Diffusion-based microfluidic PCR for “one-pot” analysis of cells. Lab on a chip. 2014;14(16):2905-9.

85. Junkin M, Kaestli Alicia J, Cheng Z, Jordi C, Albayrak C, Hoffmann A, et al. High-content quantification of single-cell immune dynamics. Cell Report. 2016;15(2):411-22.

86. Ghorashian N, Gokce SK, Guo SX, Everett WN, Ben-Yakar A. An automated microfluidic multiplexer for fast delivery of C. elegans populations from multiwells. PLoS One. 2013;8(9):e74480.

87. Gómez-Sjöberg R, Leyrat AA, Pirone DM, Chen CS, Quake SR. Versatile, fully automated, microfluidic cell culture system. Analytical Chemistry. 2007;79(22):8557-63.

88. Gao Y, Tian J, Wu J, Cao W, Zhou B, Shen R, et al. Digital microfluidic programmable stencil (dMPS) for protein and cell patterning. RSC Advances. 2016;6(104):101760-9.

89. Berkowski KL, Plunkett KN, Yu Q, Moore JS. Introduction to photolithography: preparation of microscale polymer silhouettes. Journal of Chemical Education. 2005;82(9):1365.

90. McDonald JC, Duffy DC, Anderson JR, Chiu DT, Wu H, Schueller OJ, et al. Fabrication of microfluidic systems in poly(dimethylsiloxane). Electrophoresis. 2000;21(1):27-40.

91. Urbanski JP, Thies W, Rhodes C, Amarasinghe S, Thorsen T. Digital microfluidics using soft lithography. Lab on a chip. 2006;6(1):96-104.

92. Huntington MD, Odom TW. A portable, benchtop photolithography system based on a solid-state light source. Small. 2011;7(22):3144-7.

93. Erickstad M, Gutierrez E, Groisman A. A low-cost low-maintenance ultraviolet lithography light source based on light-emitting diodes. Lab on a chip. 2015;15(1):57-61.

94. Li X, Yu ZT, Geraldo D, Weng S, Alve N, Dun W, et al. Desktop aligner for fabrication of multilayer microfluidic devices. Review of Scientific Instruments. 2015;86(7):075008.

95. Heymann M, Fraden S, Kim D. Multi-height precision alignment with selectively developed alignment marks. Journal of Microelectromechanical Systems. 2014;23(2):424-7.

96. Jain NG, Wong EA, Aranyosi AJ, Boneschansker L, Markmann JF, Briscoe DM, et al. Microfluidic mazes to characterize T-cell exploration patterns following activation *in vitro*. Integrative Biology (Camb). 2015;7(11):1423-31.

97. Wong IY, Javaid S, Wong EA, Perk S, Haber DA, Toner M, et al. Collective and individual migration following the epithelial-mesenchymal transition. Nature Materials. 2014;13(11):1063-71.

98. Irimia D, Charras G, Agrawal N, Mitchison T, Toner M. Polar stimulation and constrained cell migration in microfluidic channels. Lab on a chip. 2007;7(12):1783-90.

99. Hayashi T, Shibata T, Kawashima T, Makino E, Mineta T, Masuzawa T. Photolithography system with liquid crystal display as active gray-tone mask for 3D structuring of photoresist. Sensors and actuators A: Physical. 2008;144(2):381-8.

100. Horiuchi T, Koyama S, Kobayashi H. Simple maskless lithography tool with a desk-top size using a liquid-crystal-display projector. Microelectronic Engineering. 2015;141:37-43.

101. Nock V, Blaikie RJ. Fabrication of optical grayscale masks for tapered microfluidic devices. Microelectronic Engineering. 2008;85(5):1077-82.

102. Mark CP, Philip H, Bloom DM, Harvey AF. Building thick photoresist structures from the bottom up. Journal of Micromechanics and Microengineering. 2003;13(3):380.

103. Mikulics M, Hardtdegen H. Nano-LED array fabrication suitable for future single photon lithography. Nanotechnology. 2015;26(18):0957-4484.

104. Lynch AE, Triajianto J, Routledge E. Low-cost motility tracking system (locomotis) for time-lapse microscopy applications and cell visualisation. PLoS One. 2014;9(8):e103547.

105. Smedler E, Malmersjo S, Uhlen P. Network analysis of time-lapse microscopy recordings. Front Neural Circuits. 2014;8:111.

106. Chen B-C, Legant WR, Wang K, Shao L, Milkie DE, Davidson MW, et al. Lattice light-sheet microscopy: Imaging molecules to embryos at high spatiotemporal resolution. Science. 2014;346(6208).

107. Software M-TOSM. Comparison With Other Microscopy Software [Available from: https://micro-manager.org/wiki/Comparison_with_other_microscopy_software.

108. Edelstein AD, Tsuchida MA, Amodaj N, Pinkard H, Vale RD, Stuurman N. Advanced methods of microscope control using μManager software. Journal of biological methods. 2014;1(2):e10.

109. Stuurman N, Edelstein AD, Amodaj N, Hoover KH, Vale RD. Computer Control of Microscopes using μManager. Current protocols in molecular biology / edited by Frederick M Ausubel [et al]. 2010;CHAPTER:Unit14.20-Unit14.20.

110. Software M-TOSM. Device Support [Available from: https://micro-manager.org/wiki/Device%20Support.

111. Software M-TOSM. Micro-Manager Programming Guide [cited 2018 June 22]. Available from: https://micro-manager.org/wiki/Micro-Manager_Programming_Guide#APIs.

112. Software M-TOSM. Micro-Manager Programming Guide 2005 [Available from: https://micro-manager.org/wiki/Micro-Manager_Programming_Guide.

113. Mathworks. Hardware Support [Available from: https://www.mathworks.com/hardware-support/home.html.

114. Software M-TOSM. Matlab and the Micro-Manager GUI [Available from: https://micro-manager.org/wiki/Matlab_and_the_Micro-Manager_GUI.

115. Software M-TOSM. Matlab Configuration [cited 2018 June 22]. Available from: https://micro-manager.org/wiki/Matlab_Configuration.

116. Blog KsM. Shading correction of fluorescence images 2014 [Available from: http://nic.ucsf.edu/blog/2014/01/shading-correction-of-fluorescence-images/.

117. Mathworks. Traveling Salesman Problem: Solver-Based [Available from: https://www.mathworks.com/help/optim/ug/travelling-salesman-problem.html.

118. Irimia D, Toner M. Spontaneous migration of cancer cells under conditions of mechanical confinement(). Integrative Biology (Camb). 2009;1(0):506-12.

119. Jain NG, Wong EA, Aranyosi AJ, Boneschansker L, Markmann JF, Briscoe DM, et al. Microfluidic mazes to characterize t-cell exploration patterns following activation *in vitro*. Integrative Biology (Camb). 2015;7(11):1423-31.

120. Saurabh S, Maji S, Bruchez MP. Evaluation of sCMOS cameras for detection and localization of single Cy5 molecules. Optics Express. 2012;20(7):7338-49.